

STRUCTURE AND HYDROGEOLOGY
OF
THE NANKAI ACCRETIONARY PRISM

南海トラフ付加体の構造と水理地質

Juichiro Ashi

芦 寿 一 郎

1991

①

STRUCTURE AND HYDROGEOLOGY OF
THE NANKAI ACCRETIONARY PRISM

A DISSERTATION SUBMITTED IN PARTIAL FULFILLMENT OF
THE REQUIREMENTS FOR THE DEGREE OF

DOCTOR OF SCIENCE

DEPARTMENT OF GEOLOGY
FACULTY OF SCIENCE
UNIVERSITY OF TOKYO

BY

Juichiro Ashi

University of Tokyo

June 1991

CONTENTS

LIST OF FIGURES

ACKNOWLEDGEMENTS

CHAPTER I. STRUCTURAL DEVELOPMENT OF THE NANKAI ACCRETIONARY PRISM REVEALED BY IZANAGI OCEAN-FLOOR IMAGING SONAR: EFFECTS OF RELIEF OF OCEANIC BASEMENT

Abstract	2
I-1. INTRODUCTION	4
I-2. DATA ACQUISITION	6
I-3. GEOLOGICAL SETTING	7
The Shikoku Basin	
Topography of the Nankai Trough	
Drilling Results	
Heat Flow	
Seismicity	
I-4. STRUCTURE OF THE ACCRETIONARY PRISM	12
Off Cape Muroto	
Off Cape Ashizuri	
Lines Parallel to the Nankai Trough	
I-5. SURFACE MORPHOLOGY	19
Nankai Trough	
Accretionary Prism: Zone I	
Accretionary Prism: Zone II	
Accretionary Prism: Zone III	

I-6. STRUCTURAL INTERPRETATIONS	25
Orientation of Thrust	
Tear Faults and Normal Faults	
Thrust Geometry	
I-7. APPLICATION OF COULOMB WEDGE MODEL	33
Theory	
Application to the Nankai Accretionary Prism	
I-8. DISCUSSION	38
I-9. SUMMARY AND CONCLUSIONS	42
REFERENCES	45
FIGURES	53

CHAPTER II. Thermal Structure and Hydrogeology
of the Nankai Accretionary Prism

Abstract	95
II-1. INTRODUCTION	97
II-2. TECTONIC SETTING AND PREVIOUS WORKS	99
II-3. HEAT FLOW ESTIMATION	101
II-4. HEAT FLOW DISTRIBUTION	104
II-5. DISTRIBUTION OF BSR	106
II-6. EFFECTS OF FLUID MIGRATION	108
II-7. HEAT FLOW VARIATIONS ALONG THE NANKAI TROUGH	110
II-8. DISCUSSION	111
II-9. SUMMARY AND CONCLUSIONS	114
REFERENCES	116
FIGURES	121
APPENDIX	135

List of Figures (Chapter I)

- Fig. I-1 Tectonic sketch map and IPOD & ODP sites (hole number) in northwestern Pacific. Boxed area is shown in Fig. I-2.
- Fig. I-2 Map showing the bathymetry (in meters) of the Nankai accretionary prism with the ship chart of IZANAGI survey.
- Fig. I-3 Outline of IZANAGI towing system and specifications of tow fish system.
- Fig. I-4 Sea Beam bathymetric map of the Nankai Trough off Shikoku.
- Fig. I-5 Migrated multichannel seismic reflection profile of line NT62-8, located on Fig. I-4.
- Fig. I-6 Migrated time sections of lines NT62-4 and NT62-5.
- Fig. I-7 Migrated time sections of lines NT62-6 and NT62-7.
- Fig. I-8 Migrated time sections of lines 55-1 and 55-2 (JAPEX unpublished data).
- Fig. I-9 Migrated time sections of lines NT62-1 and NT62-2.
- Fig. I-10 Migrated time sections of lines 55-7 and 55-8 (JAPEX unpublished data).
- Fig. I-11 Transverse migrated time sections of lines 55-A and 55-A-1 along the middle slope of the prism (JAPEX unpublished data).
- Fig. I-12 Mosaic of IZANAGI side-looking sonar images.
- Fig. I-13 Mosaic of IZANAGI images on the Nankai Trough and toe region.
- Fig. I-14 Lineament map of IZANAGI mosaic. Survey area is divided into three regions based on IZANAGI images.
- Fig. I-15 Multichannel seismic profiler record in the Nankai trough.
- Fig. I-16 Mosaic of IZANAGI images with bathymetric map at the Tosa Bae Embayment.

- Fig. I-17 IZANAGI image mosaic of eastern-most part of survey area.
- Fig. I-18 Mosaic of IZANAGI images at frontal part of the prism.
- Fig. I-19 IZANAGI image mosaic covering Zone III at the middle to the upper slope of the prism.
- Fig. I-20 Migrated time sections of lines 55-3 and 55-4 (JAPEX unpublished data).
- Fig. I-21 Mosaic of IZANAGI images showing normal faults at the western flank of the Minami Muroto Knoll.
- Fig. I-22 IZANAGI image mosaic of large landslide that occurred on the upper slope of the prism off Cape Ashizuri.
- Fig. I-23 Bathymetric map of large landslide area off Cape Ashizuri. Bathymetric contour intervals are 50 m.
- Fig. I-24 Structural interpretation map of IZANAGI images.
- Fig. I-25 Map showing acoustic basement depth in meters.
- Fig. I-26 Contour map of acoustic basement depth with IZANAGI lineaments.
- Fig. I-27 Map showing decollement depth (thick lines) versus acoustic basement depth (thin lines).
- Fig. I-28 Schematic diagram of laboratory sandbox model.
- Fig. I-29 Photographic view of initial and last stages.
- Fig. I-30 Photographic view of experimental run of second model.
- Fig. I-31 Geometry of Coulomb fracture stepping up from the decollement (after Dahlen et al., 1984).
- Fig. I-32 Multichannel seismic profiles showing basal step-up thrusts near toe region (left) and relationship between basal step-up angle and pore fluid pressure ratio.
- Fig. I-33 Porosity distribution within the Nankai accretionary prism.
- Fig. I-34 Schematic cross-section of a submarine noncohesive critical wedge with effective stress indicated by the shaded area on the right (after Dahlen, 1984).

Fig. I-35 Multichannel seismic profiles and cross-sectional shapes of the Nankai accretionary prism.

Fig. I-36 Relationship between fluid pressure ratio and coefficient of internal friction.

Fig. I-37 Relationships between fluid pressure ratio and efficient of internal friction for various ratios between internal and basal fluid pressure.

Fig. I-38 Schematic cross-section parallel to the axis of the Nankai Trough showing migration of pore fluid.

Fig. I-39 Plot of fluid pressure vs. depth vs. distance in the frontal part of the prism.

Fig. I-40 Model of fluid migration toward oceanic basement high.

List of Figures (Chapter II)

- Fig. II-1 Tectonic sketch map and IPOD & ODP sites (hole number) in northwestern Pacific.
- Fig. II-2 Multichannel seismic profile showing Bottom Simulating Reflector (BSR) in the Nankai accretionary prism.
- Fig. II-3 Flow chart of heat flow estimation from seismic reflection profile.
- Fig. II-4 Map showing the bathymetry (in meters) of the Nankai accretionary prism with the data points of heat flow estimated by BSR.
- Fig. II-5 Contour map of heat flow estimated by depth of BSR with previous heat probe data (closed circle).
- Fig. II-6 Migrated multichannel seismic reflection profile of line NT62-8, located on Fig. A-3.
- Fig. II-7 Map showing sediment thickness above acoustic basement in meters.
- Fig. II-8 Contour map of sediment thickness with heat flow distribution.
- Fig. II-9 Sediment thickness versus heat flow estimated from BSR.
- Fig. II-10 Calculated surface heat flow according to the steady state model along the Line KH86-5-6-1 (Kinoshita and Kasumi, 1986) with observed heat flow values around the line.
- Fig. II-11 Cross-section showing thermal structure in the lines off Cape Muroto and Cape Ashizuri.
- Fig. II-12 Heat flow values versus distance from the NW-SE trending line of the Kinan Seamount chain.
- Fig. II-13 Mosaic of IZANAGI side-looking sonar images.
- Fig. II-14 Schematic cross-section showing fluid expulsion and advective heat flow near the deformation front.

ACKNOWLEDGEMENTS

I am much indebted to Professor Asahiko Taira of the Ocean Research Institute, University of Tokyo for continual support and critical reading of this manuscript. Thanks are due to Drs. Hidekazu Tokuyama and Tim Byrne who provided many encouraging discussions throughout this study. I would like to thank Drs. Kiyoshi Suehiro, Kantaro Fujioka and Jean Crespi for helpful advice. For the seismic reflection profiles, I am grateful to Mrs. Ei-ichiro Nishiyama and Shinichi Kuramoto for providing unpublished data and their helpful suggestions. Valuable discussions from Drs. Wonn Soh of Shizuoka University and Masataka Kinoshita of Tokai University greatly improved this paper. I wish to thank Professors Yujiro Ogawa of Kyushu University and Kazuo Kobayashi of the Ocean Research Institute, who support me for participating in the international meetings about the role of fluids in subduction zones in 1988 and 1990. I am also grateful to Mrs. Fujio Yamamoto, Toshiaki Ueki, Shoichi Kiyokawa and colleagues of Submarine Sedimentation Division of the Ocean Research Institute, University of Tokyo for their support of IZANAGI data acquisition and encouragement throughout this study.

CHAPTER I

STRUCTURAL DEVELOPMENT OF THE NANKAI ACCRETIONARY PRISM REVEALED BY IZANAGI OCEAN-FLOOR IMAGING SONAR: EFFECTS OF RELIEF OF OCEANIC BASEMENT

ABSTRACT

The Nankai accretionary prism, off southwest Japan represents one of the best developed clastic prisms in the world. A combination of swath mapping systems including Sea Beam and "IZANAGI" side-looking sonar image and closely spaced seismic reflection profiles revealed that the evolution of the prism is essentially controlled by the incoming oceanic basement relief.

The backscattering sonar image obtained by IZANAGI shows that the frontal part of the prism is characterized by continuous lineaments which correspond to the anticlinal ridges caused by imbricate thrusts occurring in a regular spacing. The incipient deformation of the trench fan suggests that the most active frontal accretion occur approximately within 10 km landward of the deformation front, because the slope sediments, which is assumed to be derived from the same source as the trench fan, mask the anticlinal ridges except for the frontal part of the prism. In the middle to the upper slope of the prism, the IZANAGI image shows features of numerous landslides as well as brittle failure such as prominent lineaments indicative of large fault scarps.

The evolution of the prism has been strongly affected by the decollement depth which is indirectly destined by the oceanic basement relief. The oceanic basement dipping oblique to the convergence direction forms en échelon folds at the frontal part of the prism, similar to the effect of oblique subduction. The low topographic profile of the frontal areas where the oceanic basement high is subducted demonstrates that the growth of the prism is closely related to the amount of the offscraped sediments. The widespread strike-slip faults across the prism are interpreted to reduce the strain caused by the difference between the various growth patterns of the prism. Moreover, the mud volcanoes observed on the trough floor are developed along these faults under the high pore pressure generated at the toe of the prism.

The frontal low topographic areas are dominated by the small tapered accretionary prism without the retrogression of the base of the landward slope. Based on the step-up angle of frontal thrusts, the overpressured decollement is estimated in the small tapered prism. This is also supported by the remarkable reversed polarity along the decollement plane in the seismic reflection profiles. In addition, the noncohesive critical tapered model suggests the occurrence of high pore pressure in the small tapered prism. Such high pore pressure may be caused by the lateral migration of pore fluids from the surrounding area where the larger tectonic overburden arises the elevation of pore pressure. It is likely that the pore fluid migrates more easily along the decollement than within the prism because of the continuity of the conduits.

I-1. INTRODUCTION

Deformation, offscraping and underplating of sediments at a plate convergent boundary are initial processes of continental crustal evolution and mountain building. Studies of accretionary prisms thus bear a fundamental importance in understanding the history of the earth. Recently, much emphasis has been placed on understanding the complex interactions between structural fabrics, physical properties, plate kinematics and especially pore fluids.

Accretionary prisms are mechanically similar to subaerial fold-and-thrust belts although they are more strongly affected by hydrogeologic frameworks (Langseth and Moore, 1990). Pore fluids within a prism or along a basal detachment zone play an important role in mechanics of faulting because fluid pressure greatly reduces the effective stress (Hubbert and Rubey, 1959). Physical properties in a prism show large lateral as well as vertical changes that are closely associated with modes of fluid expulsion and styles of geologic structures (Bray and Karig, 1985; Moore, 1989). Mechanical behavior of a prism has been estimated by critical tapered model (e.g. Davis et al., 1983) and thrust geometry (Platt, 1990).

The effect of incoming oceanic basement has also been emphasised as an important aspect of deformation in accretionary prisms. Although growth of a prism is basically controlled by the amount of offscraped sediment, bending-induced grabens on the subducting plate are also important for sediment subduction and tectonic erosion (Karig, 1974; Hilde, 1983) and seamounts may cause indentation and severe deformation at the base of inner slope (Lallemand and Le Pichon, 1987; Yamazaki and Okamura, 1989). Mauffret et al. (1984) ascribed a forward growth of a prism in response to oceanic basement relief which controls the sediment supply. Orientations of thrusts and folds observed in a prism are influenced by convergence direction as well as slope orientation (Silver, 1971; Huchon et al., 1982) and Seely (1977)

proposed that oblique subduction may form *en echelon* overlapping folds and thrusts. These processes, however, have been studied individually, so they have not been integrated into a larger, coherent picture of an accretionary prism. One of the best areas to complete an integrated study of the variables that control the growth of accretionary prisms is located in the Nankai Trough, southwest Japan.

The Nankai accretionary prism marks a zone of sediment deformation at the convergent boundary between the Philippine Sea and Eurasian plates (Fig. I-1). Seismic reflection profiles indicate that the sediments, which are mainly composed of trench-fill turbidite and underlying hemipelagite, have been offscraped at the foot of the inner slope, forming closely spaced, anticlinal ridges (Aoki et al., 1983; Moore et al., 1990). These data also show that the underlying Shikoku basin sediments are undeformed and are being thrust beneath the accretionary prism.

This paper describes both the surface features and the internal structures of the Nankai accretionary prism off Shikoku on the basis of IZANAGI side-looking sonar image and seismic reflection profiles, and discusses the effects of the oceanic basement relief on accretion. This area is favorable for revealing the evolution of the prism for two reasons. One is the presence of various prism shapes though the accreting sediments have a uniform composition. The other is the availability of abundant data from DSDP Legs 31, 58, 87 and ODP Leg 131, and a variety of data collected during the French-Japanese Kaiko project surveys.

I-2. DATA ACQUISITION

The IZANAGI survey was carried out using the R/V Shinsan Maru, operated by the Ocean Research Institute, University of Tokyo, in conjunction with the Seafloor Survey International (SSI) and the Sanyo Suiri Sokuryo (SSS), between June 8 and 23, 1989. The 3.5-kHz sub-bottom profilers were obtained simultaneously. The survey area covered both the Nankai Trough and the Nankai accretionary prism off Shikoku (Fig. I-2). In this paper, the eastern and western parts of the surveyed area are informally named the area off Cape Muroto and off Cape Ashizuri, respectively.

The IZANAGI side-looking sonar is a sea-floor imaging system and a bathymetric mapping system in a single body that is towed at depths of 120 m or less at speeds up to 10 knots (Fig. I-3). The IZANAGI is capable of producing a continuous side-looking swath image of seafloor for a width of 1 km - 40 km. Most side-looking images were processed for noise reduction and intensity correction by SSI, and then formed into a mosaic with overlapping swaths on the basis of navigation data by SSS. The image at the eastern-most area was not processed but mosaiced by hand.

Closely spaced seismic reflection profiles were used for mapping of various features such as geometry of the thrusts and depth of the oceanic basement. All seismic reflection lines including unpublished data have been obtained during the past 10 years. These profiles are roughly divided into five data sets of the specific survey programs as shown in appendix (Figs. A1-A4). The bathymetry off Shikoku was provided by the Sea Beam map constructed during the Kaiko project in 1984 (see Le Pichon et al., 1987a) and the IZANAGI data based on a phase difference technique.

I-3. GEOLOGIC SETTING

The Nankai Trough extends 700 km from the Suruga Trough, which marks a collision zone between the Izu-Bonin island arc and Honshu arc, to the northern tip of the Kyushu-Palau Ridge (Fig. I-1). The Nankai accretionary prism defines the landward slope of the trough and consists of sediments derived from the trough and the Shikoku Basin. The Shikoku Basin is situated in the northeastern corner of the Philippine Sea plate, which is converging to northwest or west-northwest, based on fault plane mechanisms (Kanamori, 1971) and plate kinematics (Seno, 1977; Minster and Jordan, 1979). Estimated values of the convergent rate vary from 1 - 2 cm/yr (Ranken et al., 1984) to 3 - 4 cm/yr (Seno, 1977).

The Shikoku Basin

Analysis of magnetic anomalies constrains the kinematic evolution of the Shikoku Basin and suggests an irregular opening with multiple episodes of spreading during the late Oligocene to middle Miocene (Kobayashi and Nakada, 1978; Shih, 1980). The basement relief of the subducting Shikoku Basin, which was mapped by the "Jean Charcot" single-channel seismic reflection system, also shows a complex ridge and trough basement topography. Le Pichon et al. (1987b) identified two conspicuous structural trends; one oriented 310°, is fossil spreading center that trends parallel to the magnetic anomalies in this area and the other, oriented 350°, is interpreted as transform faults related to the last phase of spreading. Chamot-Rooke et al. (1987) proposed that the opening of the Shikoku Basin proceeded from early east-west rifting to late north-south spreading on the basis of the magnetic lineations and the N-S trending transform faults. The Kinan Seamount Chain, which is being subducted at the central part of the Nankai Trough (Fig. I-1), is interpreted to be the expression of an aborted stage of seafloor

spreading in the Shikoku Basin (Chamot-Rooke et al., 1987), although it has been modified by off-ridge volcanisms (Klein and Kobayashi, 1980).

Topography of the Nankai Trough

In view of submarine topography, the Nankai Trough is roughly divided into two domains. One is the area off the Tokai District at the water depth about 4000 m, where the trough floor is narrow due to the existence of the Zenisu Ridge running roughly NE-SW. In this area, the French-Japanese Kaiko and Kaiko-Nankai projects were conducted (Le Pichon et al., 1987a; Kobayashi, Le Pichon, et al., 1989). During these projects the submersible "Nautile" and a deep-towed camera (JAMSTEC) equiped on the R/V "Hakuho", revealed the development of benthic communities associated with fluid venting (Ohta and Laubier, 1987; Fujimoto, Kobayashi et al., 1989). The second area is the area off Kii peninsula and Shikoku Island in water depth between 4500 and 4900 m. The trough in this area is characterized by a broad and flat sea-floor. The cross-section along the trough axis shows variations of sediment thicknesses and oceanic basement relief and indicates that the trench-filling process is closely controlled by the structure of the oceanic basement (Le Pichon et al., 1987b). The maximum sediment thickness beneath the trough exceeds 2000 m at a depression in the basement. Therefore, the shallowness of the trough is due partly to the thickness of the sediment, and partly to the shallow dipping lithosphere of the subducting young Shikoku Basin.

Drilling Results

Deep-sea Drilling programs such as DSDP Legs 31, 58 and 87 and ODP Leg131 provided a variety of data related to the development of the accretionary prism in three regions: the Shikoku Basin, the Nankai Trough and the Nankai accretionary prism.

DSDP Sites 297, 442, 443 and 444 drilled in the Shikoku Basin (Fig. I-1). The hemipelagic sequence drilled at Site 297 is characterized by a clayey

siltstone followed by a silty claystone with interbedded graded silt and sand, which is estimated to be early Pliocene to middle Miocene age (Ingle, Karig, et al., 1975a). In the southwestern part of the Shikoku Basin, Site 443 penetrated mostly hemipelagic layers and bottomed in the Miocene basaltic sills (Curtis, 1980).

The Nankai Trough off Shikoku was visited two times during DSDP operations. The cores retrieved from Site 582 show two lithologic units: an upper turbidite unit (566 m) and a lower hemipelagic unit (183 m). The turbidite sequence is composed of interbedded sandstone and shale (Kagami, Karig, et al., 1986), that were probably deposited by a distal channel and levee type turbidity currents. These sediments were transported laterally along the trough axis from the Fuji River drainage and are interpreted to be the direct consequence of the Izu collision in Pliocene-Pleistocene times (Taira and Niitsuma, 1986). Based on the geometry of the uppermost trench-fill strata, the subduction rate in the Nankai Trough was estimated to be between 1.4 and 2.0 cm/yr for the past 10^4 to 10^5 yr (Karig and Angevine, 1986). This value is somewhat lower than seismologically determined rates of 3 - 4 cm (Seno, 1977; Minster and Jordan, 1979). The lower hemipelagic unit consists of dark gray mudstone and volcanic ash and is lower Pleistocene to Pliocene age.

The third region, the Nankai accretionary prism, is located just landward of the Nankai Trough. Site 298 penetrated at the toe of the prism off Cape Ashizuri (Fig. I-1). This hole encountered a stratigraphic section consisting of 183 meters of late Pleistocene turbidite deposits underlain by 427 meters of late to early Pleistocene clay, silt and clayey-silty sand (Karig, Ingle, et al., 1975b). Site 583 was drilled on the same terrace as Site 298, approximately 15 km westward. A total of eight holes in this site penetrated the frontal thrust at about 170 m sub-bottom. The sediments throughout all of the holes are described as Quaternary hemipelagic muds with interlayered units of sand and silt. Results of Sites 582 and 583 show that the 450 m section of Site 583 is lithologically similar to Unit 1 of Site 582 despite the differences in structural features. Bray and Karig (1986) have proposed that these

differences reflect the processes of dewatering related tectonically deformed sediments on the basis of comparisons in physical properties between Site 582 and Site 583.

During ODP Leg 131, Site 808 was drilled in the toe of the prism off Cape Muroto, where the fossil spreading center in the Shikoku Basin is currently being subducted. This drilling site is located in the studied area of this paper, therefore, a more detailed review is given. At this hole, six lithologic units were identified (Taira, Hill, Firth et al., in press). Unit I is composed muddy slope apron deposits at 0-20 m sub-bottom. Unit II (20-556.8 m sub-bottom) consists of Pleistocene turbidites; the upper part of this unit is almost the same lithology as the turbidite sequence at Site 582. Unit III is lithological transition zone between Unit II and Unit IV. Unit IV (618.5-1243 m sub-bottom) is composed of lower Pleistocene to middle Miocene hemipelagic mudstone. Unit V (1243-1289.9 m sub-bottom) is composed of several thick, white acidic tuffs (maximum thickness 4.5 m) interbedded with vari-colored hemipelagic mudstone. These volcanoclastic deposits are interpreted to be due to the magmatism near trough in the middle Miocene time (Tatsumi, 1982). Unit VI (1289.9-1327 m sub-bottom) is subdivided into two basaltic units: an upper sill bearing unit and a lower pillow lava unit intercalated with red tuffaceous mudstones. The age of these mudstones is 15 Ma B.P. Hole 808 penetrated two structural discontinuities. One is a thrust fault with a separation estimated to be 309 m along fault plane and the other is the decollement situated at 945-965 m sub-bottom.

Heat Flow

Heat flow distribution around the Nankai Trough is revealed by relatively abundant thermal probe data (Uyeda, 1972; Watanabe et al., 1977; Yoshii, 1979). In addition, Yamano et al. (1982) have estimated heat flow values using the phase relation of the gas hydrate system. Bottom-hole temperatures at Site 583 are also consistent with the values (Kinoshita and Yamano, 1986). The heat flow distribution map off Shikoku compiled by

Yamano et al. (1984) shows that heat flow is unexpectedly high in the trough and decreases landward and seaward. Four explanations for the high heat flow in the trough have been proposed. First, subduction of a young hot plate (Yamano et al., 1984). Second, heat flow disturbance caused by migration of pore fluid (Yamano et al., 1984). Third, chemical reactions in the sediments (Kinoshita and Yamano, 1986). Fourth, the recovery of conductive heat flow in the trough owing to sedimentation (Nagihara et al., 1989).

Seismicity

The Wadati-Benioff zone is relatively shallow (10°) and short in length in southwest Japan. Although the seismic activity of the Nankai Trough is relatively low in comparison with neighboring subduction zones, great earthquakes have repeatedly occurred and caused large tsunamis. Such large tsunamis have been generated off Shikoku at average intervals of 120 yr (Hatori, 1974). Based on arrival times of tsunami waves along the coast of SW Japan, the source areas of tsunamis have been estimated. The three latest tsunamis, which were caused by the Hoei earthquake (1707), the Ansei earthquake (1854) and the Nankaido earthquake (1946), occurred at almost same source area (Ando, 1975; Aida, 1981). The area regarded as the tsunami source extends from the continental shelf to the upper slope of the Nankai accretionary prism around 1500 m in water depth. On the other hand, there is no seismicity around the toe of the prism except for intra-crustal earthquakes, although active deformation within the prism and along the decollement is well documented.

I-4. STRUCTURE OF THE ACCRETIONARY PRISM

An accretionary prism is well developed in the landward slope of the Nankai Trough off Shikoku. The landward slope extends from the toe of the prism at a depth about 4800 m to the outer-ridge seaward of several forearc basins at a depth about 1500 m. Multi- and single-channel seismic lines (Figs. A1-A4) reveal that the sedimentary section which is well-defined in the trough has been subducted and deformed during accretion. Topography of the studied area is characterized by a large embayment off Cape Muroto, named the "Tosa Bae Embayment" by Leggett et al. (1985), as well as several other smaller embayments on depressions (Fig. I-4). Therefore, one important problem is to confirm whether the internal structure of the embayment is different from that in the surrounding area or not. The area off Cape Muroto, where the ODP leg 131 was conducted, is representative of the embayment region. On the other hand, the area off Cape Ashizuri, which was drilled on DSDP legs 31 and 87, is appropriate as a reference region for the area off Cape Muroto. These two wedges are discussed below.

Off Cape Muroto

There are a number of multichannel seismic lines around the Tosa Bae Embayment, for example, JAPEx lines (N55-1, N55-A, 55-1, 55-2, 55-A), ORI lines (KH83-2-2-2, KH86-5-6-1, KH86-5-7), Fred Moore lines (NT62-4, 5, 6, 7 and 8) as well as Kaiko single-channel lines. In the following paragraphs I describe the internal structure of the prism from the toe to the outer-ridge.

NT62-8. Starting with line NT62-8 because it provides the most detailed structural features in the lower slope of the prism (Fig. I-5). The lowest reflector of line NT62-8 shows laterally continuous, low frequency acoustic basement. This reflector is well-defined for a few tens kilometers under the prism. Based on the drilling result of ODP leg 131 which is located on this line

(Taira, Hill, Firth et al., in press), the acoustic basement is composed of acidic volcanoclastic deposits (Unit V) and basaltic rocks (Unit VI). The incoming sediments beneath the trough floor can be roughly divided into two stratigraphic units (Fig. I-5, shot#1400-1600). The lower unit above the oceanic basement is acoustically transparent with a few moderate amplitude reflectors. This unit is correlated with Unit IV of the Shikoku Basin hemipelagic layer. The upper layered unit, which consists mainly of terrigenous turbidite sequence (Units II and III), lies on the hemipelagic unit and fills the trough.

The most conspicuous reflector in the lower part of the section is situated within the hemipelagic unit and is considered to be a decollement. The reflector is characterized in a reversal polarity indicating a decrease of acoustic impedance caused by a decreasing seismic velocity and/or density across the interface. Moore et al. (1990) have suggested that the reversed polarity along the decollement is due to abnormally high pore fluid pressures. The decollement reflector is subparallel to the oceanic basement and extends from the landward limit of line NT62-8 (Fig. I-5) to the trough near shot# 1450, although it is impossible to determine the seaward limit of the reflector.

Subduction-related deformation begins at the base of the seaward dipping slope. The incipient uplift of the trough floor is seen at shot# 1615-1690 (Fig. I-5). This elevation is assumed to be less than 30 m and caused by a frontal thrust that reaches the seafloor at shot #1615. The frontal thrust cuts up both the hemipelagic and turbidite sequences, and soles into the decollement. Seaward of the frontal thrust, there are small structural disruptions in the sedimentary sequence that are not expressed in the surface morphology. The seaward limit of this deformation, the deformation front, is located at shot#1600. Second thrust, named the "first thrust" by Moore et al. (1990), occurs at 2 km landward of the frontal thrust. This thrust clearly cuts up from the decollement and forms a ramp structure within the hemipelagic sequence. The overthrusting sediments have formed a fault-bend fold over the ramp. The region between these "first-" thrusts on the deformation front

is designated the "prot thrust zone" by Ingle, Karig, et al. (1975b). Landward of this zone, several thrusts are developed at intervals of about 1.5 km, although individual fault planes are barely visible on the seismic reflection line. Most thrust faults in the imbricate thrust zone dip about 30° landward except for several backthrusts, that have been inferred from fault-bend folds.

Slope basins are usually distributed in depressions situated between anticlinal ridges. One of the largest basins has developed landward of the ridge formed by a major landward dipping thrust fault (Fig. I-5, shot#2800-). A backthrust is also present on the landward flank of this ridge. The strata within the basin, increase in dip with increasing depth, suggesting progressive uplift of the ridge.

NT62-4,5 & 6. Lines NT62-4, 5 and 6 show the internal structure near the deformation front in sections parallel to the trough axis (Figs. I-6 & I-7a). The decollement reflector is distinguishable from reflections of sedimentary layers on the basis of its reversed polarity. Lines NT62-5 and 6 indicate that the decollement plane is subparallel to the top of the oceanic basement rather than the sea-floor. The sedimentary sequences, which have been deformed by gently landward dipping thrusts, are also cut by upward divergent faults named the "flower" or "palm tree" structure (Fig. I-6b, e.g. shot#1300, and Fig. I-7a). The flower structure is regarded as that caused by transpression displacement along high angle to moderately dipping faults. The distribution of flower structures in three seismic lines suggest that directions of these faults are almost parallel each other and roughly NW-SE.

JAPEX 55-1 & 2. Line 55-2 is extremely close to Line NT62-8 and furthermore provides better resolution of the internal structure of the prism landward of Line NT62-8. The surface slope of the prism suddenly steepens landward of the large slope basin (Fig. I-8b, shot#780-). The slope increases from 1°-2° to 6°-7° there. Moreover, depth sections of line N55-1 (Nasu et al., 1982) and NT62-8 (Moore et al., 1990) indicates that the decollement increases

in dip from 3° to 4° under the imbricate thrust zone to 6°-7° beneath the region of steep slope. The morphology of the accretionary prism, therefore, suggests two wedges: a seaward wedge with an angle of 4°-6° and a landward wedge with a wedge angle of 12°-14° (e.g. Fig. I-8a, shot#1100-1700 and shot#500-1100).

Fig. I-8b shows several landward dipping thrusts in the steep slope region (shot#800-1200). Dips of these thrusts are shallow in comparison with the frontal imbricate thrusts and thus they are interpreted as out-of-sequence thrusts. Line 55-1 is subparallel to Line 55-2 and located at 20 km eastward of it (Fig. I-8a). This profile also exhibits several well-developed out-of-sequence thrusts. The area of crustal movement estimated by arrival time of tsunamis extends to this region, suggesting that some of these faults are seismically active (Kagami, 1986). In fact, undulations on the steep slope (Fig. I-8a, shot#900-1000; Fig 8b, shot 800-900) appear to be composed of slide deposits caused by displacements of nearby thrust faults.

Off Cape Ashizuri

Cross sections perpendicular to the trough axis in the area off southeast of Cape Ashizuri indicate no remarkable change in dip of the surface slope. Bathymetric maps also show that contour intervals off Cape Ashizuri are relatively constant in comparison with the increase on slope associated with the embayed area off Cape Muroto (Fig. I-4). Line NT62-2 is a typical example of a wedge-shaped accretionary prism; multichannel seismic lines NT62-1, NT62-3, N55-3-1, 55-7, 55-8 and Kaiko single-channel lines also show similar profiles (Figs. A1-A4).

NT62-2. The seismic stratigraphy in NT62-2 is almost the same as NT62-8. However, the hemipelagic sequence in the former region is intercalated with highly reflective stratified unit, which consists of a Pliocene terrigenous turbidite sequence based on the drilling at DSDP sites 297 and 582, as pointed out by Moore et al. (1990).

Structural style in the protothrust zone is characterized by the presence of several 45° dipping "seismic discontinuities" (Fig. I-9b, shot#520-600) and thickening of the sedimentary sequence. These structures are apparently formed by kink folds spaced several hundred meters apart, that are similar to the style of deformation in cores from DSDP hole 583 (Kagami, Karig, et al. 1986). Karig and Lundberg (1990) argued that the thickening process is due to the result of ductile pre-failure flow in the protothrust zone.

An incipient landward dipping thrust forms a fault-bend fold at the arcward termination of the protothrust zone (Fig. I-9b, shot#620). Landward of this fold, a frontal thrust cuts up from the decollement and emerges at shot#645. The terrace caused by thrusting of the first thrust is uplifted about 170 m above the trough floor. The second thrust occurs approximately 2.3 km landward of the first thrust. The fault planes of both thrusts are straight and dip about 25°.

The surface of the prism shows relatively constant slope as mentioned above. In detail, however, there are two inflection points in the bathymetry. One is the steep slope region situated landward of the third thrust (Moore et al., 1990). This steepness is interpreted to be caused by a fault-bend fold because the steep slope region is restricted to the hanging wall of the third thrust (Fig. I-9b, shot#730-750). The other is the conspicuous inflection point at shot#980 where the slope increases from 4° to 8° landward. The change of the dip may be resulted in out-of-sequence thrusts emerged at shot#980-1100. The base of this steep slope is characterized by a deformed layered sequence, which seems to be a slope basin overlain by overthrusting sediments (Fig. I-9b, shot#980). This structural feature is more striking in NT62-1 (Fig. I-9a, shot#160-190).

JAPEX 55-7 & 8. Lines 55-7 and 8 are located 15 and 40 km westward of NT62-2. These profiles show the whole internal structure of the prism off Cape Muroto. The imbricate thrust zone, which shows the same structural style as NT62-2, is seen in lines 55-7 (shot#1550-1800) and 55-8 (shot#1600-

1850). Out-of-sequence thrusts also occur in the upper slope, and tsunami source studies (Hatori, 1974) suggested that some of these thrusts appear to be seismically active. Landslide structures and topographic features are well-developed on the upper slope (Fig. I-10a, shot#700-1000, Fig. I-10b, shot#900-1250). The surface slope of the prism is roughly constant from the toe region to the depth of 1500 m where the slope decrease toward the outer ridge.

Lines Parallel to the Trough Axis

Lines 55-A and 55-A-1 are located at the middle of the seaward dipping slope, 40 km landward of the trough axis (Fig. I-11). Line 55-A mainly reveals the internal structure of the prism at the embayment area off Cape Muroto. Line NT62-8 intersects this line at shot#750 (Fig. I-11a). On the other hand, Line 55-A-1 shows the internal structure off Cape Ashizuri and Line NT62-2 crosses this line at shot#3100 (Fig. I-11b). Reflectors subparallel to the sea-floor, named bottom Simulating Reflector (BSR), are widely distributed at a depth about 0.5 seconds in two-way travel time. This reflector can be seen in most profiles of the prism off Shikoku and corresponds to the bottom of the gas hydrate layer.

For descriptive purpose, Line 55-A has been subdivided into two sections. The eastern profile is situated in the embayment area off Cape Muroto (Fig. I-11a, shot#250-1200) and shows a graben like structure at shot#380-540. A eastward dipping normal fault can be clearly seen at shot#500-530, whereas a thrust fault is present just west of the normal fault and forms a ramp anticline at shot#700. A backthrust is also present on the western flank of this anticlinal ridge. A channel-and-levee like structure is developed at the base of the steep slope (shot#920). This structure seems to be a kind of drainage connected to a gully landward.

The western section of the profile is dominated by the two peaks of the Minami Muroto Knoll. The profile in the eastern flank of this knoll shows eastward steeply dipping sedimentary sequences (Fig. I-11a, shot#1200-1350). On the contrary, the westward dipping sequences extends from shot#1350 to

shot#2000. The western flank of the knoll is characterized by westward dipping normal faults emerged at shot#1750, 1870 and 2010.

I-5. SURFACE MORPHOLOGY

The surface morphology of the accretionary prism is produced by a combination of faulting, folding and gravitational sliding. A seismic reflection profile provides such structural features in a cross section of the prism. The topographic map has been used to assume the lateral distribution of each structure between seismic profiles. In fact, a Sea Beam map is very useful for mapping of thrust faults, fold axis, and landslides. Structural maps of the Nankai accretionary prism show the general distribution of thrusts, anticlines and synclines (Kagami, 1986; Le Pichon et al., 1987b). However, it is difficult to know the lateral extend and configuration of these thrusts which have relatively small value of total accumulated displacement, even by means of the Sea Beam survey. In this study, the side-looking sonar IZANAGI revealed the distribution and trend of more detail structures in the prism and the trough.

The mosaic of IZANAGI side-looking image observed around the Nankai Trough is shown in Fig. I-12. The image of the Nankai trough is relatively flat and low reflectivity. On the other hand, the image of the accretionary prism is characterized by numerous lineaments and undulations. The mosaic image of the prism is roughly subdivided into three regions, here designated as Zone I, Zone II and Zone III. Zone I is the seaward-most region of the prism. The image exhibits a rugged configuration in a direction parallel to the trough axis. Zone II is distributed in the lower to the middle slope of the prism. The image is similar to the first one except for some discontinuous lineaments. Zone III is situated in the middle to the upper slope of the prism. The image indicates striking contrast lineaments and irregularly bounded configurations.

Nankai Trough

The Sea Beam bathymetric map shows that the trough floor dips less than 0.05° and ranges from 10 to 30 km wide off Shikoku Island. The IZANAGI image also shows that the flat trough floor is characterized by low reflectivity

suggesting fine grained sediment cover. Moreover, there is no evidence for a well developed axial channel in the trough floor. The development of the channel seems to depend on the dip of the trough floor as pointed out by Taira and Niitsuma (1986). In the seaward of the trough floor, the gently landward dipping slope is overlain by finer grained materials than that in the trough floor on the basis of reflectivity.

Most conspicuous feature observed by IZANAGI is a cone situated landward-most of the trough floor (Fig. I-13). This cone is 2 km in diameter, less than 50 m in height, and characterized by the depression at the top. The reflectivity of the cone is very high even if its morphological effect is considered. The IZANAGI image suggests that this cone is a mud volcano, which is well-known in active margins (e.g. Westbrook and Smith, 1982; Barber et al., 1986). Furthermore, two similar cones are detected in the middle of the trough floor (Fig. I-13).

There are a lot of lineaments perpendicular or oblique to the trough axis as shown in Figs. I-13 & I-14. Especially, several lineaments are well-developed around the mud volcanoes. The trend of these lineaments are approximately NW-SE. Some of them seems to extend into the prism. Toward the western part of the IZANAGI mosaic, the trend of the lineament swings from northwest to west-southwest (Fig. I-14). Seismic profiles indicate that these lineaments are due to lateral displacement along high angle faults without deformations of the oceanic basement (Fig. I-6). In other words, these lineaments are considered to be tear faults or lateral faults. In the eastern-most of the study area, however, the oceanic basement appears to have been deformed, forming the NW-SE trending ridge and depression, based on seismic profiles in the trough (Fig. I-15). The IZANAGI mosaic shows the NW-SE lineament where the trough fill is affected by the movement of the oceanic basement (Fig. I-12).

Accretionary Prism: Zone I

The Zone I is situated along the toe of the prism. Based on the seismic reflection survey, this zone includes the protothrust zone and the seaward part of the imbricate thrust zone. The IZANAGI mosaic shows relatively continuous lineaments that are nearly parallel to the trough axis in this zone (Fig. I-12). The reflectivity of the lineaments immediately changes across the track line of the IZANAGI fish, suggesting that each lineament is due to a change in slope and not to unique properties of the sediments along the lineament. Seismic profiles also reveal that these lineaments correspond to anticlinal ridges caused by thrust faults (e.g. Fig. I-5). Therefore, it is easy to document the lateral extent and configuration of the thrusts with the aid of the IZANAGI images. The interval between lineaments is remarkably constant in the middle to the eastern part of the IZANAGI mosaic (Fig. I-16). For instance in the middle area, the lineaments at intervals of 1.5 km are in good agreement with the fault-bend faults observed in the seismic profile NT62-8 (Fig. I-5). On the whole the intervals decrease westward with narrowing of the zone width (Fig. I-12).

The general trend of the lineaments is NE-SW in the eastern area and is N60E in the western area (Fig. I-12). At the boundary area between these areas, the seaward-most lineaments have almost the same trend (N50E) as those in the eastern area. However, most lineaments landward of the protothrust zone are oriented about N70E. Moreover, the boundary region is also characterized by dextral en échelon folds, which suggest a component of right-lateral displacement. Axis of these folds trend approximately NE-SW. At the eastern-most region where a NW-SE trending basement high and depression have been subducted, there are a few lineaments which trend about N70E (Fig. I-17).

The IZANAGI image also shows that the trench fan is developed across the deformation front (Fig. I-16). The presence of a distinct lineament on the fan reveals that the fan has been affected by frontal thrusting. The height of this fan above the trough floor is assumed to be less than 20 m because it is

impossible to observe it even with the IZANAGI bathymetric map. The probable source of this fan deposits, which is distributed in the Zone II, appears to be undeformed.

Accretionary Prism: Zone II

The boundary between the Zone I and the Zone II is gradational because the Zone II is regarded as the region where slope sediments have covered and modified the configuration of the fault-bend folds. The slope sediment is assumed to consist mainly of very fine grained material based on the low reflectivity of the image. Observations with a deep-sea camera, carried out during Hakuho Maru cruise KH86-5, also suggest that the surface in the Zone II is overlain by muddy sediments (Watanabe, 1988). Moreover, surface samples obtained by piston core from the slope basin in the Zone II are composed of clay or silty clay (e.g. Soh, 1988). Slope basins are well-developed between the anticlinal ridges and the IZANAGI images show that the slope basin in the middle area is sharply bounded by the thrust fault on its landward side and by a fault-bend fold on its seaward side (Fig. I-18). The width of the Zone II is broad in the eastern area and narrow in the western area due to the difference of deformation style, as discussed in a later section (Fig. I-14).

Lineaments oblique or perpendicular to the trough axis, considered to be tear faults, are observed landward of the trough floor where tear faults are also abundant (Fig. I-18). Some of these structures extend to the trough floor, although they are difficult to identify in the Zone I. Another kind of lineament cuts the anticlinal ridges in the middle area (Fig. I-18). These structures are characterized by closely aggregated lineaments which show low reflectivity, indicating that they are composed of fine sediments. The structures are interpreted to be a huge clastic dikes, due to injection of clastic materials. These structures are also similar to features reported as "mud ridges" in the Barbados Ridge accretionary complex (Brown and Westbrook, 1988), which were interpreted as clastic intrusions.

Accretionary Prism: Zone III

Zone III is characterized by two features on the IZANAGI data. The first is a lineament that is marked by a high degree of contrast in reflectivity and sharp, well defined boundaries (Fig. I-19). The contrast is due to a narrow and steeply slanting slope, such as a fault scarp, whereas the sharpness in contrast is associated with whether the surface sediment is hard or not. In contrast, most lineaments in the Zone I correspond to fault-bend folds, because the sediment is not sufficiently lithified to form well deformed faults. The absence of gullies around the toe of the prism supports the idea that the surface sediment is not lithified. Zone III however is characterized by a large number of cliffs and numerous well-defined gullies.

The second feature that characterizes Zone III are irregularly bounded configurations (Fig. I-19). Seismic reflection profiles reveal that these configurations are due to surface undulations caused by landslides. A large number of landslides occur on the steep slopes of Zone III and partly masks the fault scarps. The seismic line 55-3 shows well-developed sliding planes and thrusts within the slope basin as well as undulations composed of sliding materials (Fig. I-20a). The distal part of this landslide is detectable in the IZANAGI image (Fig. I-19). The seismic profile also shows that the thickness of the basin changes across the thrust fault, suggesting that landslides have been repeatedly caused by the tilting of the slope due to thrusting.

Based on the IZANAGI image and the Sea Beam map, the most striking lineaments correspond to thrust faults that are distributed in the steep slope region (Figs. I-4 & I-12). In other words, the slope of the prism is associated with the development of these thrusts, which are interpreted to be out-of-sequence thrusts based on the seismic profiles. On the other hand, normal faults also show lineaments with striking contrast and two regions of well-developed normal faults have been recognized. One region is situated on the western flank of the Minami Muroto Knoll (Fig. I-21) and the other is just seaward of this knoll (Fig. I-21). The first region is detected by the seismic line

55-A (Fig. I-11a) . The lineaments of normal faults have a more striking contrast than that of thrust faults. This may be due to the difference in scarp morphology between the two structures.

The side-looking image in the upper slope of the prism is provided by another IZANAGI mosaic (Fig. I-22). The survey area of this mosaic is situated just west of the former area. The IZANAGI image reveals that a large submarine landslide occurred at a depth between 1000 and 2000 m off Cape Ashizuri (Fig. I-23). The landslide is distributed in a 20 by 30 km area and the upper-most part of the landslide is characterized by slide scars characterized by high reflectivity. The dip direction of the slope is southwest to south and most of the collapsed material has moved down slope to form a large number of depositional lobes. Part of the sliding material also appears to extend to the Ashizuri Canyon. In the middle of the landslide area, a NE-SW trending lineament is detected with a mud volcano-like cone. This lineament is a surface expression of the thrust exhibited by the seismic line 55-7 (Fig. I-10a). The large landslide may have been caused or triggered by the movement along this thrust.

I-6. STRUCTURAL INTERPRETATIONS

The structural interpretations of the Nankai Trough and the accretionary prism off Shikoku are presented here on the basis of the IZANAGI mosaic, seismic reflection profiles and a Sea Beam bathymetric map. In total, these data suggest that lineaments revealed by the IZANAGI mosaic correspond to thrust faults, tear faults or normal faults that exhibit a variety of directions or intervals (Fig. I-24). This chapter focused on three structural features; orientations of thrusts, origins of tear faults and normal faults, and relationship between thrust geometry and growth of the prism.

Orientation of Thrusts

The effect of oblique convergence on the geometry of fold-and-thrust belts have been argued by several authors (e.g. Silver, 1971; Seely, 1977; Huchon et al, 1982; Breen and Silver, 1989). The orientations of folds and thrusts have been explained to be due to the interaction between convergent direction and slope orientation. In other words, the development of folds and thrusts is greatly affected by the gravity component of the stress as well as the regional or plate tectonic stress. Huchon et al. (1982) proposed that the trend of folds and thrusts is intermediate between the slope dip and the normal to the convergence.

The IZANAGI interpretation map shows well-developed NE-SW trending frontal thrusts at the eastern area (Fig. I-24). This area is marked by the very small tapered wedge which has a gentle slope (1° - 2°) and a shallow dipping decollement (3° - 4°). Such gentle slope is considered to have a negligible gravity component of the stress. Consequently, the convergence direction in this area is assumed to be about northwest on the basis of the trend of thrust faults revealed by IZANAGI data and the topography. This direction is roughly consistent with the previous estimated values based on fault plane mechanisms and the plate kinematics (e.g. Seno, 1977). The NE-

SW trending thrusts extend more than 10 km from the deformation front to the imbricate thrust zone.

In the western area, the orientation of thrusts is approximately N60E (Fig. I-24). Seismic reflection profiles (e.g. NT62-2, 55-6) show that the slope of the prism in this area is steeper than that in the eastern area. The strike and dip of the landward slope in this area is about N65E and 4°, respectively, thus with the assumed convergent direction in the eastern area predicts the oblique subduction in this area. However, the orientation of the thrust faults are not intermediate in trend as proposed by Huchon et al. (1982). According to Silver (1971), fold axes and thrust fault are essentially parallel to the direction of the slope of the prism and are only mildly sensitive to the convergent direction.

There are two regions where the orientation of thrusts is much different than the normal NE-SW trend. One is the eastern-most region where the NW-SE trending oceanic basement high is subducted (Fig. I-24). The IZANAGI image shows landward bending lineaments, which correspond to frontal anticlinal ridges, owing to the subduction of the basement high. The Sea Beam map (Fig. I-4) and the IZANAGI mosaic (Fig. I-12) suggest right lateral displacements along the steep slanting slope.

The second area is the boundary between the western and the eastern areas (Fig. I-24). This area is characterized by the N50E and the N70E trending imbricate thrust faults and en échelon folds as described in the previous section. The orientation of fold axis is approximately normal to the assumed NW convergent direction. Seely (1977) suggested the development of en échelon structures owing to oblique convergence. The structural features in the boundary area appear to be associated with the relief of the subducting oceanic basement based on seismic reflection data. Fig. I-25 provides the depth of the acoustic basement mapped by using of 67 multichannel seismic reflection profiles. Conversion of travel time into the depth in meters is based on average velocity law (Fig. A5) constructed by previous interval velocity data and drilling results. The depth to basement shows that northward dipping oceanic basement has been subducted beneath the boundary area. The

N70E trending thrust fault and en échelon folds are probably formed by this process. Dextral en échelon folds suggest a right-lateral displacement owing to the subduction of obliquely dipping basement. On the other hand, Fig. I-26 shows the northwestward dipping oceanic basement beneath the frontal part of the boundary area as well as in the other frontal areas. The N50E trending frontal thrust seems to be independent of the subduction of obliquely dipping basement and the gravity force effect.

Strictly speaking, the orientation of thrusts should be associated with the decollement configuration rather than the oceanic basement relief, because the accretionary prism rides on the detachment surface (decollement) and not always on oceanic crust. However, it is difficult to know the depth of the decollement in the study area because there are few seismic profiles available for the mapping. Fig. I-27 provides the depth to decollement only in the small area near the deformation front, and reveals that the contour of the decollement is almost parallel to that of the acoustic basement. It is probable that the basement relief is regarded as the decollement configuration. Consequently, the configuration of the incoming oceanic basement appears to produce the same effect as oblique subduction on the morphology of the prism. This deformational processes can be reproduced experimentally as described below.

An experimental study of obliquely inclined oceanic crust was made by means of a simple sandbox. The sandbox model is similar to the model used in previous studies (e.g. Davis et al., 1983; Byrne et al., 1988), and is composed of a transparent box, a sheet of Mylar and sand (Fig. I-28). The Mylar sheet lies on a flat rigid base and in turn underlies the sand. Horizontal compression is achieved by pulling the Mylar sheet. The sand wedge is created in the sand as the Mylar sheet is moved toward the back wall. The first model conducted so that the dip of the rigid base was in the same orientation as the pulling direction. Fig. I-29 illustrates, in top view, that the orientation of the thrust faults are almost normal to the convergence direction, although lineaments near the wall are bent due to the effect of friction along the side walls.

The second model where the dip of the rigid base was oblique to the pulling direction was also completed. Orientations of thrusts in the sandbox are oblique to the convergence direction. In other words, the wedge was wider where the Mylar sheet (decollement) was deepest. In addition, en échelon folds have developed between the oblique thrusts. Each of these fold axes are normal to the convergence direction. The results of this experimental study are in good agreement with the observation around the Nankai Trough as revealed by the IZANAGI side-looking sonar data.

Tear Faults and Normal Faults

As mentioned above, the surface morphology is associated with the decollement configuration, which appears to be controlled by the oceanic basement relief. The acoustic basement map indicates that NW-SE and WNW-ESE trending ridge-and-trough structures dominate the eastern and western areas respectively (Fig. I-25). The directions of these ridge-and-trough structures are consistent with the orientations of magnetic anomalies reported by Chamot-Rooke et al. (1987), although possible fossil transform faults may have modified the original relief. Le Pichon et al. (1987b) proposed that three N10W trending fossil transform faults exist in this area. Overall, the general trend of the oceanic basement relief is nearly parallel to the assumed plate convergence direction. Therefore, the evolution of the prism should be different between blocks divided by the sections roughly parallel to the convergence direction. In other words, the prism should be well-developed in the area where the decollement is deep and a large amount of sediments have been accreted. It is also likely that tear faults may occur at the boundary area between the different types of wedges, because the tear fault may have accommodated the two types of deformation.

The IZANAGI interpretation map (Fig. I-24) and the acoustic basement depth map (Fig. I-26) show that the tear faults have the same trend as the ridge-and-trough structures in the oceanic crust. For instance, the NW-SE trending tear faults are developed in the eastern area, and the WNW-ESE

trending tear faults are distributed in the western area (Fig. I-26). The most conspicuous tear faults, which strike NW-SE, form a boundary zone between the eastern and the western areas. The cross sectional shape of the accretionary prism changes across this boundary zone: the wedge in the eastern area has a much smaller tapered than the wedge in the western area (Figs. I-5 & I-9). The tear fault zone appears to accommodate the strain between the different types of wedges.

Mud volcanoes on the trough floor are distributed within 7 km of the deformation front. In the Barbados Ridge accretionary prism, a large number of mud diapirs occur on the trough floor as well as on the slope of the prism. Westbrook and Smith (1982) have suggested that abnormally high pore pressures are generated within the prism extend toward the trough, and resulted in the formation of mud volcanoes. The mechanisms of diapir has been regarded as buoyancy caused by reversal of density around the diapir body. Moreover, high pore pressure in the source of mud diapir plays an important role in the development of mud injection (e.g. Barber et al., 1986). The mud volcanoes revealed by the IZANAGI survey are probably caused by the same mechanism as those in the Barbados Ridge. Fig. I-16 also shows that two mud volcanoes are situated along tear faults in the boundary zone. The formation of mud volcanoes therefore seems to be due to the injection of muddy materials along tear faults. Brown and Westbrook (1988) also attributed the distribution of the mud volcano in the trough to the oceanic basement relief. In this case, mud volcanoes are interpreted to be initiated along the faults which caused by the differential compaction across the large steps in the oceanic basement.

Normal faults occur in the steep slope of the prism, and show a striking contrast in reflectivity (Fig. I-19). Seismic reflection line 55-A also demonstrates that the normal faults are particularly well-developed between the different shapes of accretionary wedges in the western flank of the Minami Muroto Knoll (Fig. I-11a).

Thrust Geometry

Several kinds of differences between the western and the eastern areas were revealed by the IZANAGI and seismic reflection data, as described above. However the most remarkable differences in this part of the prism are the prism's shapes, and the geometry of the thrust faults. In the eastern area where the small tapered wedge is formed, thrusts with dips about 30° occur at intervals of 1.5 km and maintain this spacing for more than 15 km (Fig. I-5). On the other hand, the western area has a large tapered wedge and the spacing of imbricated thrust sheets gradually decreases landward. The frontal thrust also dips only about 25° landward (Fig. I-9).

Based on the Coulomb failure criterion, the dip of a thrust fault is found by the factors of friction, fluid pressure and cohesion of a prism (Dahlen et al., 1984; Davis and von Huene, 1987). This relation is briefly explained below. The axis of the maximum compressional stress should dip seaward when the prism grows with a resisting shear traction along the basal decollement as shown in Fig. I-31. In this state, a shallowly dipping forward thrust and/or steeply dipping backthrust occur at angles of $45^\circ - \varphi/2$ to the σ_1 , where coefficient of internal friction $\mu = \tan \varphi$. Therefore, the dip data of thrusts provides the internal friction (μ) and the angle of σ_1 to the decollement (ψ_b). In the case of a submarine accretionary prism, the pore fluid pressure must also be considered. λ and λ_b are the fluid pressure ratios to lithostatic pressure (Hubbert and Rubey, 1959) in the wedge and on the base, defined by

$$\lambda = (P_f - \rho_w g D) / (\sigma_d - \rho_w g D)$$

where ρ_w , g , P_f are the constant density of the overlying water, the constant acceleration of gravity and the pore fluid pressure.

By using of Mohr circle construction, the ψ_b is related to the cohesive S_0 , internal and basal friction coefficients μ , μ_b and internal and basal fluid pressure ratios λ , λ_b by

$$[\mu(1-\lambda) + S_0/\rho g H] \sin 2\psi_b = \mu_b(1-\lambda_b) [(1+\mu^2)^{1/2} - \mu \cos 2\psi_b]$$

where H is the local wedge thickness, ρ is the mean sediment density (Dahlen, 1984). This equation can be rewritten in terms of basal stepup angle of forward thrust to the decollement, δ_b as

$$K\mu\mu_b\cos\theta+(\mu+S_0/\rho gH)\sin\theta = K\mu_b(1+\mu^2)^{1/2}$$

where

$$\theta = \pi/2 - \arctan \mu - 2\delta_b$$

$$K = (1 - \lambda_b)/(1 - \lambda)$$

This equation suggests that the basal stepup angle of the thrusts, δ_b , is only related to the factor K , when internal and basal frictions and cohesion are constant. In the toe of the Nankai accretionary prism, there is no significant difference of composition between the western and the eastern areas based on drilling results (Bray and Karig, 1982; Taira, Hill, Firth, et al., in press). Hoshino et al. (1972) has also reported that the coefficient of friction μ is not dependent on the porosity but the kind of materials. Therefore, the internal and basal friction coefficients and the cohesion is assumed to be almost the same in both areas.

The seismic reflection profiles indicate that the thrusts clearly cut up from the basal decollement in both the western and the eastern areas (Fig. 1-5). Data for determining the stepup angles are restricted only the two thrusts near the toe, because the more landward faults are probably modified by the later deformations and incipient faults do not appear to step up from the decollement. The measured stepup angles are 30° in the eastern area and 25° in the western area. Fig. 1-32 shows the relationship between δ_b and μ for various values of K , assuming $\mu_b = 0.4$, $S_0/\rho gH = 0.4$. The coefficient of internal friction μ was estimated to be 0.4-0.5 based on the angle between two conjugate faults at the toe of the eastern prism. The cohesion and coefficients of friction μ , μ_b are not precise and unique but consistent with the estimated values in other accretionary prisms (e.g. Davis and von Huene, 1987; Zhao et al., 1986). In any case, there is the tendency that the larger value of K

corresponds to the smaller stepup angles without regard to cohesion or friction coefficient. Fig. I-32 also shows that the value of K in the eastern area is smaller than that in the western area. The small K value indicates the large difference between the basal and the internal fluid pressure ratios. Higher basal fluid pressure ratios are also suggested by the well-developed reversed polarity along the decollement for the eastern area (e.g. compare seismic lines NT62-8 and NT62-2, Figs. I-5, I-9 & I-32).

The IZANAGI data show a nearly constant imbricate spacing of thrust in the eastern area (Fig. I-16). Mulugeta and Koyi (1987) reported that the constant imbricate spacing is accompanied by the small tapered wedge on the basis of the experimental study using a sandbox. On the other hand, the seismic reflection profile in the western area indicates that the imbricate spacing decreases toward the rear of the prism although the quality of the reflections also gradually diminishes landward (Fig. I-9). Such differences in growth of the prism seems to reflect the physical properties of internal materials. Fig. I-33 provides the sections showing the porosity distribution assumed by the interval velocity data (Nasu et al., 1982) in the western and eastern areas. Conversion of interval velocity into porosity is based on the laboratory measurements (Hamilton and Bachman, 1982) and the drilling results (Bray and Karig, 1986). It is clear that the porosity gradually decreases landward in the western area. In the eastern area, however, the porosity varies and shows no systematic change. These results suggest that the dewatering of sediments in the large tapered wedge effectively occurs by overthrusting.

I-7. APPLICATION OF COULOMB WEDGE MODEL

Theory

Accretionary prisms generally display a wedge-like cross-section that has been compared to the wedge of soil or snow that forms in front of a moving bulldozer. In case of no additional material, the wedge attains a steady state shape and slides stably on the basal detachment surface. As new sediment is accreted at the toe, the material within the wedge deforms to maintain its critical taper. The wedge thus continues to grow self-similarly during sliding. Such critically tapered wedges are assumed to be on the verge of Coulomb failure everywhere (Davis et al., 1983). Coulomb wedge theory therefore appears to provide a working model of accretionary wedge mechanics (Zhao et al., 1986). Laboratory measurements of rock strength also suggest that friction and brittle failure mechanisms control the deformation and state of stress in the upper crust (Brace and Kohlstedt, 1980), supporting the assumption that brittle, or Coulomb, failure is the dominant deformation mechanism in accretionary wedges.

The theoretical analysis of a Coulomb wedge can be divided roughly into two models, depending on whether or not cohesion is considered. A uniformly cohesive wedge displays a slightly concave surface slope (Dahlen et al., 1984). Typical shapes of submarine wedges, however shows convex upper surface slope and Zhao et al. (1986) have considered the increase in cohesion toward the inner part of the wedge to explain the convex shape of the Barbados accretionary prism. Their porosity profile was obtained from an empirical porosity-cohesion relation which is consistent with porosity reduction during the accretion. The model for a noncohesive wedge, which exhibits a perfectly triangular geometry, produces the simple and exact solution (Dahlen, 1984). In this paper, the theoretical treatment of the Coulomb wedge is based upon a noncohesive wedge model because the influence of cohesion on a wedge shape is mostly restricted to the toe of an accretionary prism (Dahlen, 1984).

The model relating the wedge shape, which has constant surface slope α and constant basal dip β , to the internal and basal strength parameters μ , μ_b , λ , λ_b is illustrated in Fig. I-34. The static equilibrium of stresses in a wedge lacking cohesion and frictional sliding on a basal decollement provides the equation between the cross-sectional shape and strength parameters as follows.

$$\alpha + \beta = \psi_0 - \psi_b \quad (1)$$

$$\frac{\tan 2\psi_0}{(1 + 1/\mu^2)^{1/2} \sec 2\psi_0 - 1} = \left(\frac{1 - \rho_w/\rho}{1 - \lambda} \right) \tan \alpha \quad (2)$$

$$\frac{\tan 2\psi_b}{(1 + 1/\mu^2)^{1/2} \sec 2\psi_b - 1} = \left(\frac{1 - \lambda_b}{1 - \lambda} \right) \tan \mu_b \quad (3)$$

where the angle ψ_0 and ψ_b are the constant acute angle between the axis of principal compressive stress and the surface and base of the wedge as shown in Fig. I-34.

Critical taper equation (1), (2) and (3) implies that increasing the basal traction or decreasing the wedge strength increases the taper. Davis et al. (1983) estimated the coefficient of internal friction from the observed fluid pressure ratio in the Taiwan fold-and-thrust belt by assuming $\mu_b = 0.85$ (Byerlee, 1978) on the base. Moreover, they applied the Coulomb wedge model to other accretionary prisms by using of the estimated coefficient of internal friction $\mu = 1.03$ and predicted the fluid pressure ratio by assuming $\lambda = \lambda_b$. Obtained pore fluid pressures in several accretionary prisms are consistent with calculated values of λ in spite of imprecise measurements during drilling operations.

Application to the Nankai Accretionary Prism

Various shapes of accretionary prisms occur in the Nankai Trough but they are roughly divided into two cross-sectional shapes. One is nearly triangular with the wedge having a constant surface slope. The other appears to be composed of two wedges; a frontal wedge that has a small taper angle and a more landward wedge with a large taper angle. In general, most wedges belong to the former type and the wedge near the drilling site of DSDP Leg 87 off Cape Ashizuri (Fig. I-9b) is of this type. The latter type of wedges display a peculiar embayment topography (Fig. I-5a). The drilling site of ODP Leg 131 is located in the second type of prism (i.e., Tosa Bae Embayment off Cape Muroto). These two types of wedges are thus alternately developed along the structural trends of the Nankai Trough (Fig. I-35).

Using a Coulomb wedge model, the differences in shapes between the prisms off Cape Muroto and Cape Ashizuri is thought to be due to the value of fluid pressure ratio within the prism and/or on the basal decollement. The surface slope angle α of both wedges are easily determined from the depth sections of multichannel seismic profiles (Nasu et al., 1982). The high resolution seismic profiles, moreover, provide the decollement dip β , although the decollement was usually assumed to be parallel to the top of the oceanic crust. The relation between the fluid pressure ratio λ and the coefficient of internal friction μ was computed on the basis of noncohesive Coulomb wedge model by assuming $\lambda = \lambda_b$ (Fig. I-36).

If a reasonable coefficient of internal friction μ is used, it is possible to determine the fluid pressure ratio. The coefficient μ is not dependent on the porosity but the kind of materials (Hoshino et al., 1972). The results of DSDP Leg 87 and ODP Leg 131 show no significant differences of composition and grain size between the two drilling sites (Bray and Karig, 1982; Taira, Hill, Firth, et al., in press). Thus, the coefficient of internal friction μ is presumed to be constant in the wedges off Shikoku. By adopting the coefficient μ between 1.03 (Davis et al., 1983) and 1.1 (Dahlen, 1984), the relative differences of fluid

pressure ratio in each wedges make clear the effect of fluid pressure on the wedge shape (Fig. I-36).

In the seaward wedge off Cape Muroto (hereafter referred to as Wedge A1), the fluid pressure ratio is very high λ (λ_b) = 0.97 (Fig. I-36) and equivalent to the ratio near the toe of the Barbados estimated by Davis et al.(1983) and measured by Moore et al.(1982). Such high λ means that the pore fluid pressure is nearly lithostatic. On the other hand, the landward wedge off Cape Muroto (referred to as Wedge A2) predicts λ (λ_b) < 0.5, which is low even when compared the fluid pressure ratio ($\lambda = 0.6-0.9$) found in most accretionary prisms. This very low λ is smaller than the ratio $\lambda = 0.5$ in the Japan Trench (Davis et al., 1983) where the tectonic erosion occurs (Karig, 1975). The wedge off Cape Ashizuri (referred to as Wedge B) has a typical taper in the Nankai Trough corresponding to a predicted fluid pressure ratio λ (λ_b) = 0.8-0.9 (Fig. I-36). This value is almost the same as that in the Aleutian Trench or the Oregon margin (Davis et al., 1983; Hottman et al., 1979; Moore and von Huene, 1980). Strictly speaking, the assumption that $\lambda = \lambda_b$ is probably incorrect because pore fluid pressure on the basal decollement is generally considered to be larger than that within the prism (Moore, 1989). The effect of a variation in λ_b versus λ have to be examined below.

Fig. I-37 illustrates plots of λ_b versus μ for various values of $(1 - \lambda_b)/(1 - \lambda)$ expressed by coefficient K. The function $K=1$, <1 and >1 means $\lambda_b = \lambda$, $\lambda_b > \lambda$ and $\lambda_b < \lambda$ respectively. In addition, increasing the deviation of K from 1, is equivalent to increasing the discrepancy between λ_b and λ . Fig. I-37 shows that the basal fluid pressure of Wedge A1 is nearly lithostatic in the range $K > 0.75$. The anomalous low value $K = 0.55$ only permits the lower basal fluid pressure ratio $\lambda_b = 0.75$. Therefore, it may well be that λ_b in Wedge A1 is very high ($= 0.95$) and significantly larger than λ . In Wedge A2, which is situated landward of Wedge A1, the Coulomb wedge theory is satisfied only in the range $1 < K < 1.25$. This situation indicates that the basal friction approaches to the internal friction (Dahlen, 1984). It also suggests that the basal decollement is relatively strong and that a new decollement may form within

the wedge. The possibility of the formation of a new decollement is also consistent to the existence of out-of-sequence thrust faults within Wedge A2. In Wedge B, there is no difference between λ_b and λ owing to the ratio $K = 1$. The presumption that the ratio K in Wedge A1 is smaller than that in Wedge B is in good agreement with the result predicted from the step-up angle of thrust faults.

I-8. DISCUSSION

Some embayment topographies in the landward slope of the Nankai Trough are situated where the oceanic basement high is subducted as shown in the seismic reflection profiles and the Sea Beam bathymetric maps (Fig. I-4). In the oceanic basement high, the amount of sediments to be accreted is small due to the shallow decollement. In fact, seismic reflection profiles indicate that the quantity of material which constitutes the Wedge A at the embayment is much smaller than that of the surrounding Wedge B (Fig. I-35). Therefore the landward configuration is ascribed to the relief of the oceanic basement in view of the amount of sediment accreted. The tendency that the decollement depth mainly depends on the oceanic basement relief may be due to that the decollement is developed in a hemipelagic layer selectively. The decollement should be almost parallel to the oceanic basement, because the hemipelagic sediment layer on the oceanic basement is roughly constant in thickness, whereas the turbidite sediment tends to fill the depression.

The embayments along the trough or trench off Shikoku, Hyuga and Erimo (Fig. I-1) has been regarded as the traces where the seamount subducted under the prism (Yamazaki and Okamura, 1989). Lallemand and Le Pichon (1987) proposed the evolutionary model of seamount subduction on the basis of the criteria that undercritical or overcritical slope causes thickening or erosion in the prism, respectively. They predicted the retrogression of the wedge from its initial location during the seamount subduction because frontal accretion is absent or very limited. Following their model, the deformation front should retreat after the subduction of the seamount. On the contrary, the embayment off Shikoku, which is called the Tosa Bae Embayment, is characterized by that the deformation front advances seaward rather than moves back. Seismic reflection profiles show that such low topographic portion is composed of not slumping or falling materials but newly accreting materials (Fig. I-5). The reason why the very small tapered

accretionary prism is well developed in front of the embayment off Shikoku should be discussed below.

According to a Coulomb wedge theory, the small tapered wedge means high fluid pressure ratio which reduces the internal and basal friction. Such high ratio of fluid pressure nearly equal to lithostatic was actually observed in a few small tapered wedges of active accretionary prisms (Moore et al., 1982; Moore and von Huene, 1980). High pore fluid pressure estimated around the embayment where the oceanic basement rise has subducted can be explained by the model as illustrated in Fig. I-38. Interstitial waters are generally expelled through the permeable layer when the tilted sedimentary unit comprises permeable layers such as in the Nankai Trough. At the toe of the prism, pore fluids migrate up not only seaward but toward the oceanic basement rise. Such migration of fluids may raise the pore pressure above the basement rise. A small tapered wedge such as Wedge A1 grows under the high pore pressure ratio during subduction of the basement rise. At the landward slope of the prism, the comparison of fluid pressure ratio in the same level below the sea surface indicates that the ratios of Wedge A1 should be smaller than those of Wedge B everywhere as shown in Fig. I-38. As a result, pore fluids migrate from Wedge B to Wedge A1 due to the difference of pressures. Moreover, the decollement is regarded as one of significant conduits for pore fluids because its plane has good continuity rather than high permeable sediment layer (Moore, 1989). For this reason, the pore fluid pressure in the decollement of Wedge A2 appears to be more elevated than that within the wedge (Fig. I-39). Angles of thrusts stepped up from the decollement, which suggest that the difference between λ and λ_b is larger in Wedge A1 than Wedge B, support the model inferred above. Therefore, the existence of tilted layers and decollement along the Nankai Trough axis, which is ascribed to the oceanic basement relief, cause the active fluid flow within the prism and through the decollement (Fig. I-40). It can be said that a subducting basement relief is most significant factor for the development of the prism.

Another topographic feature of the embayment off Cape Muroto is steep slope landward of the small tapered wedge discussed above (Fig. I-8). Such steep slope corresponds to the surface slope of Wedge A2 (Fig. I-36). In the Barbados Ridge complex, the Barracuda Ridge and the Tiburon Rise, which have a role of a dam for the sediment supply from the Orinoko fan delta, provide local control of sediment thickness (Westbrook and Smith, 1982). Mauffret et al. (1984) reported the detail relationship between the basement relief and the structure of the prism and concluded that the growth of the front is controlled by the thickness of the sediment layer accreted. However, shapes across the prism are almost constant everywhere without the dependence on the amount of the accreting sediment.

For the formation of Wedge A2, three major factors have been proposed. The first is the effect of the subducting seamount, which forces the inner trench slope material forward and upward (Yamazaki and Okamura, 1989). Indeed, the basement rise inferred above can be regarded as a kind of the seamount. The second is associated with the existence of multiple decollement which shift their position to the higher level because of the increase of the basal friction (Kagami, 1986). Such multiple decollement, which is described as out-of-sequence thrusts, probably accelerates to make the prism thicken. The high angle taper as shown in Wedge A2 also suggests the high friction on the decollement and the development of out-of-sequence thrusts. The process that accounts for the high friction on the decollement must be discussed below. The third is underplating which provides new materials from the bottom of the prism (Leggett et al., 1985), although there is no observation of steep slope above where underplating occurs, as well as in the Barbados Ride accretionary complex. However, underplating is a good explanation for the increase of the basal friction beneath the region of steep slope, when the decollement cuts or comes in contact with the oceanic basement. It is probably that the friction between the oceanic basement and the overlying accreted sediments may be larger than that within the sediment (Kagami, 1985). Moreover, seismic reflection profiles indicate that steep slope region is

situated just above where the decollement steps down and appears to contacts the oceanic basement (Fig. I-8, shot#1000).

SUMMARY AND CONCLUSIONS

Various cross sectional shapes of the accretionary prism are distributed along the Nankai Trough. They are roughly divided into two shapes. One is simple triangular shape composed of the surface slope slanting by 3° - 5° and the decollement plane dipping by 4° - 5° . This type of the prism is commonly seen along the Nankai Trough and regarded as the standard wedge. The other consists of the seaward gentle and the landward steep surface slopes slanting by 1° - 2° and 6° - 7° , respectively. The decollement dip is slightly smaller than that of the standard wedge, therefore this type is the complex of the seaward and the landward wedges. The seaward wedge corresponds to the low topographic region such as "Tosa Bae embayment" and has been discussed about the evolution (Leggett et al., 1985; Kagami, 1986; Yamazaki and Okamura, 1989). However, the formations of the two type's prisms have been argued individually. The IZANAGI side-looking sonar images revealed the structural variations of the prism laterally.

Based on the IZANAGI images, the Nankai accretionary prism is subdivided into three structural domains superficially. The frontal accretional zone named "Zone I" is defined as the laterally continuous rugged topographic features caused by active fault-bend folding. Toward the Zone II landward of the Zone I, such undulations are gradually masked by slope sediments. The trench fan which consists of the fine grained materials derived from the slope basin in the Zone II is developed across the deformation front, undergoing incipient deformation due to frontal accretion. This observation suggests that the Zone I is more active than the Zone II tectonically.

The convergence direction can be estimated by the orientation of the imbricate thrusts dominating Zone I in the eastern area where the effects of both the gravity force in the prism and the subducting oceanic basement relief are negligible. This direction is roughly consistent with the values estimating from the fault plane mechanisms or the plate kinematics (e.g. Seno, 1977). In

the area where the dip of the oceanic basement is oblique to the convergence direction, however, the thrust zone is characterized by en échelon folds due to the same effect as oblique subduction. With the good correlation between the decollement configuration and the oceanic basement relief, the development of the thrust faults should be considered to result from the former rather than the latter.

The imbricate thrust sheets observed in the Zone I are assumed to accelerate dewatering owing to the rapid tectonic overburden. The accreted sediments which initially have porosities of at least 50% are gradually lithified toward the rear of the prism. The IZANAGI image provides the striking lineaments indicating steep cliffs such as fault scarps in the middle to the upper slope of the prism (Zone III). As comparison with the image of the Zone I showing gradual reflectivity change, the surface sediments seem to be enough lithified to failure brittly in the Zone III. This assumption is in good agreement with the occurrence of probable seismic thrusts in this region, because the Zone III is located in the main crustal movement areas estimated by tsunami arrival times at large earthquakes. The numerous landslides observed in the Zone III might be caused by such thrusting.

The growth pattern of the prism is basically associated with the amount of the offscraped sediment. In other words, the oceanic basement relief indirectly controlling the decollement depth appears to play the most important role in the growth of the prism, because the deeply seated decollement must provide a large quantity of the sediments into the prism. Around the Nankai Trough off Shikoku, the NW-SE trending ridge-and-trough structure has subducted toward approximately NW. Therefore, it is likely that the shapes of the prism vary in the NW-SE cross sections. The widespread tear faults in both the trough and the prism are interpreted to be the structures which release the strains between the such different types of the prism. The mud volcanoes observed on the trough floor may be related to the tear faults under the high pore pressure, which is caused by the lateral migration of pore fluids from the prism.

The retrogression of the base of the landward slope has been reported in the area where the seamounts (Lallemant and Le Pichon, 1987; Yamazaki and Okamura, 1989) or the basement highs (Mauffret et al., 1984) are subducted beneath the prism. In the Tosa Bae Embayment, however, the deformation front advances seaward rather than retreats landward, even if the basement high has subducted there. Based on the Coulomb Wedge theory (Davis et al., 1983), the forward growth of the prism with smaller tapered wedge suggests weaker friction in decollement and/or stronger prism. The results of the drillings indicate no significant differences between the accreted materials. Moreover, the localized high pore pressure in the decollement plane revealed by the seismic reflection profiles is consistent with the weak decollement. Such high pore pressure in the embayment area may be caused by the lateral migration of pore fluids from the surrounding area where the larger tectonic overburden arises pore pressure. The pore fluid is assumed to migrate easily along the decollement rather than within the prism because of the continuity of the conduits. The step-up angle of thrusts at the toe of the prism also supports the localized high pore pressure in the decollement.

The steep slanting slopes are widely distributed at the 30 - 40 km landward of the deformation front. Seismic reflection profiles suggest that the steep slope regions are situated just above where the decollement steps down and cuts or contacts with the oceanic basement. Such underplating may be a good explanation for the increase of the basal friction which makes the prism more large-tapered. Consequently, it is likely that the evolution of the accretionary prism off Shikoku is basically controlled by the incoming oceanic basement relief.

References

- Aida, I. 1981. Numerical Experiments for the Tsunamis generated off the coast of the Nankaido district. *Bull. Earthq. Res.* 56, 713-730.
- Ando, M. 1975. Source mechanisms and tectonic significance of historical earthquakes along the Nankai Trough, Japan. *Tectonophysics*, 27, 119-140.
- Aoki, Y., Tamano, T., and Kato, S. 1983. Detailed structure of the Nankai Trough from migrated seismic sections. *Mem. Am. Asso. Pet. Geol.* 34, 309-322.
- Barber, A.J., Tjokrosapoetro, S., and Charlton, T.R. 1986. Mud volcanoes, shale diapirs, wrench faults, and Melanges in accretionary complexes, eastern Indonesia. *Am. Asso. Pet. Geol. Bull.* 70, 1729-1741.
- Brace, W.F., and Kohlstedt, D.L. 1980. Limits on lithospheric stress imposed by laboratory experiments. *J. Geophys. Res.* 85, 6248-6252.
- Bray, C.J., and Karig, D.E. 1985. Porosity of sediments in accretionary prisms and some implications for dewatering processes. *J. Geophys. Res.* 90, 768-778.
- Bray, C.J., and Karig, D.E. 1986. Physical properties of sediments from the Nankai Trough, Deep Sea Drilling Project Leg 87A sites 582 and 583. In Kagami, H., Karig, D.E. et al., *Init. Repts. DSDP*, Washington (U.S. Govt. Printing Office), 87, 827-842.
- Breen, N. A., and Silver, E. 1989. The water back arc thrust belt, eastern Indonesia: The effect of accretion against an irregularly shaped arc. *Tectonics*, 8, 85-98.
- Brown, K., and Westbrook, G.K. 1988. Mud diapir and subduction in the Barbados Ridge accretionary prism complex: The role of fluids in accretionary processes. *Tectonics*, 7, 613-640.

- Byerlee, J. 1978. Friction of rocks. *Pure Appl. Geophys.* 116, 615-626.
- Byrne, D.E., Davis, M.D., and Sykes, R. 1988. Loci and maximum size of thrust earthquakes and the mechanics of the shallow region of subduction zones. *Tectonics*, 7, 833-857.
- Chamot-Rooke, N., Renard, V., and Le Pichon, X. 1987. Magnetic anomalies in the Shikoku Basin: a new interpretation. *Earth Planet Sci. Lett.*, 83, 214-228.
- Curtis, D.M., and Echols, J. 1980. Lithofacies at the Shikoku and Parece Vele Basins. In Klein, G. deV., and Kobayashi, K., et al., *Init. Repts. DSDP*, Washington (U.S. Govt. Printing Office), 58, 701-710.
- Dahlen, F.A. 1984. Noncohesive critical coulomb wedges: An exact solution. *J. Geophys. Res.* 89, 10125-10133.
- Dahlen, F.A., Suppe, J., and Davis, D. 1984. Mechanics of fold-and-thrust belts and accretionary wedges: cohesive coulomb theory. *J. Geophys. Res.* 89, 10087-10101.
- Davis, D.M., Suppe, J., and Dahlen, F.A. 1983. Mechanics of fold-and-thrust belts and accretionary wedges. *J. Geophys. Res.* 88, 1153-1172.
- Davis, D.M., and von Huene, R. 1987. Aleutian subduction zone seismicity, volcano-trench separation, and their relation to great thrust-type earthquakes. *Geology*, 15, 517-522.
- Fujimoto, H., Kobayashi, K., et al. 1989. Deep-Tow observation of seafloor ventings in the eastern Nankai accretionary prism. *EOS*, 70, 1381.
- Hamilton, E.L., and Bachman, R.T. 1982. Sound velocity and related properties of marine sediments. *Jour. Acoust. Soc. Am.* 72, 1891-1904.
- Hatori, T. 1974. Source of large Tsunamis in southwest Japan. *Zishin*, 27, 10-24.
- Hilde, T.W.C. 1983. Sediment subduction versus accretion around the Pacific. *Tectonophysics*, 99, 381-397.

- Hoshino, K., Koide, H., Inami, K., Iwamura, S., and Mitsui, S. 1972. Mechanical properties of Japanese Tertiary sedimentary rocks under high confining pressures. *Geol. Surv. Japan Rep.* 244, 200 pp.
- Hubbert, M.K., and Rubey, W.W. 1959. Role of fluid pressure in mechanics of overthrust faulting, I, Mechanics of fluid-filled solids and its application to overthrust faulting. *Geol. Soc. Am. Bull.* 70, 115-166.
- Huchon, P., Lyberis, N., Angelier, J., Le Pichon, X., and Renard, V. 1982. Tectonics of the Hellenic Trench: A synthesis of sea-beam and submersible observations. *Tectonophysics*, 86, 69-112.
- Ingle, J.C., Karig, D.E., et al. 1975a. Site 297. In Ingle, J.C., Karig, D.E., et al., *Init. Repts. DSDP*, Washington (U.S. Govt. Printing Office), 31, 275-316.
- Ingle, J.C., Karig, D.E., et al. 1975b. Site 298. In Ingle, J.C., Karig, D.E., et al., *Init. Repts. DSDP*, Washington (U.S. Govt. Printing Office), 31, 317-350.
- Kagami, H. 1986. The accretionary prism of the Nankai Trough off Shikoku, southwestern Japan. In Kagami, H., Karig, D.E. et al., *Init. Repts. DSDP*, Washington (U.S. Govt. Printing Office), 87, 941-953.
- Kagami, H., and Karig, D.E., et al. 1986. Site 582. In Kagami, H., Karig, D.E. et al., *Init. Repts. DSDP*, Washington (U.S. Govt. Printing Office), 87, 35-71.
- Kanamori, H. 1971. Faulting of the Great Kanto earthquake of 1923 as revealed by seismological data. *Bull. Earthq. Res. Inst.* 49, 13-18.
- Karig, D.E. 1974. Tectonic erosion at trenches. *Earth Planet Sci. Lett.* 21, 209-212.
- Karig, D.E., and Angevine, C.L. 1986. Geologic constraints on subduction rates in the Nankai Trough. In Kagami, H., Karig, D.E. et al., *Init. Repts. DSDP*, Washington (U.S. Govt. Printing Office), 87, 789-796.
- Karig, D.E., Lundberg, N. 1990. Deformation bands from the toe of the Nankai accretionary prism. *J. Geophys. Res.* 95, 9099-9110.

- Kinoshita, H. and Yamano, M. 1985. The heat flow anomaly in the Nankai Trough area. In Kagami, H., Karig, D.E., et al., *Init. Repts. DSDP*, Washington (U.S. Govt. Printing Office), 87, 737-743.
- Klein, G. deV., and Kobayashi, K. 1980. Geological summary of the North Philippine Sea based on Deep Sea Drilling Project Leg 58 Results. In Klein, G. deV., and Kobayashi, K., et al., *Init. Repts. DSDP*, Washington (U.S. Govt. Printing Office), 58, 951-961.
- Kobayashi, K., and Nakada, M. 1978. Magnetic anomalies and tectonic evolution of the Shikoku interarc basin. *Jour. Phys. Earth.* 26, 391-402.
- Kobayashi, K., Le Pichon, X., et al. 1989. Quantitative evaluation of large-scale fluid venting on the frontal portion of the eastern Nankai accretionary prism using the 6000 m Nautilie submersible. *EOS*, 70, 1381.
- Lallemand, S., and Le Pichon, X. 1987. Coulomb wedge model applied to the subduction of seamounts in the Japan Trench. *Geology*, 15, 1065-1069.
- Langseth, M.G., and Moore, J.C. 1990. Introduction to special section on the role of fluids in sediment accretion, deformation, diagenesis, and metamorphism in subduction zones. *J. geophys. Res.* 95, 8737-8742.
- Leggett, J. K., Aoki, Y. and Toba, T. 1985. Transition from frontal accretion to underplating in a part of the Nankai Trough accretionary complex off Shikoku (SW Japan) and extensional features on the lower trench slope. *Mari.Petrol. Geol.* 2, 131-141.
- Le Pichon, X., Kobayashi, K., Cadet, J.P., Iiyama, T., Nakamura, K., Pautot, G., Renard, V., and Kaiko Scientific Crew. 1987a. Project Kaiko - Introduction. *Earth Planet Sci. Lett.* 83, 183-185.
- Le Pichon, X., Iiyama, T., Chamley, H., Charvet, J., Faure, M., Fujimoto, H., Furuta, T., Ida, Y., Kagami, H., Lallemand, S., Leggett, J., Murata, A., Okada, H., Rangin, C., Renard, V., Taira, A. and Tokuyama, H. 1987b. Nankai Trough and the fossil Shikoku Ridge, results of Box 6 Kaiko survey. *Earth Planet Sci. Lett.* 83, 186-198.

- Le Pichon, X., Foucher, J., Boulegue, J., Henry, P., Lallemand, S., Benedetti, M., Avedik, F., and Marippt, A. 1990. Mud volcano field seaward of the Barbados accretionary complex: A submersible survey. *J. Geophys. Res.* **95**, 8931-8944.
- Masce, A., and Moore, J.C. 1990. ODP Leg 110: Tectonic and hydrogeologic synthesis. *Proc. ODP, Init. Rept.*, **110**: Collage Station, TX (Ocean Drilling Program). 409-422.
- Mauffret, A., Westbrook, G. K., Truchan, M., and Ladd, J. 1984. The relief of the oceanic basement and the structure of the front of the accretionary complex in the region of sites 541, 542, and 543. In Biju-Duval, B., Moore, J.C. et al., *Init. Repts. DSDP*, Washington (U.S. Govt. Printing Office), **78A**, 49-62.
- Minshull, T., and White, R. 1989. Sediment compaction and fluid migration in Makran Accretionary Prism. *J. Geophys. Res.* **94**, 7387-7402.
- Moore, J.C., Biju-Duval, B., Bergen, J.A. and others, 1982. Offscraping and underthrusting of sediment at the deformation front of the Barbados Ridge: Deep Sea Drilling Project Leg 78A. *Geol. Soc. Am. Bull.* **93**, 1065-1077.
- Moore, G.F., Shipley, T.H., Stoffa, P.L., Karig, D.E., Taira, A., Kuramoto, S., Tokuyama, H., and Suyehiro, K. 1990. Structural of the Nankai Trough accretionary zone from multichannel seismic reflection data. *J. Geophys. Res.* **95**, 8753-8765.
- Moore, J. C. 1989. Tectonics and hydrogeology of accretionary prisms: role of the decollement zone. *Jour. Structural Geol.* **11**, 95-106.
- Mulugeta, G., and Koyi, H. 1987. Three-dimensional geometry and kinematics of experimental piggy back thrusting. *Geology*, **15**, 1052-1056.
- Nagihara, S., Kinoshita, H., Yamano, M. 1989. On the high heat flow in the Nankai Trough area - a simulation study on a heat rebound process. *Tectonophysics*, **161**, 33-41.

- Nasu, N., Tomoda, Y., et al. 1982. Multichannel seismic reflection data across Nankai Trough, *Ocean Research Institute, University of Tokyo, IPOD-Japan Basic Ser. 4.*
- Ohta, S. and Laubier, L. 1987. Deep biological communities in the subduction zone of Japan from bottom photographs taken during "Nautile" dives in the Kaiko project. *Earth Planet Sci. Lett.* 83, 329-342.
- Platt, J.P. 1990. Thrust mechanics in highly overpressed accretionary wedges. *J. Geophys. Res.* 95, 9025-9034.
- Ranken, B., Cardwell, R.K. and Karig, D. E. 1984. Kinematics of the Philippine sea plate. *Tectonics*, 3, 555-575.
- Seely, D.R. 1977. The significance of landward vergence and oblique structural trends on trench inner slopes. In Talwani, M., and Pitman III, W.C. (Eds), *Island Arcs, Deep Sea Trenches and Back-Arc Basins, Maurice Ewing Ser. vol. 1.* AGU, Washington, pp. 187-198.
- Seno, T. 1977. The instantaneous rotation vector of the Philippine Sea plate relative to the Eurasian plate. *Tectonophysics*, 42, 209-226.
- Shih, T.C. 1980. Magnetic lineations in the Shikoku Basin. In Klein, G. deV., Kobayashi, K., et al., *Init. Repts. DSDP*, Washington (U.S. Govt. Printing Office), 58, 783-788.
- Silver, E.A. 1971. Transitional tectonics and late Cenozoic structure of the continental margin off northern California. *Geol. Soc. Am. Bull.* 82, 1-22.
- Soh, W. 1988. Description of piston core samples of KH86-5 cruise. *Preliminary Report of the Hakuho Maru cruise KH86-5: ODP Site Survey.* Ocean Research Institute, University of Tokyo, 103-159.
- Taira, A. and Niitsuma, N. 1985. Turbidite sedimentation in the Nankai Trough as interpreted from magnetic fabric, grain size, and detrital modal analyses. In Kagami, H. and Karig, D. E. et al., *Init. Repts. DSDP*, Washington (U.S. Govt. Printing Office), 87, 611-632.

- Taira, A., Hill, I., Firth, J. et al. in press. *Proc. ODP, Init. Rept.*, 131: Collage Station, TX (Ocean Drilling Program).
- Tatsumi, Y. 1982. Origin of High-magnesian Andesites in the Setouchi Volcanic Belt, Southwest Japan, 2. Melting Phase Relation at High Pressure. *Earth Planet Sci. Lett.* 60, 305-317.
- Uyeda, S. 1972. Heat flow. In Miyamura, S., and Uyeda, S. (Eds.), *The Crust and Upper Mantle of the Japanese Area* (Part 1, Geophysics) : Tokyo (Earthquake Research Institute, University of Tokyo), pp. 97-105.
- Watanabe, T., Langseth, M., and Anderson, R.N. 1977. Heat flow in back-arc basins of the western Pacific. In Talwani, M., and Pitman, W.C., III (Eds.), *Island Arcs, Deep Sea Trenches, and Backarc Basins: Washington* (Am. Geophys. Union), Maurice Ewing Series, 1, 137-167.
- Watanabe, M. 1988. Deep-sea photography, system, operation and observation. *Preliminary Report of the Hakuho Maru cruise KH86-5: ODP Site Survey*. Ocean Research Institute, University of Tokyo, 88-101.
- Westbrook, G. K., and Smith, M. J. 1983. Long decollements and mud volcanoes: Evidence from the Barbados Ridge Complex for the role of high pore-fluid pressure in the development of an accretionary complex. *Geology*, 11, 279-283.
- Yamano, M., Uyeda, S., Aoki, Y., and Shipley, T.H. 1982. Estimates of heat flow derived from gas hydrates. *Geology*, 10, 339-343.
- Yamano, M., Honda, S., and Uyeda, S. 1984. Nankai Trough: A hot trench ?. *Marine Geophysical Researches*, 6, 187-203.
- Yamazaki, T. and Okamura, Y. 1989. Subduction seamounts and deformation of overriding forearc wedge around Japan. *Tectonophysics*, 160, 207-229.
- Yoshii, T. 1979. Compilation of geophysical data around the Japanese Islands (1). *Bull. Earthquake Res. Inst. Univ. Tokyo*, 54, 75-117.

Zhao, W.L., Davis, D.M., Dahlen, F.A., and Suppe, J. 1986. Origin of convex accretionary wedges: evidence from Barbados. *J. Geophys. Res.* **10**, 10246-10258.

FIGURES

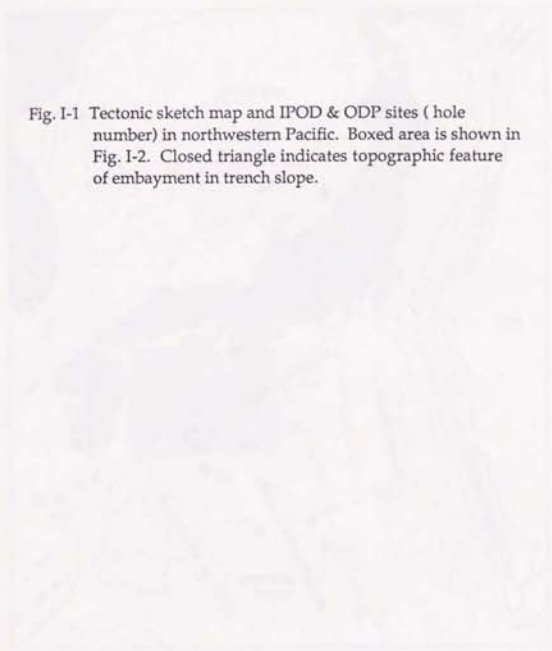
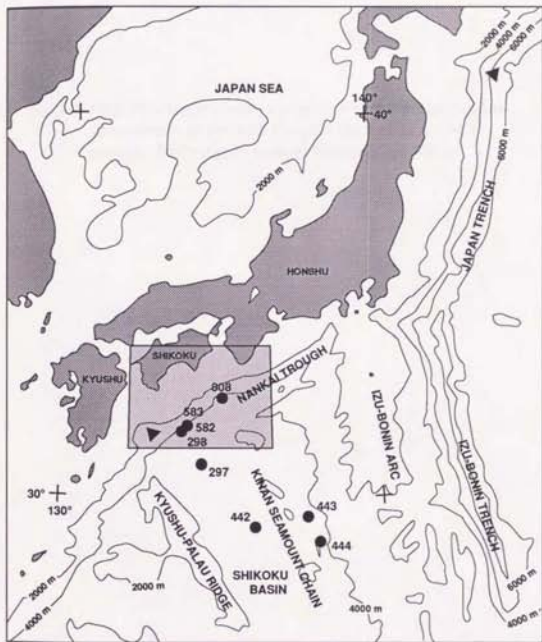


Fig. I-1 Tectonic sketch map and IPOD & ODP sites (hole number) in northwestern Pacific. Boxed area is shown in Fig. I-2. Closed triangle indicates topographic feature of embayment in trench slope.



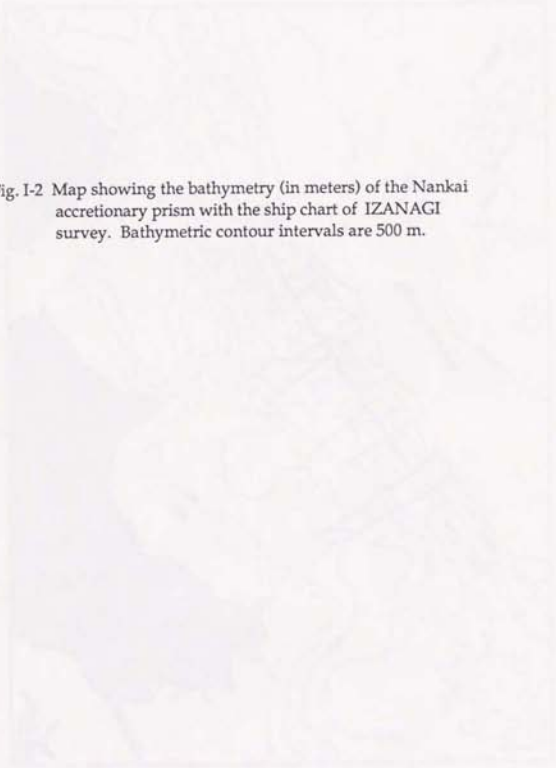


Fig. 1-2 Map showing the bathymetry (in meters) of the Nankai accretionary prism with the ship chart of IZANAGI survey. Bathymetric contour intervals are 500 m.

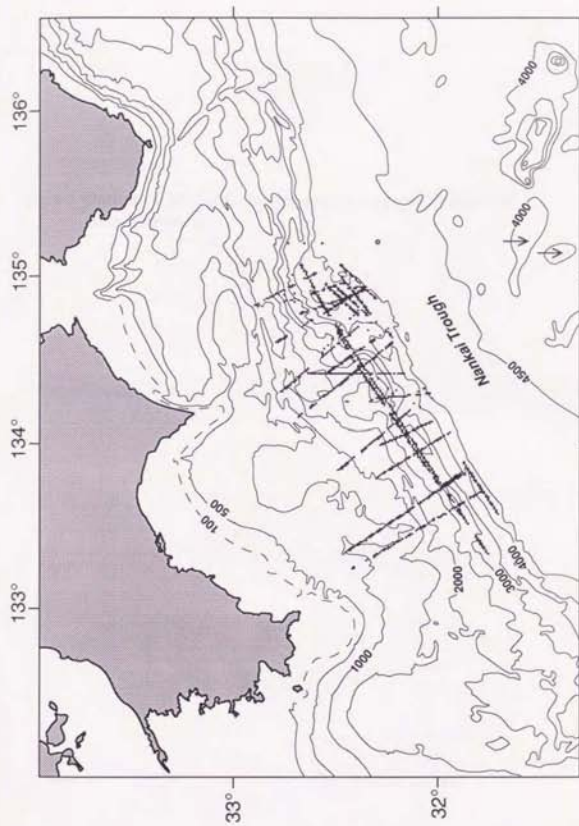
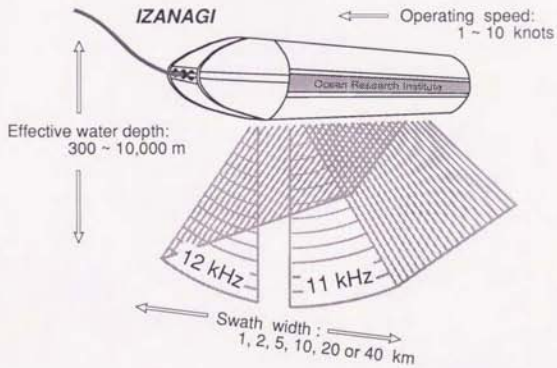
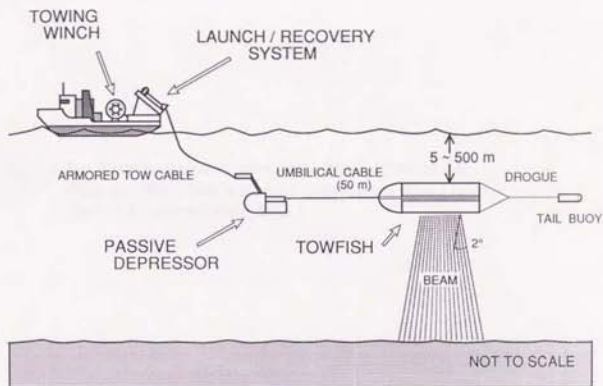


Fig. 1-3 Outline of IZANAGI towing system and specifications of tow fish system.



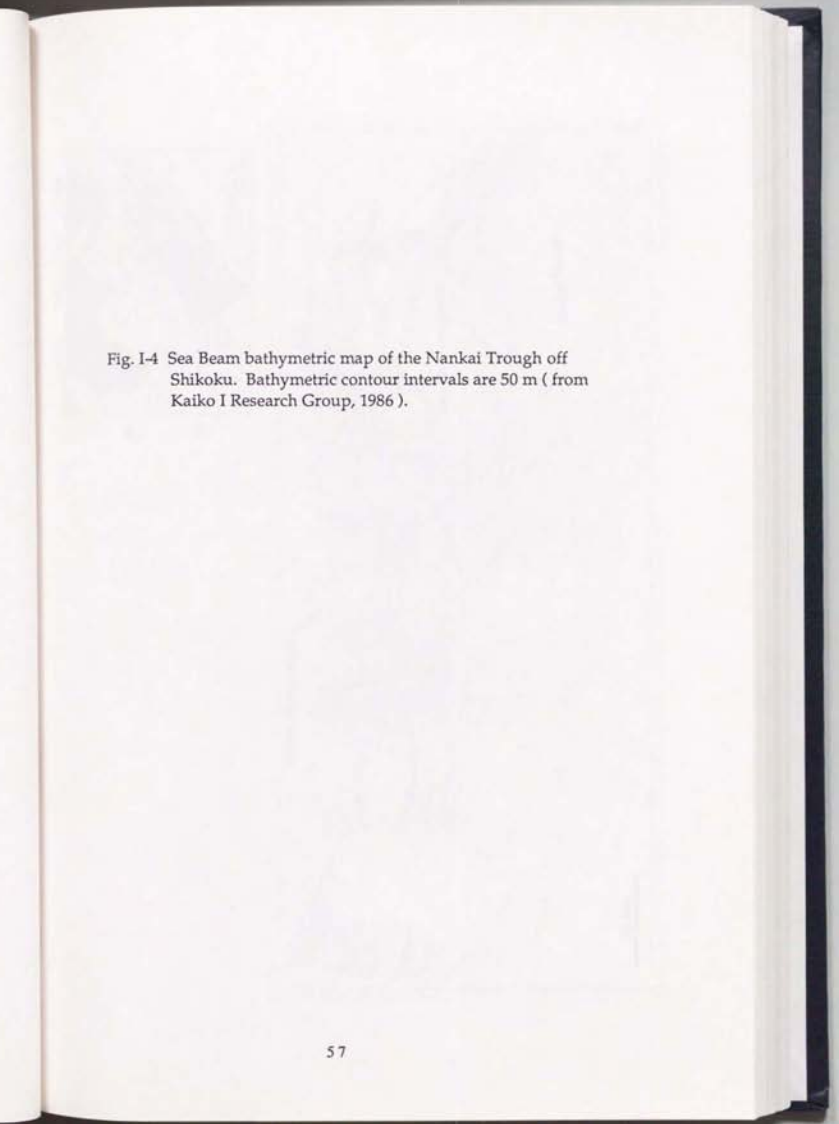


Fig. I-4 Sea Beam bathymetric map of the Nankai Trough off Shikoku. Bathymetric contour intervals are 50 m (from Kaiko I Research Group, 1986).

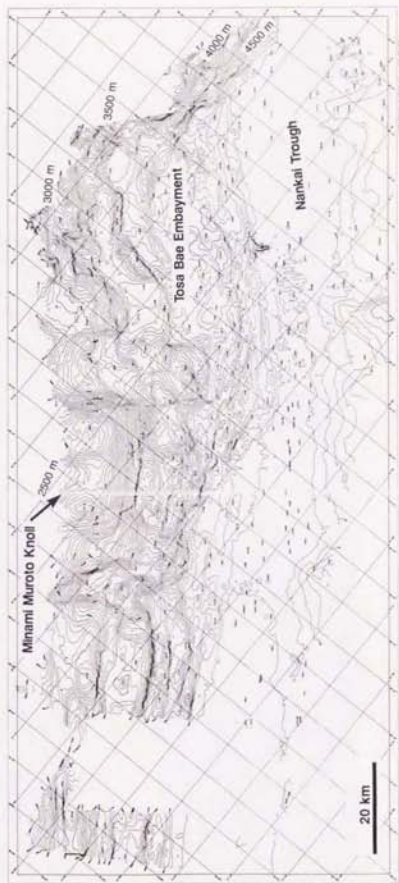


Fig. 1-5 Migrated multichannel seismic reflection profile of line NT62-8, located on Fig. A3.

TWT (s)
5.0

1300

1500

1700

1900

NT52-B

2 km

NANAKI TROUGH

6.0

7.0

8.0

OCEANIC BASEMENT

DECOLLEMENT

2100

2300

2500

2700

2900

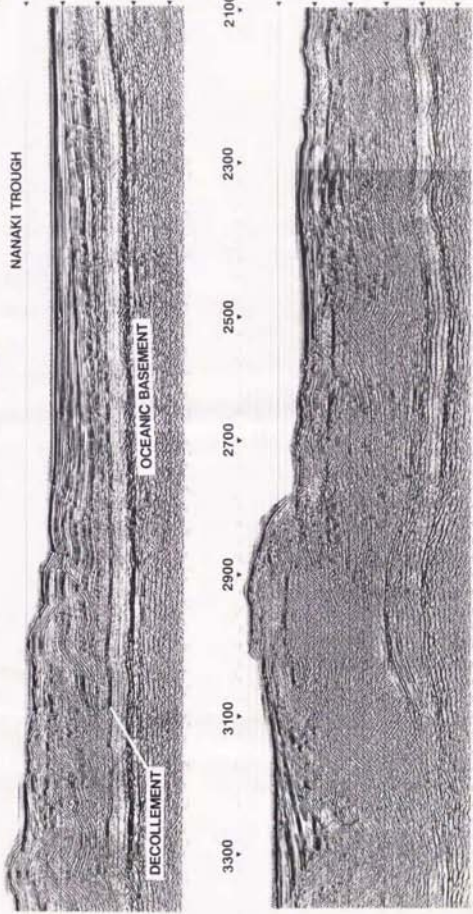
3100

3300

6.0

7.0

8.0



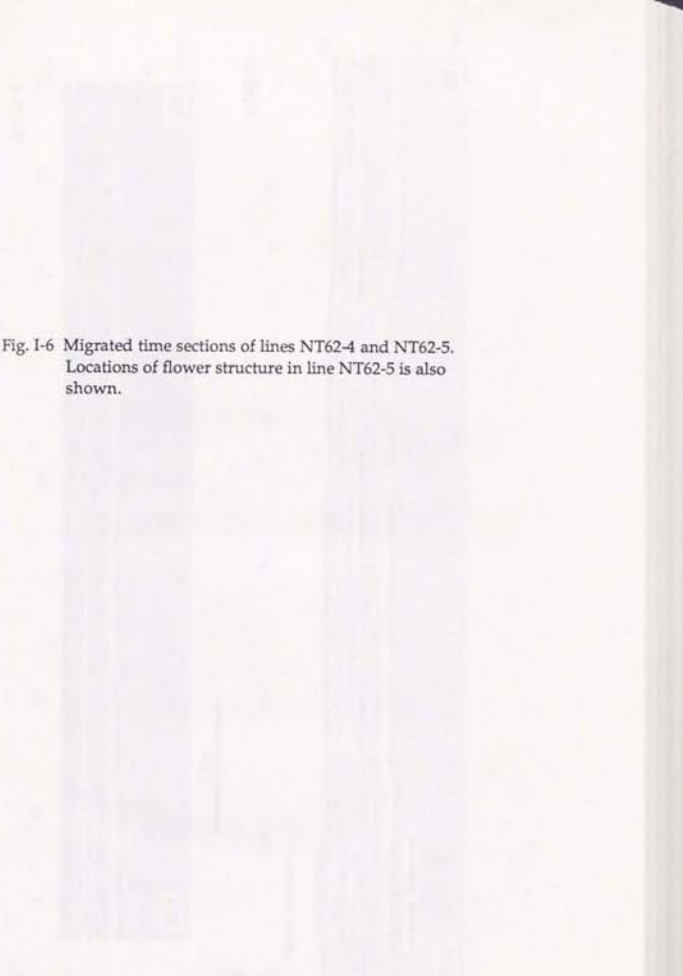


Fig. 1-6 Migrated time sections of lines NT62-4 and NT62-5.
Locations of flower structure in line NT62-5 is also
shown.

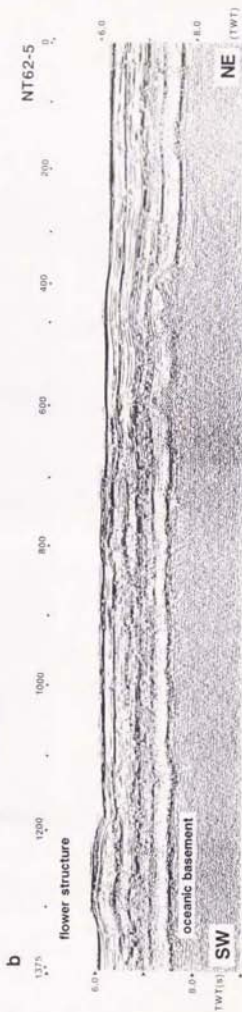
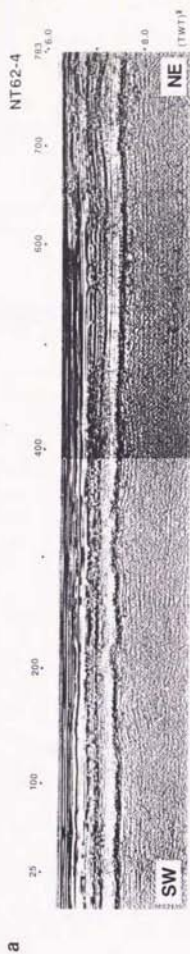


Fig. 1-7 Migrated time sections of lines NT62-6 and NT62-7.

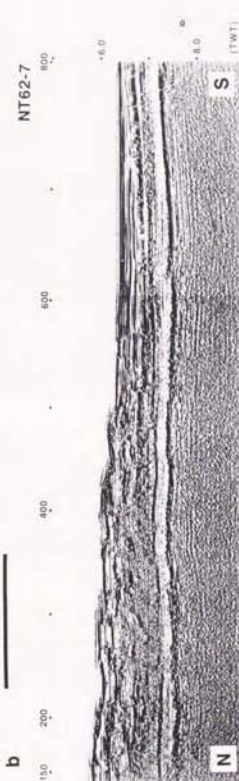
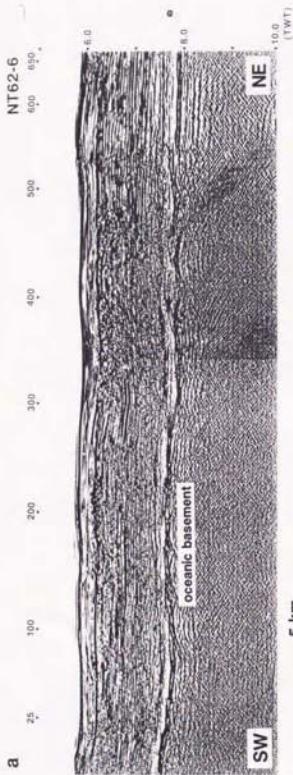


Fig. I-8 Migrated time sections of lines 55-1 and 55-2 (JAPEX unpublished data). Both lines are located in the Tosa Bae Embayment.

Fig. 1-9 Migrated time sections of lines NT62-1 and NT62-2.
Profiles show typical shape of the Nankai accretionary
prism.

NT62-1

975

600

400

200

100

25

5 km

+4.0

slope basin

Nankai Trough

+8.0

SE

NW

NT62-2

425

600

800

1000

1100

+4.0

Nankai Trough

+6.0

+8.0

SE

NW

decollement

oceanic basement

a

b

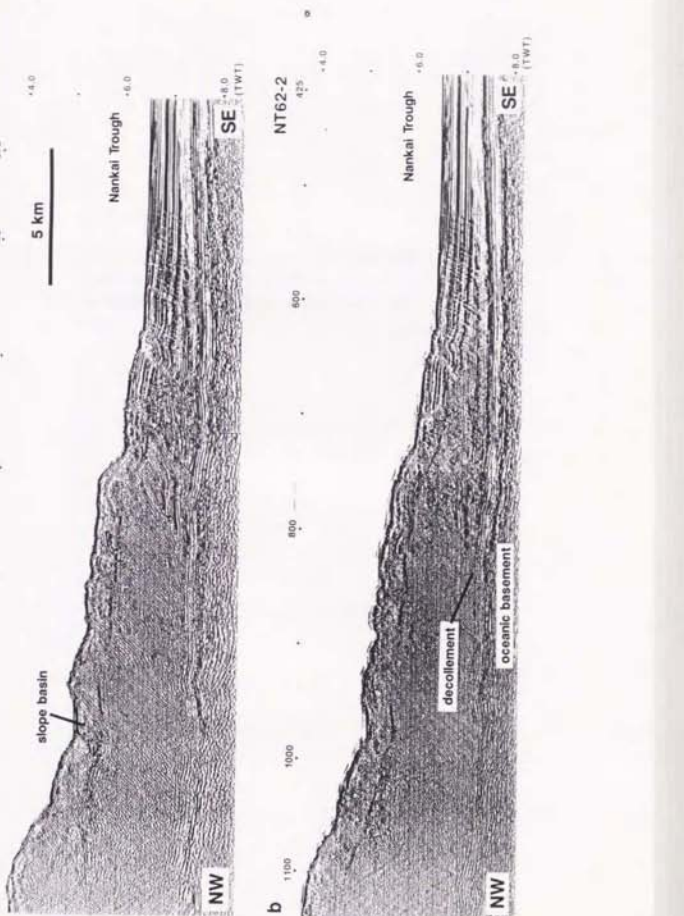


Fig. I-10 Migrated time sections of lines 55-7 and 55-8 (JAPEX unpublished data). Both lines are located off Cape Ashizuri. Landslides occur at the upper slope of the prism.

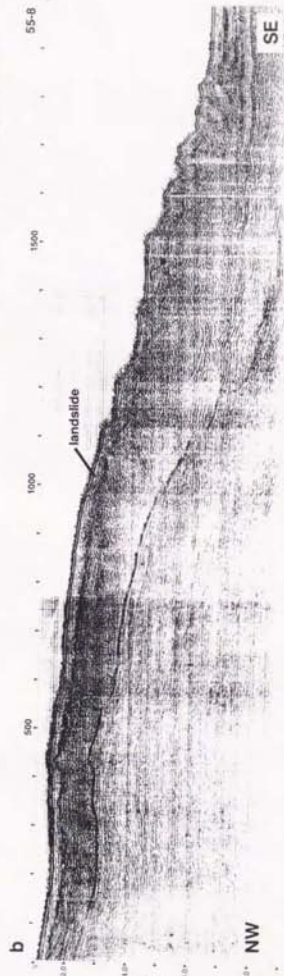
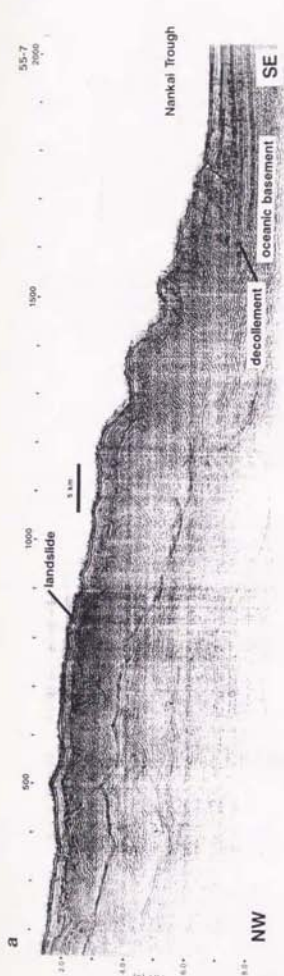


Fig. I-11 Transverse migrated time sections of lines 55-A and 55-A-1 along the middle slope of the prism (JAPEX unpublished data).

a

Minami Muroto Knoll

normal fault

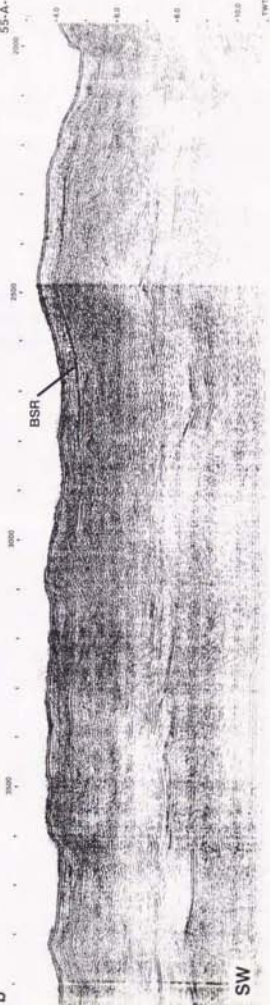
55-A



b

55-A-1

BSR



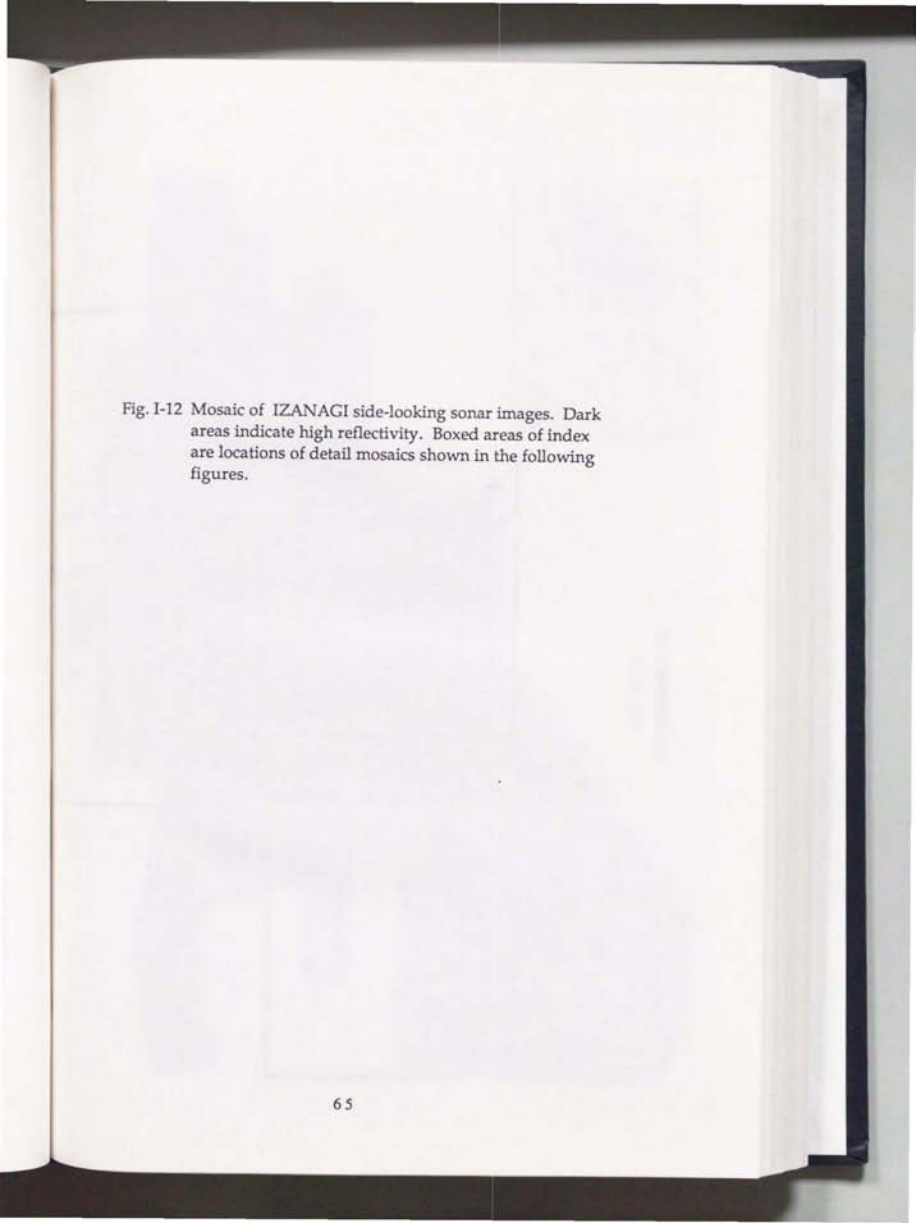


Fig. I-12 Mosaic of IZANAGI side-looking sonar images. Dark areas indicate high reflectivity. Boxed areas of index are locations of detail mosaics shown in the following figures.

Fig. 17

Fig. 19

Fig. 18

Fig. 21

Fig. 16

20 km

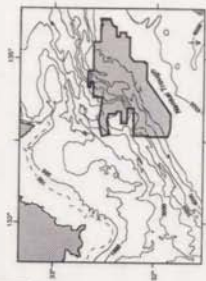


Fig. 17

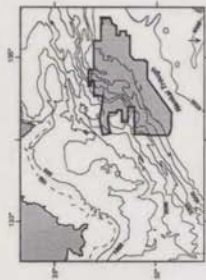
Fig. 19

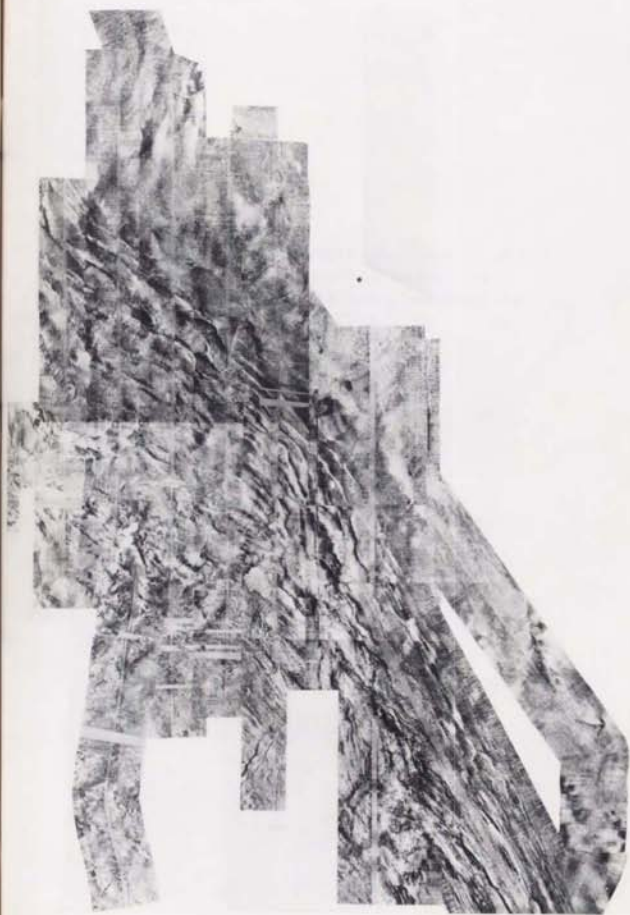
Fig. 18

Fig. 21

Fig. 16

20 km





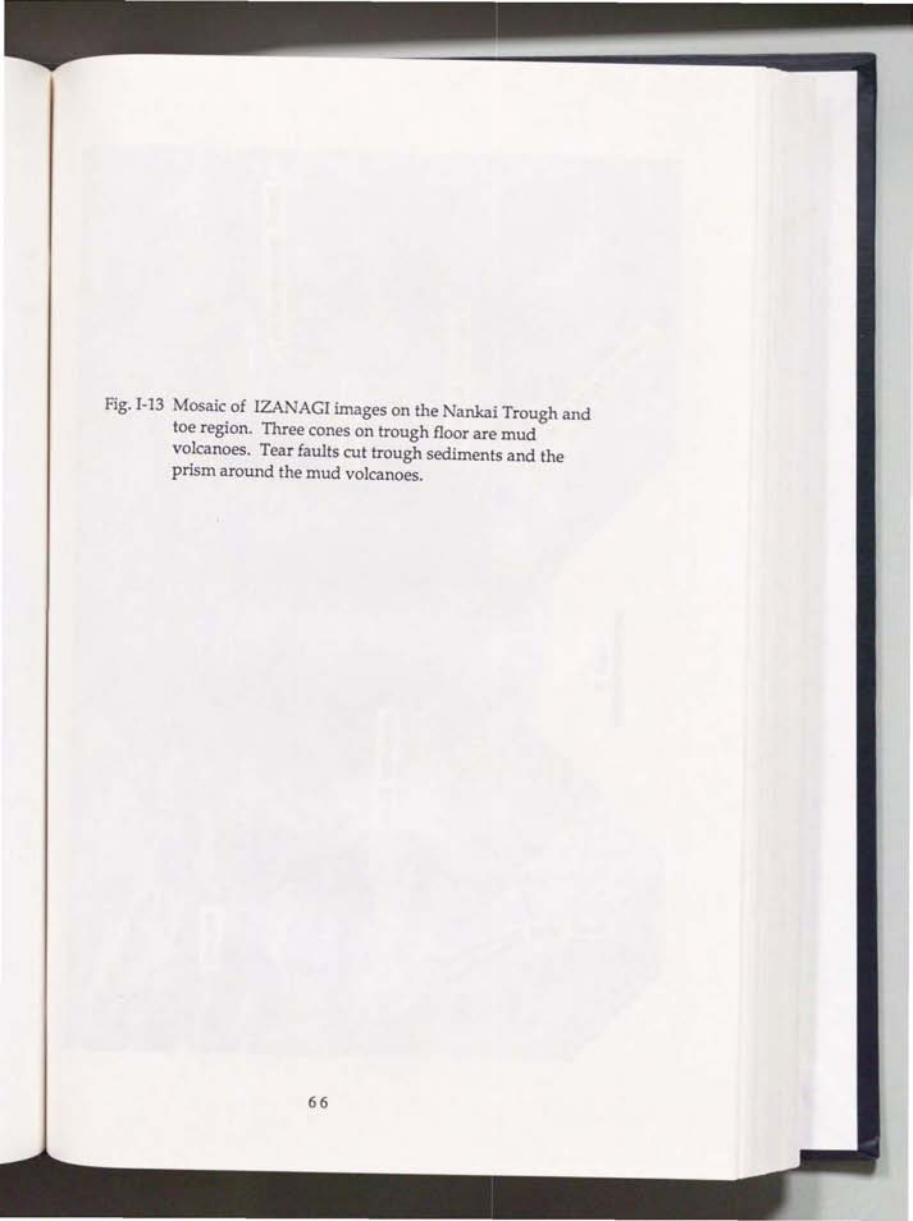
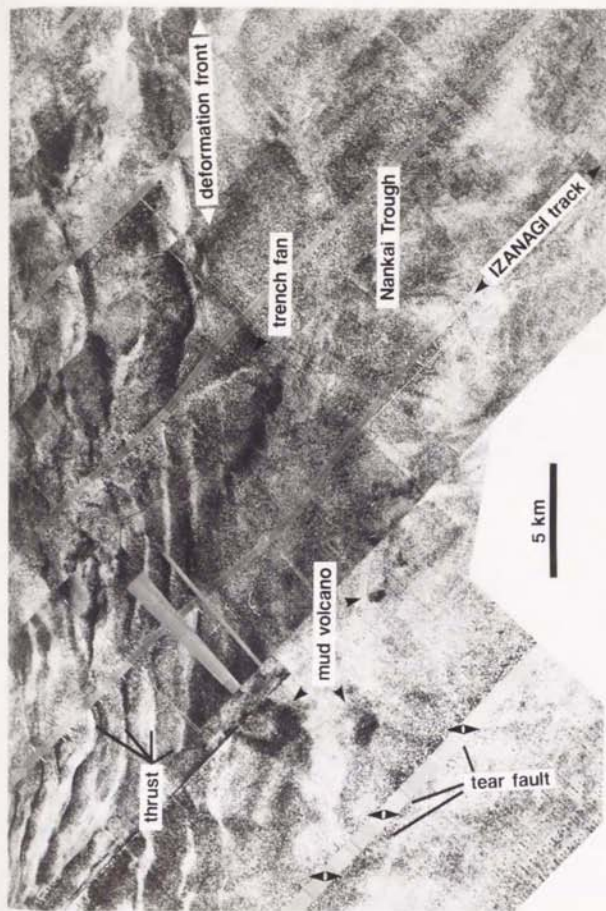


Fig. I-13 Mosaic of IZANAGI images on the Nankai Trough and toe region. Three cones on trough floor are mud volcanoes. Tear faults cut trough sediments and the prism around the mud volcanoes.



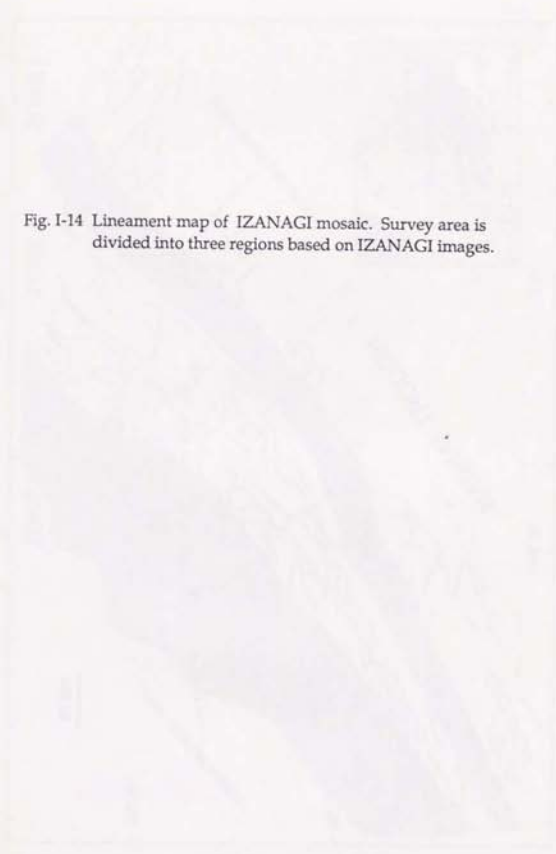
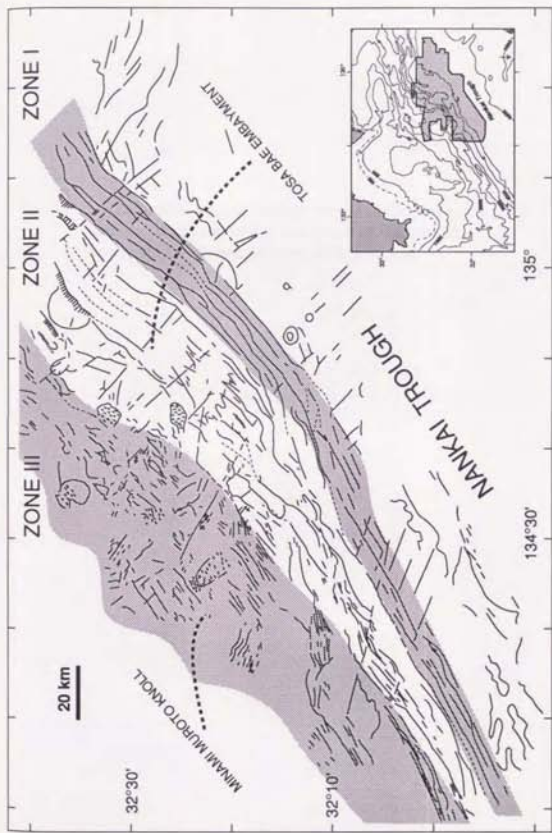
A faint, large-scale lineament map of the IZANAGI mosaic is visible in the background of the page. The map shows a complex network of linear features, likely fractures or faults, distributed across the survey area. The features are most prominent in the central and lower portions of the map. The map is divided into three distinct regions, as indicated by the caption, though the boundaries between these regions are not clearly defined in the image. The overall appearance is that of a technical drawing or map, rendered in a light, almost ghostly tone.

Fig. I-14 Lineament map of IZANAGI mosaic. Survey area is divided into three regions based on IZANAGI images.



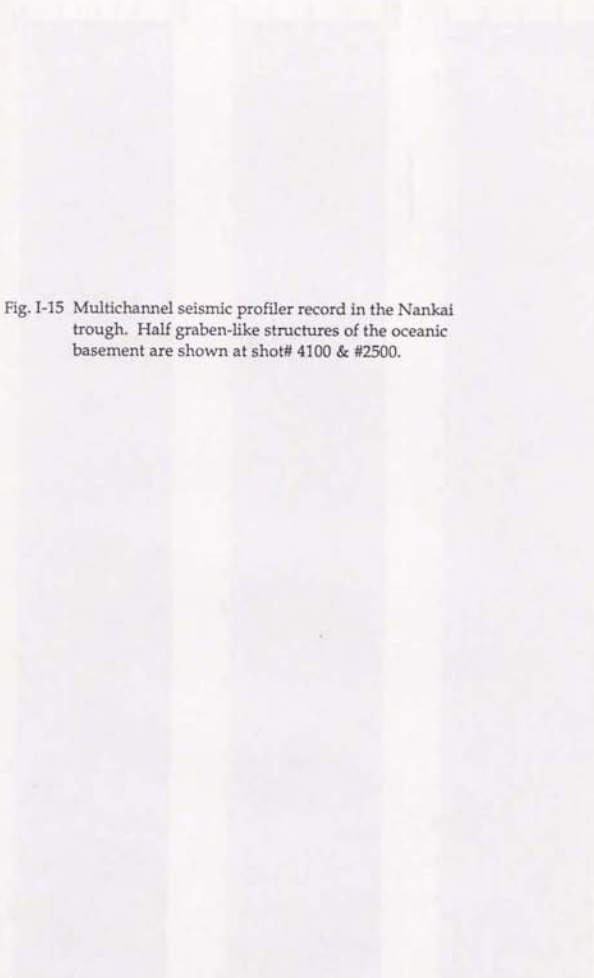
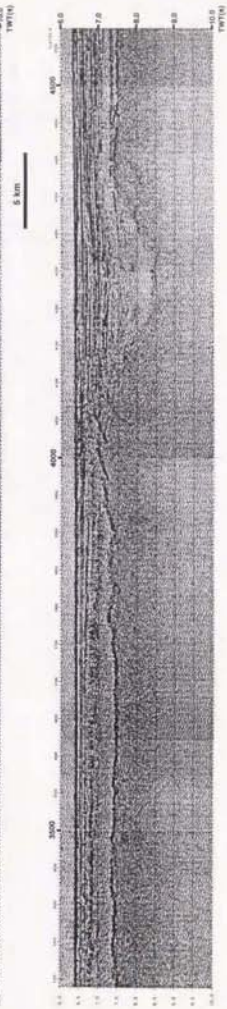


Fig. I-15 Multichannel seismic profiler record in the Nankai trough. Half graben-like structures of the oceanic basement are shown at shot# 4100 & #2500.



1000 ft

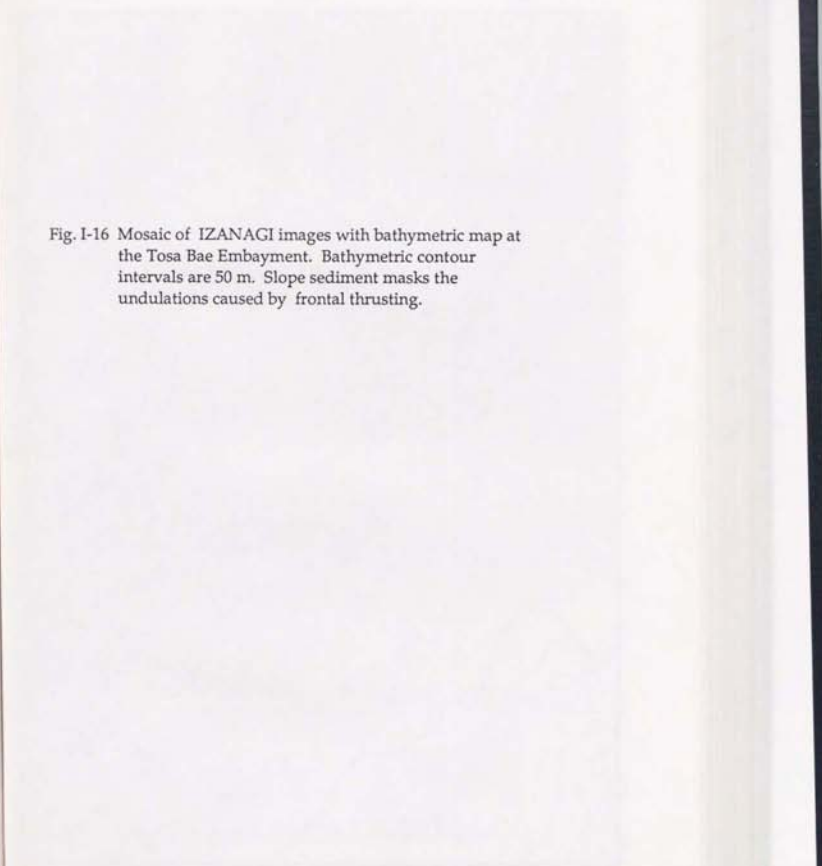
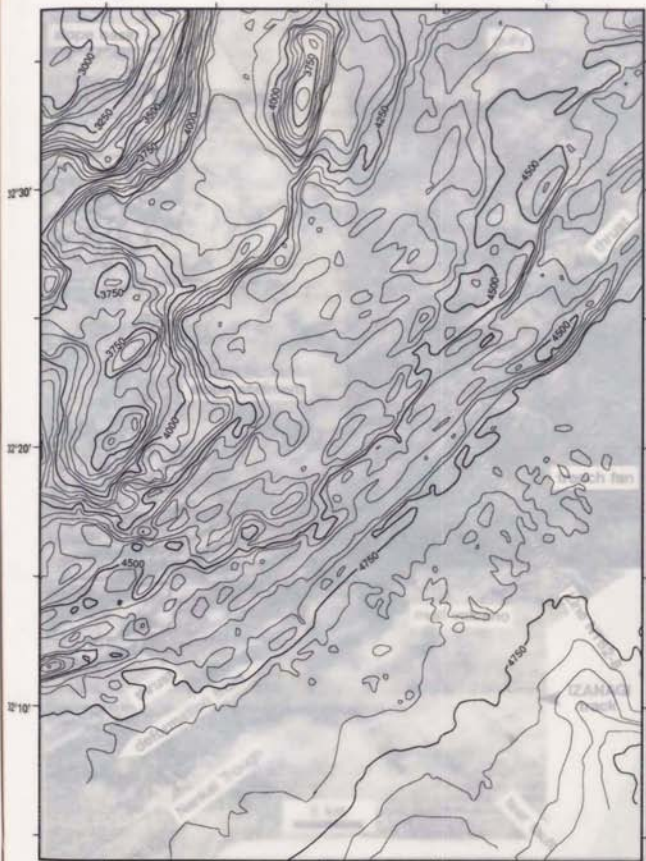


Fig. I-16 Mosaic of IZANAGI images with bathymetric map at the Tosa Bae Embayment. Bathymetric contour intervals are 50 m. Slope sediment masks the undulations caused by frontal thrusting.

134°40'

134°50'

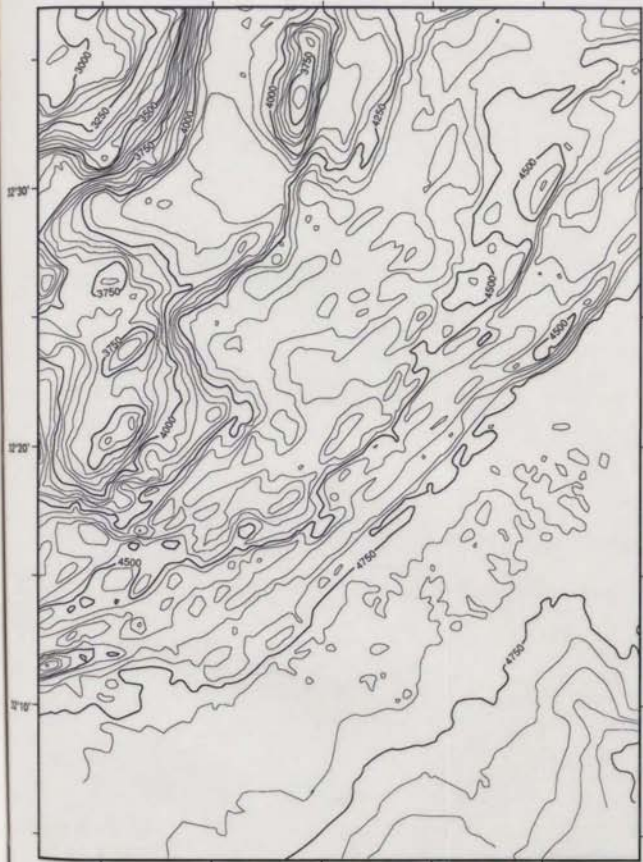
135°



134°40'

134°50'

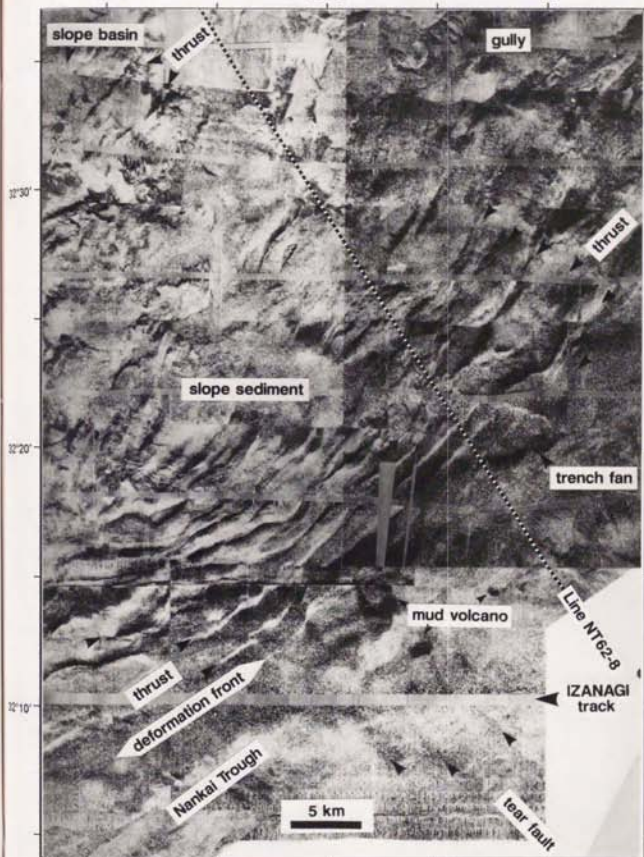
135°



134°40'

134°50'

135°



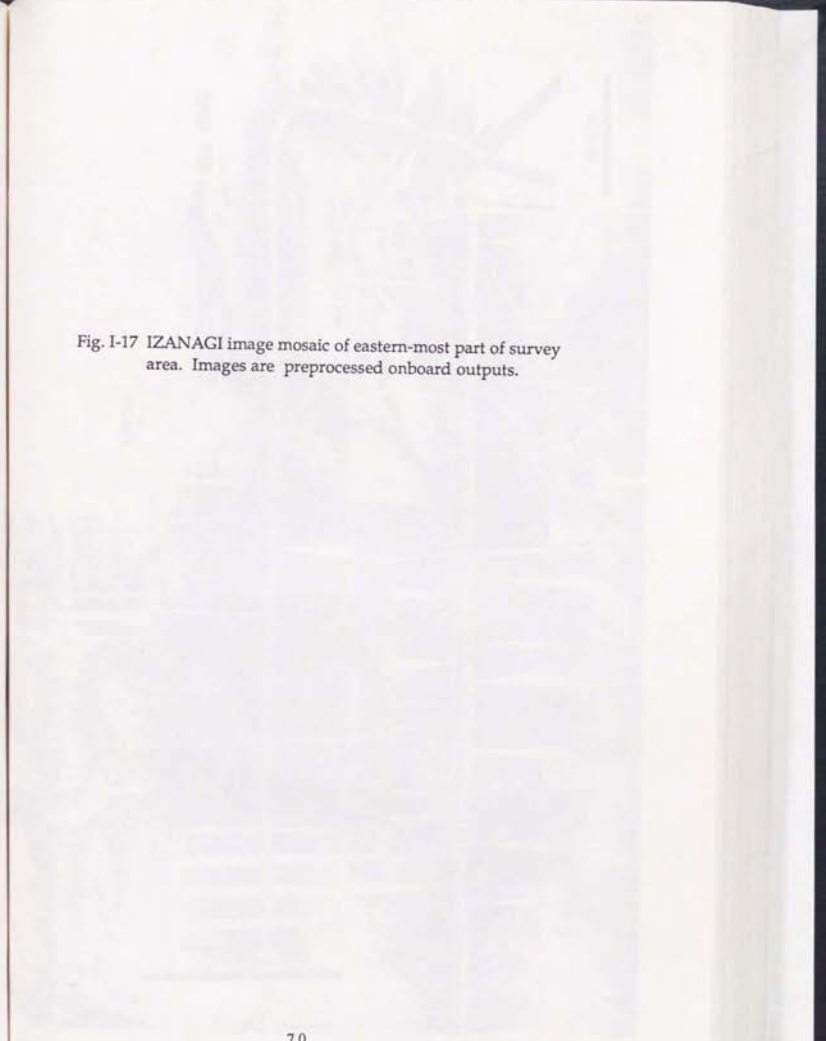
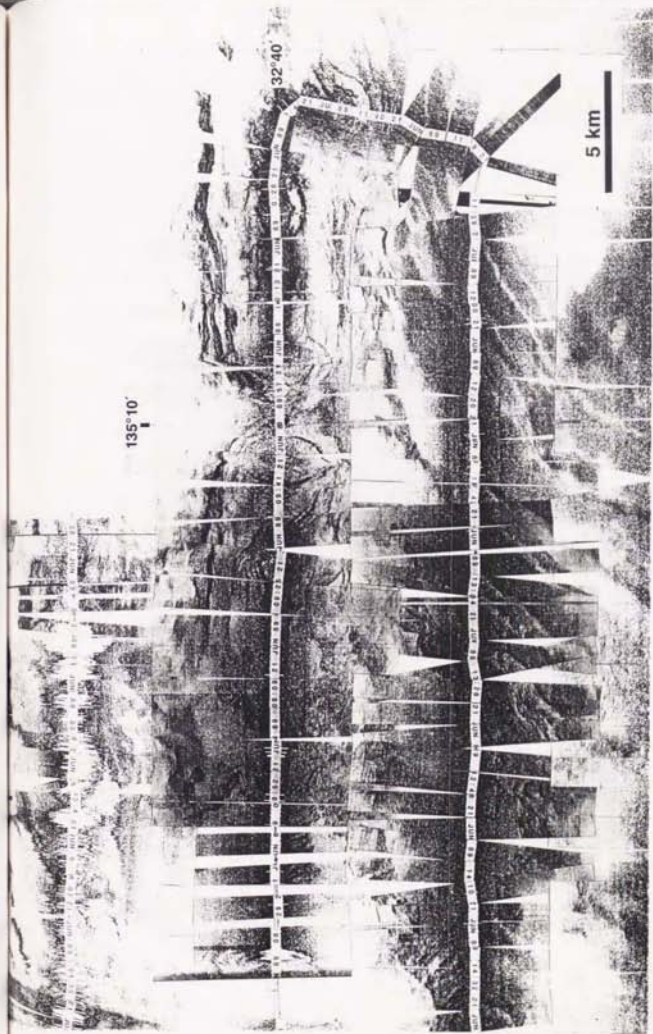


Fig. I-17 IZANAGI image mosaic of eastern-most part of survey area. Images are preprocessed onboard outputs.



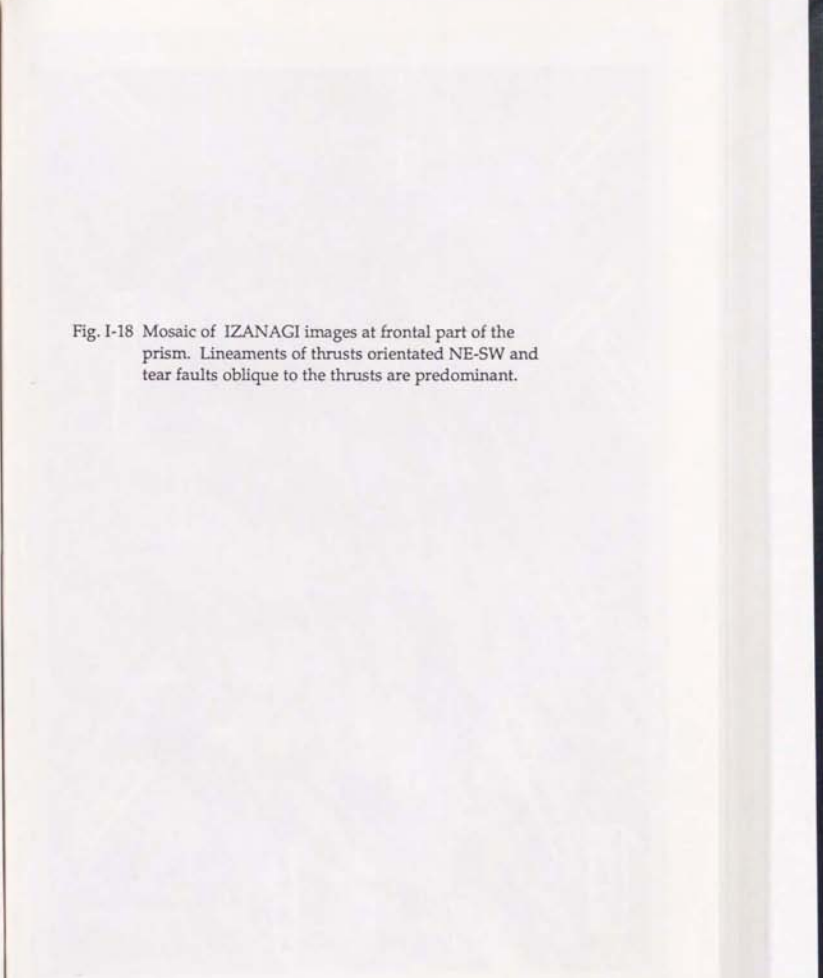


Fig. I-18 Mosaic of IZANAGI images at frontal part of the prism. Lineaments of thrusts orientated NE-SW and tear faults oblique to the thrusts are predominant.



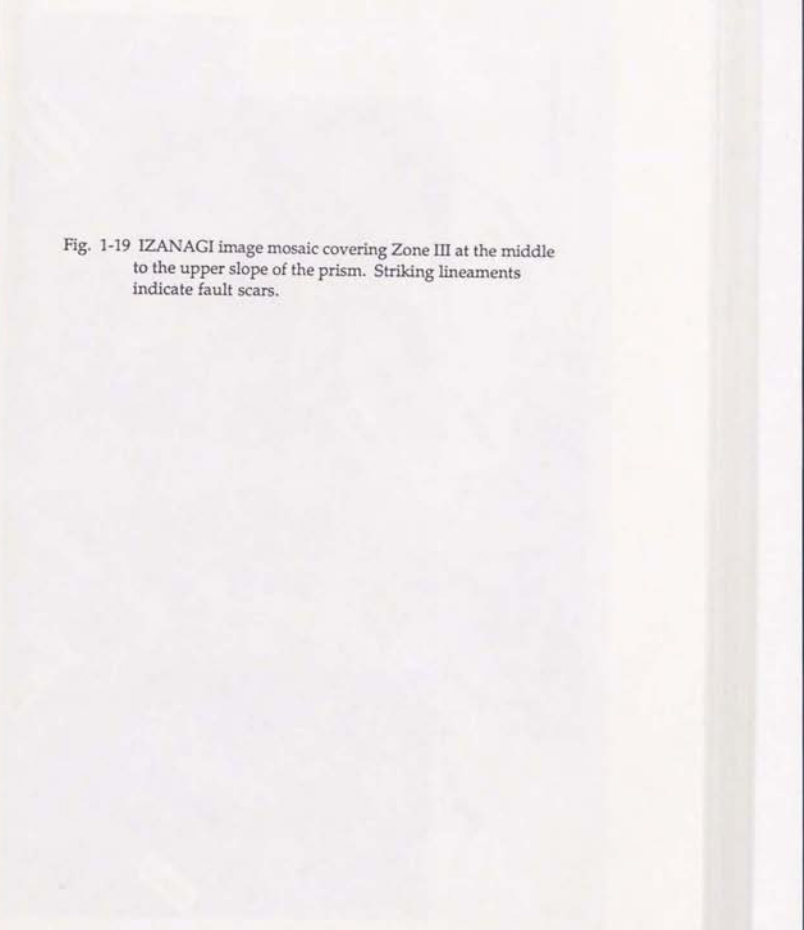


Fig. 1-19 IZANAGI image mosaic covering Zone III at the middle to the upper slope of the prism. Striking lineaments indicate fault scars.

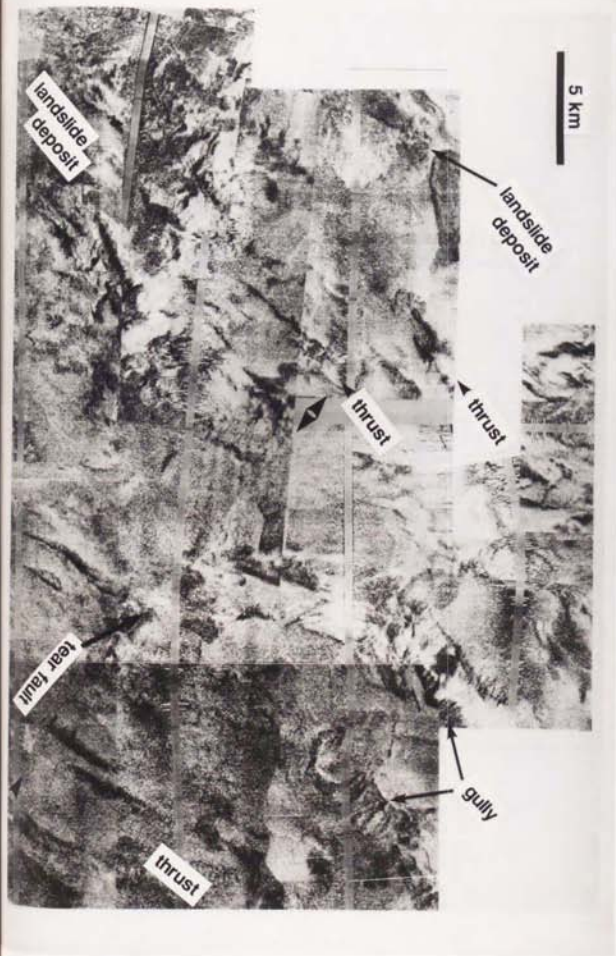
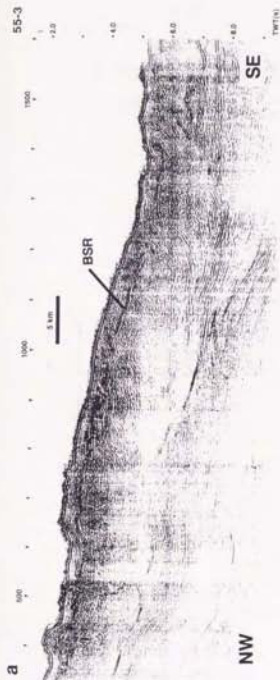


Fig. I-20 Migrated time sections of lines 55-3 and 55-4 (JAPEX unpublished data). Line 55-4 is across small embayment area.



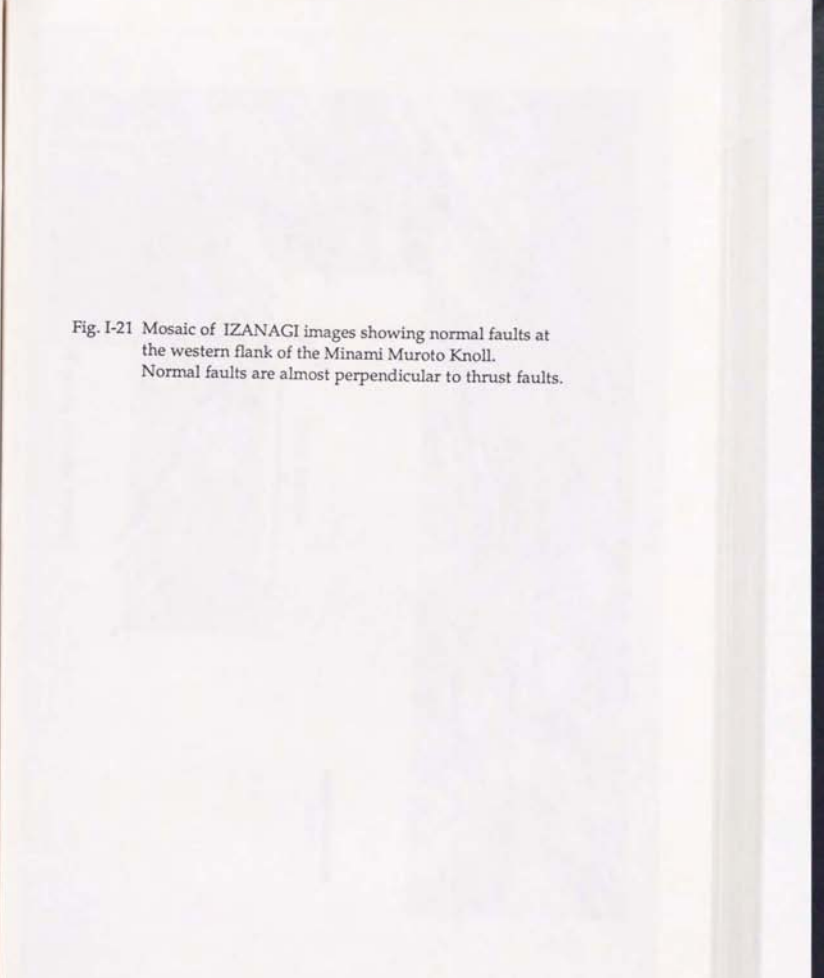
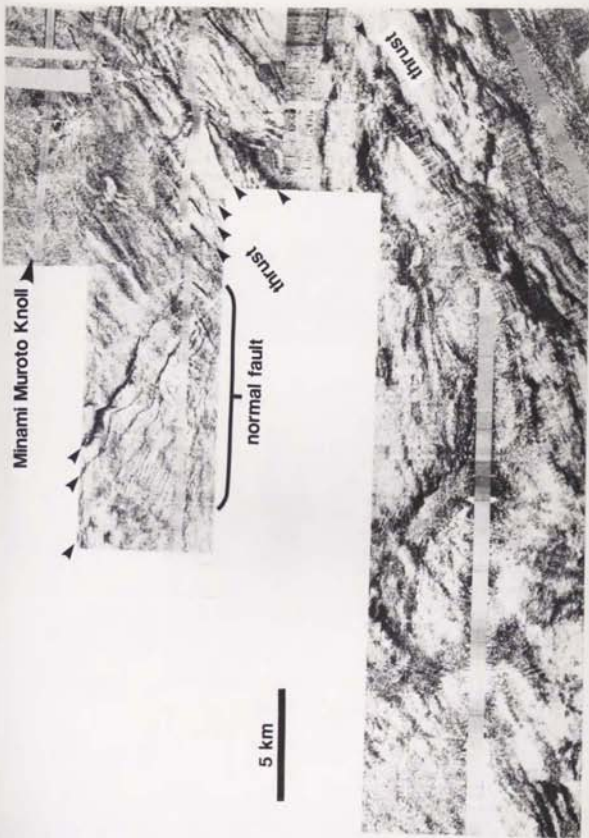


Fig. I-21 Mosaic of IZANAGI images showing normal faults at
the western flank of the Minami Muroto Knoll.
Normal faults are almost perpendicular to thrust faults.



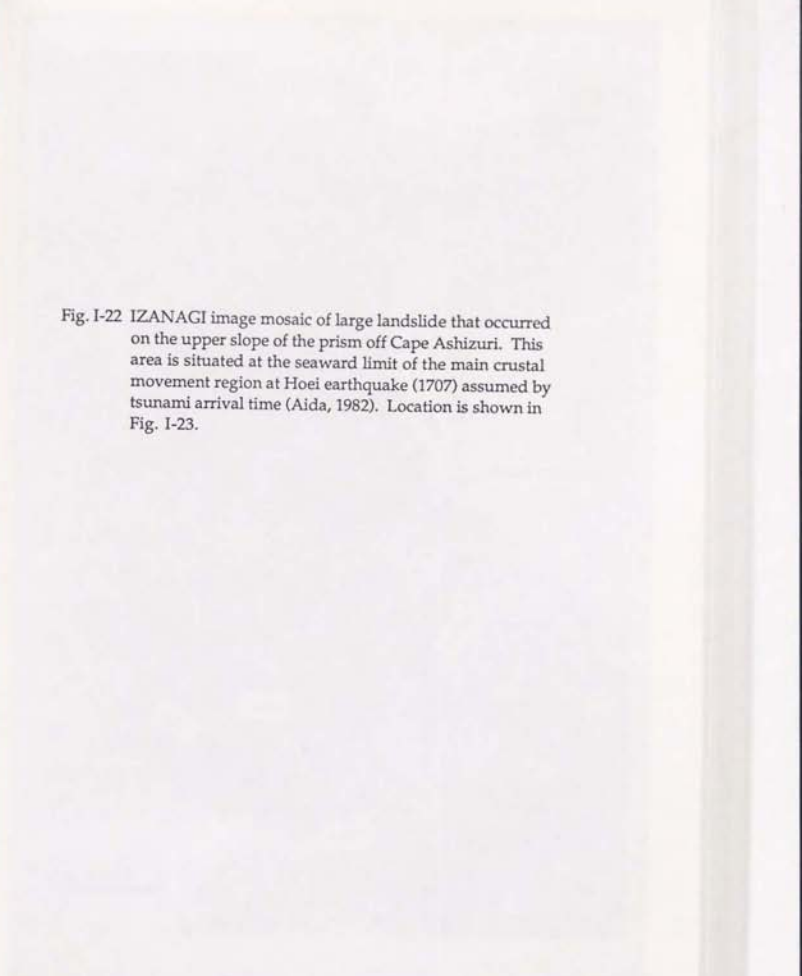
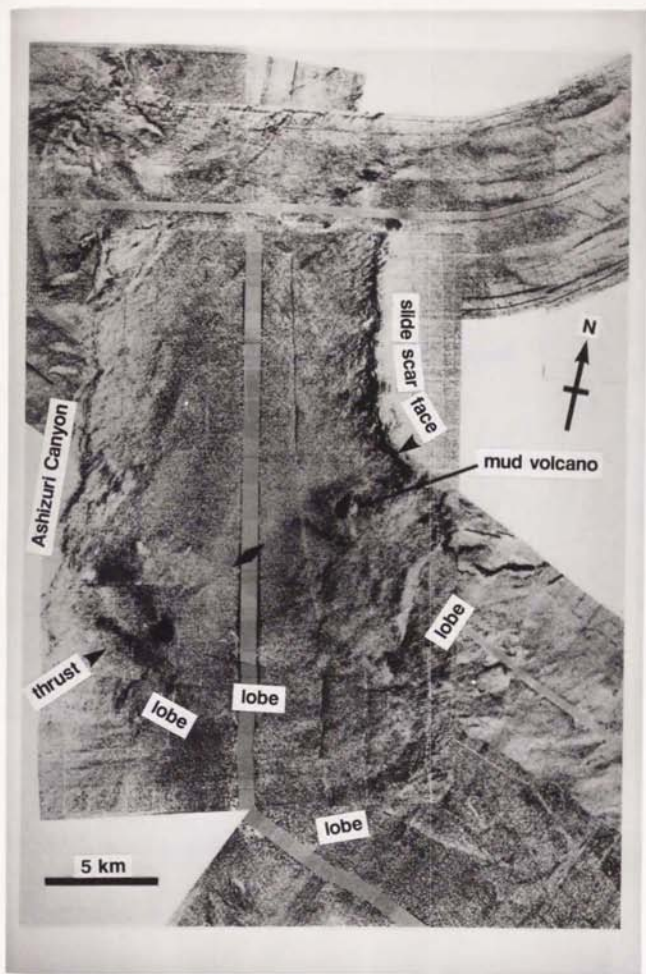


Fig. I-22 IZANAGI image mosaic of large landslide that occurred on the upper slope of the prism off Cape Ashizuri. This area is situated at the seaward limit of the main crustal movement region at Hiei earthquake (1707) assumed by tsunami arrival time (Aida, 1982). Location is shown in Fig. I-23.



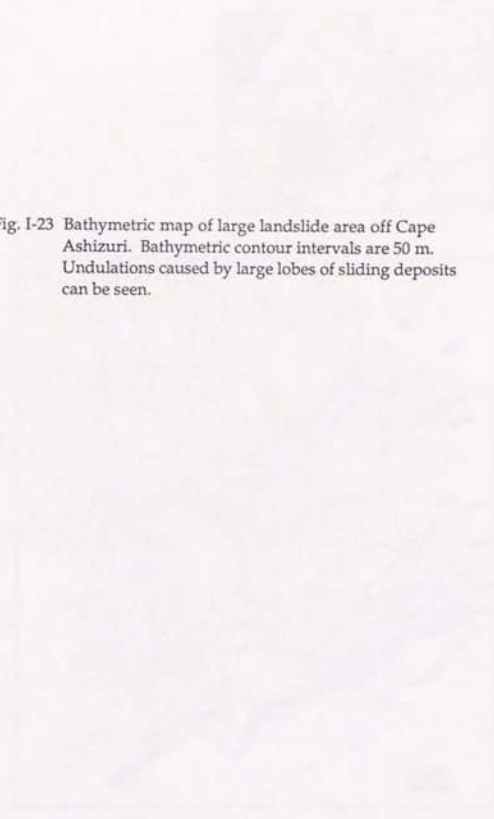
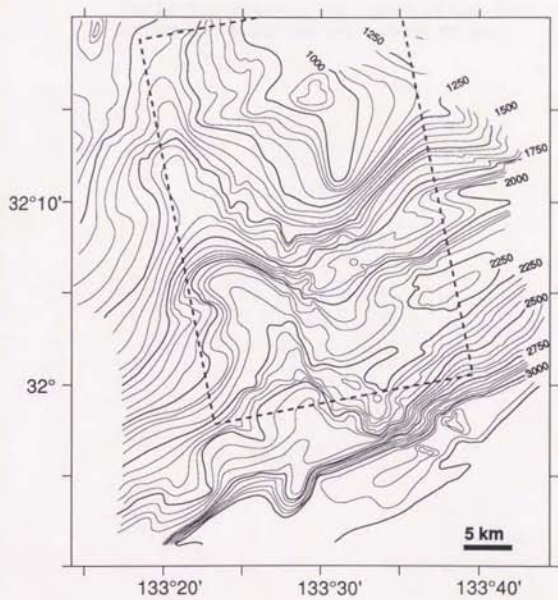
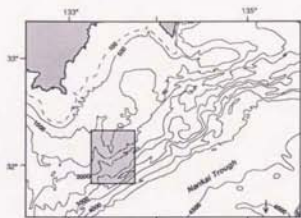


Fig. I-23 Bathymetric map of large landslide area off Cape Ashizuri. Bathymetric contour intervals are 50 m. Undulations caused by large lobes of sliding deposits can be seen.



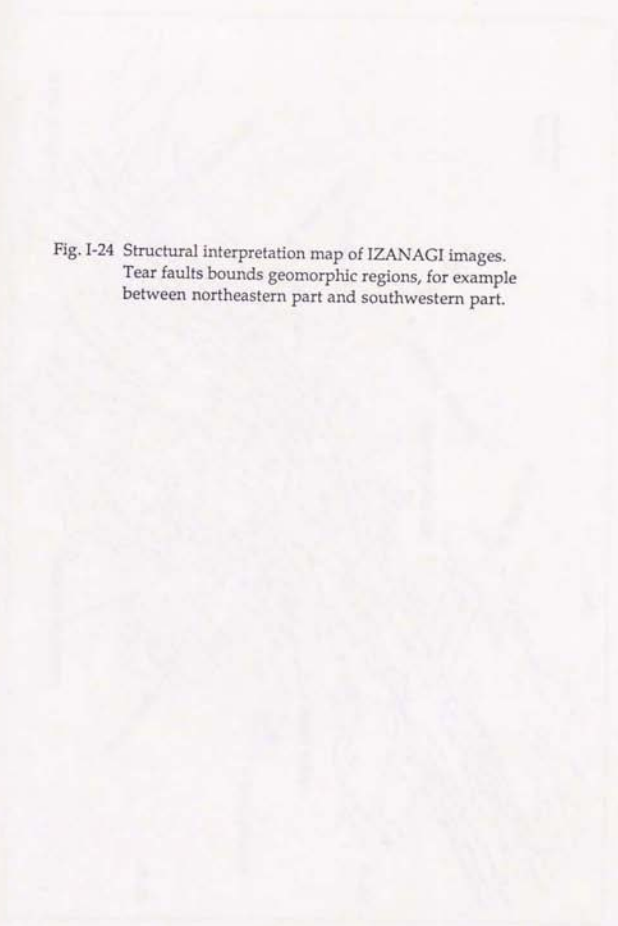
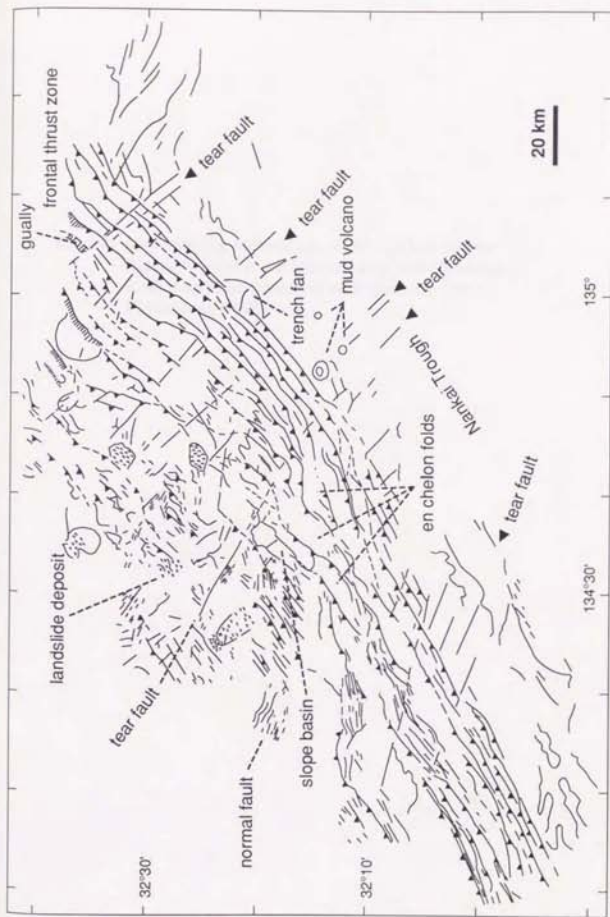


Fig. I-24 Structural interpretation map of IZANAGI images.
Tear faults bounds geomorphic regions, for example
between northeastern part and southwestern part.



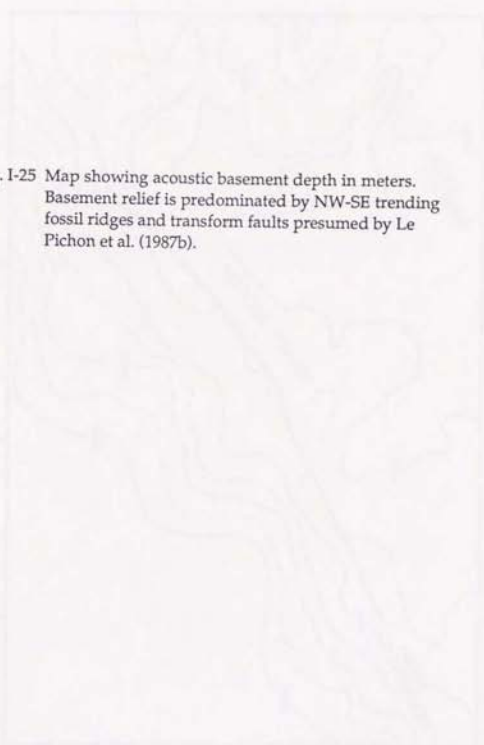
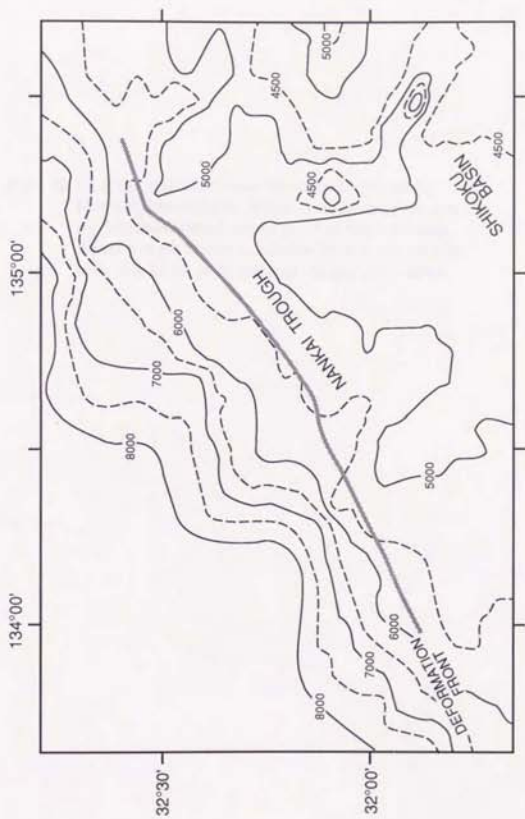


Fig. I-25 Map showing acoustic basement depth in meters. Basement relief is predominated by NW-SE trending fossil ridges and transform faults presumed by Le Pichon et al. (1987b).



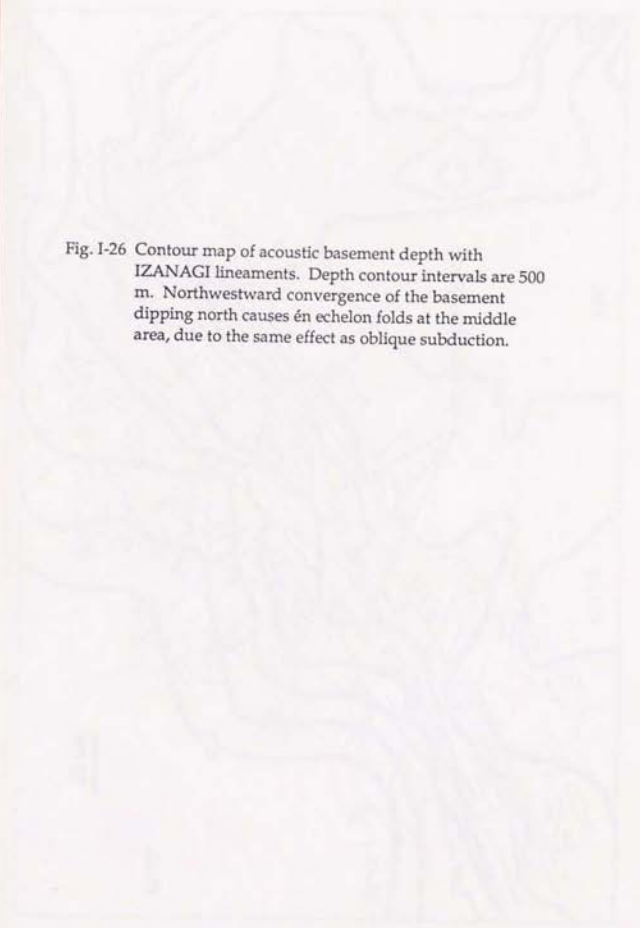
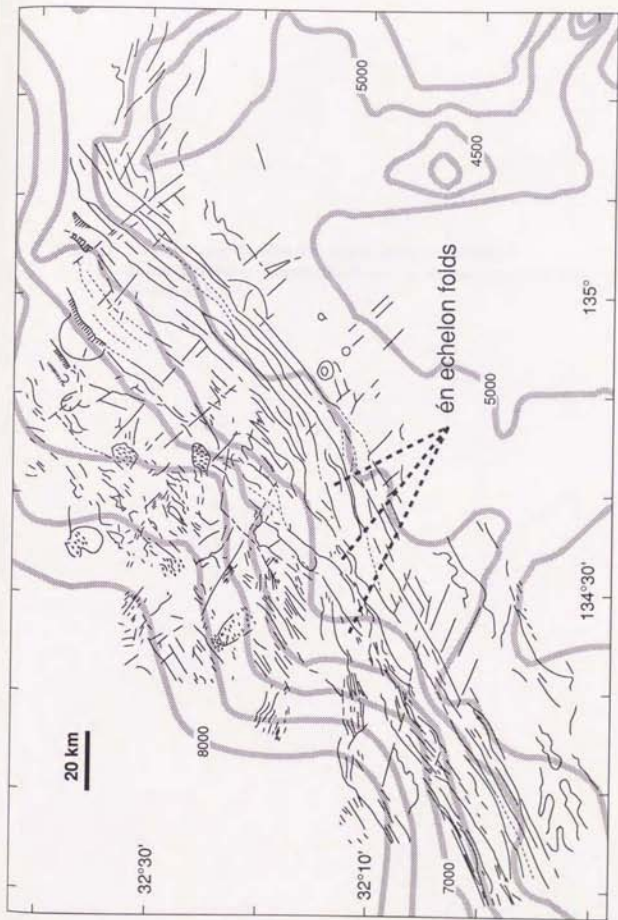


Fig. I-26 Contour map of acoustic basement depth with IZANAGI lineaments. Depth contour intervals are 500 m. Northwestward convergence of the basement dipping north causes *en echelon* folds at the middle area, due to the same effect as oblique subduction.



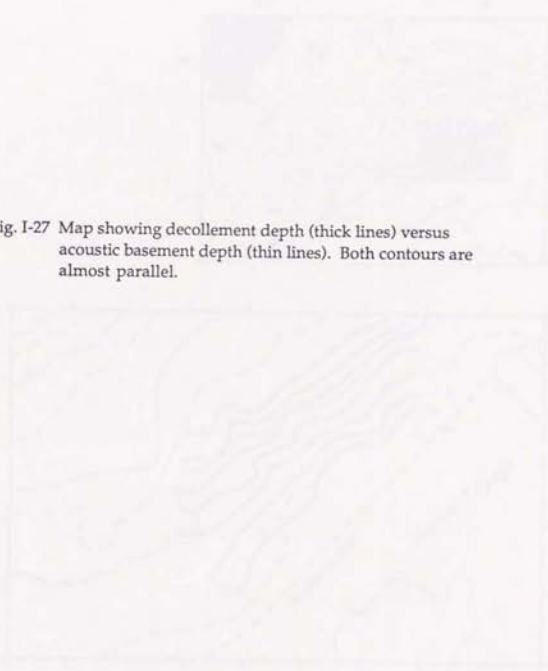
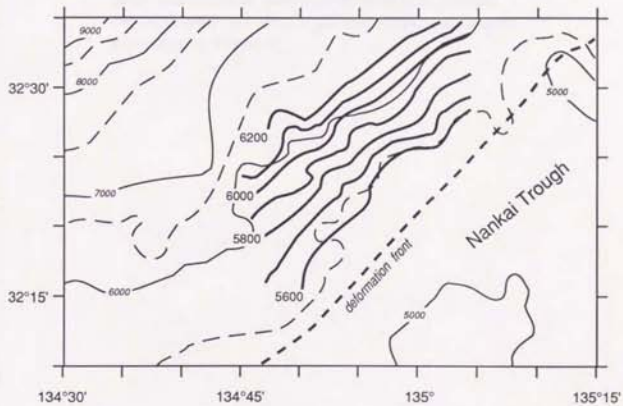
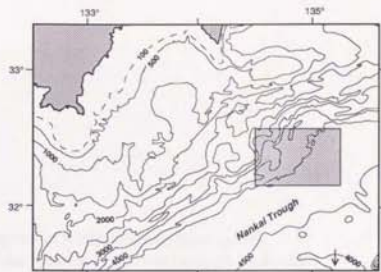


Fig. I-27 Map showing decollement depth (thick lines) versus acoustic basement depth (thin lines). Both contours are almost parallel.



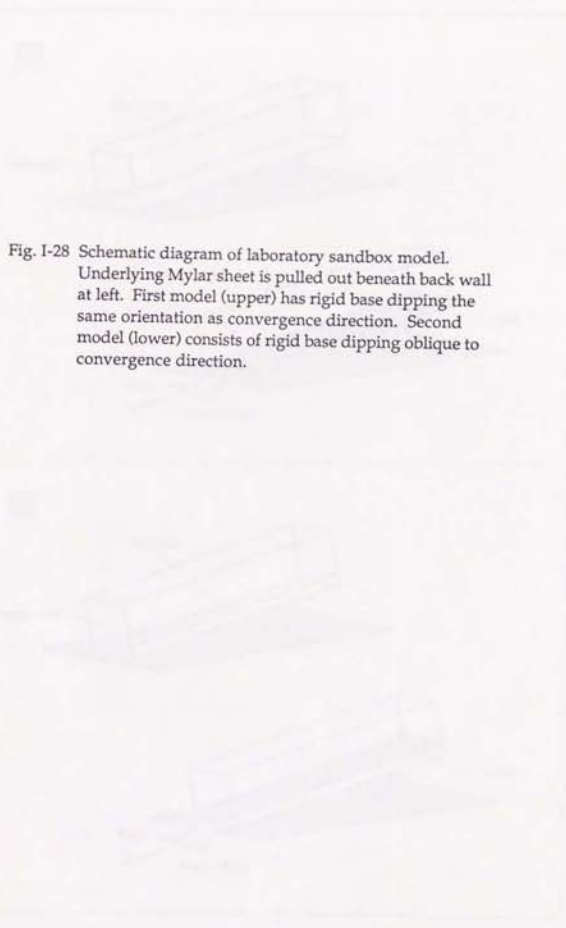
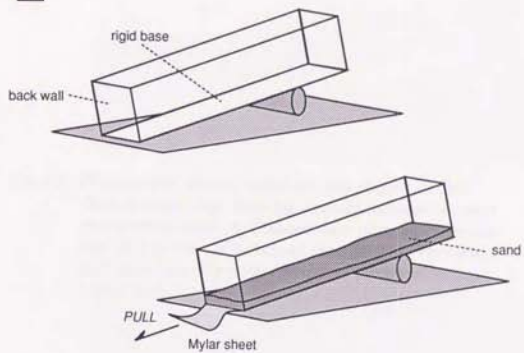
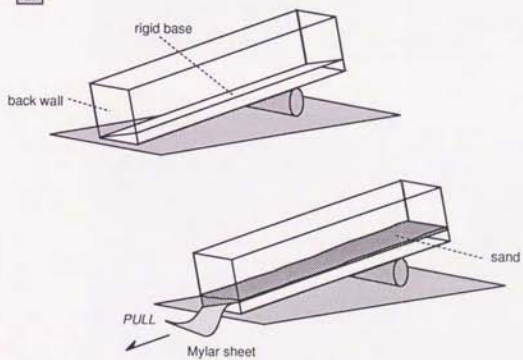


Fig. I-28 Schematic diagram of laboratory sandbox model. Underlying Mylar sheet is pulled out beneath back wall at left. First model (upper) has rigid base dipping the same orientation as convergence direction. Second model (lower) consists of rigid base dipping oblique to convergence direction.

1



2



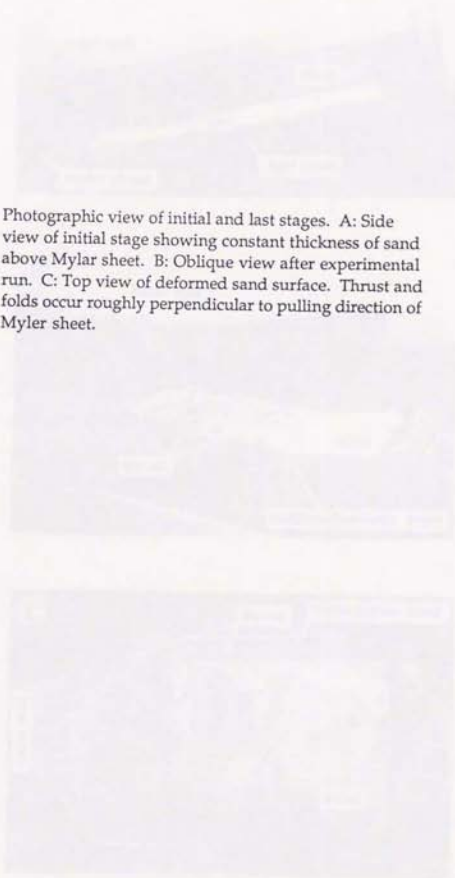
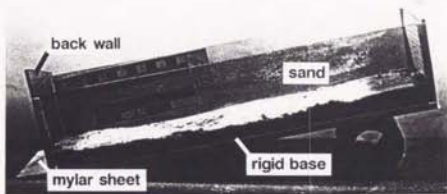
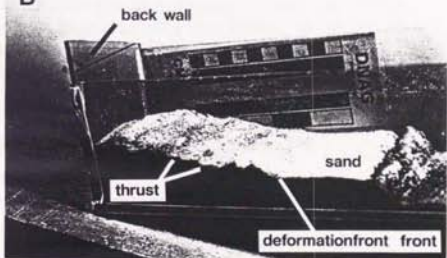


Fig. I-29 Photographic view of initial and last stages. A: Side view of initial stage showing constant thickness of sand above Mylar sheet. B: Oblique view after experimental run. C: Top view of deformed sand surface. Thrust and folds occur roughly perpendicular to pulling direction of Mylar sheet.

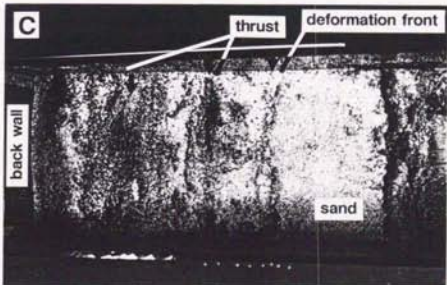
A



B



C



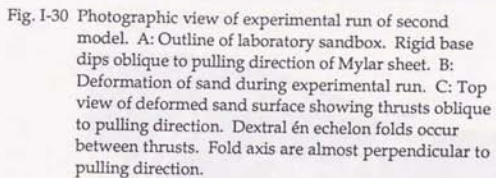


Fig. I-30 Photographic view of experimental run of second model. A: Outline of laboratory sandbox. Rigid base dips oblique to pulling direction of Mylar sheet. B: Deformation of sand during experimental run. C: Top view of deformed sand surface showing thrusts oblique to pulling direction. Dextral en echelon folds occur between thrusts. Fold axes are almost perpendicular to pulling direction.

A

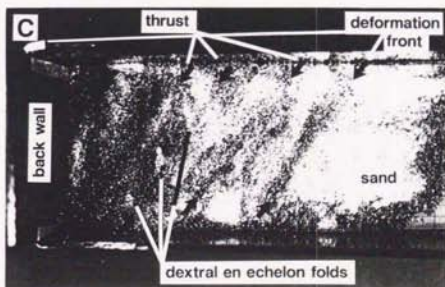
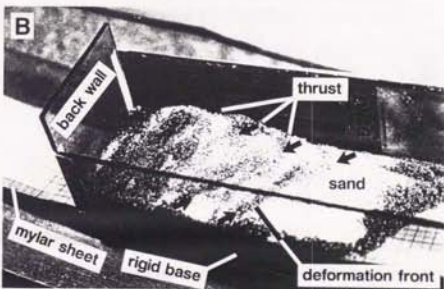
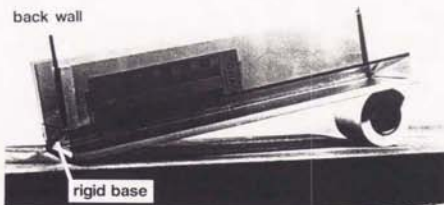


Fig. I-31 Geometry of Coulomb fracture stepping up from the decollement (after Dahlen et al., 1984). Effective stress is shown schematically by the shaded area on the right.

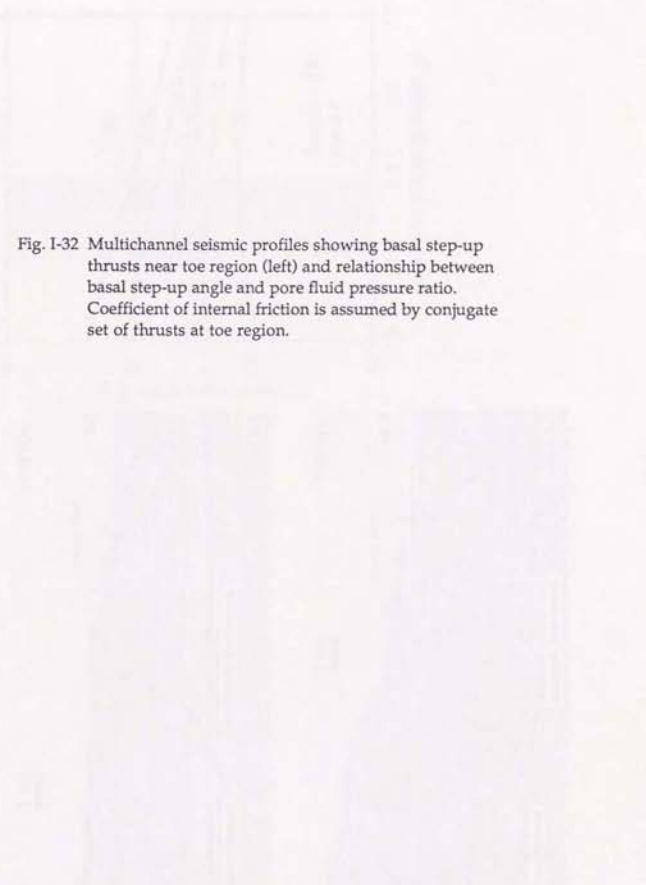
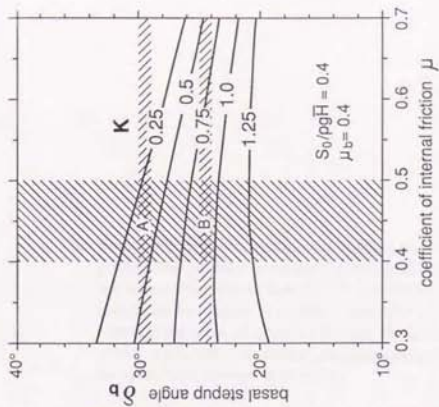
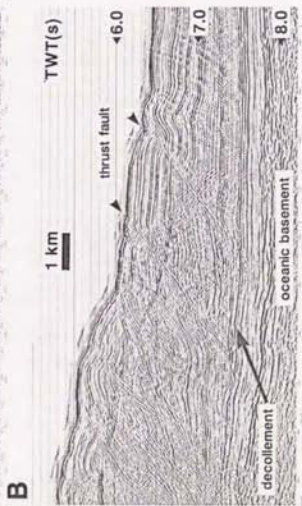
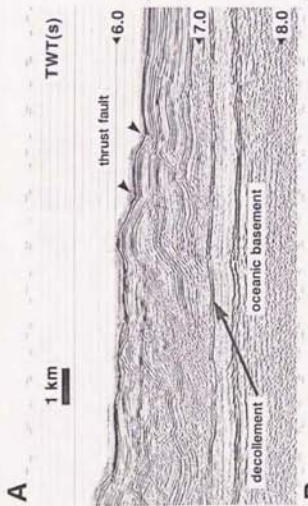


Fig. I-32 Multichannel seismic profiles showing basal step-up thrusts near toe region (left) and relationship between basal step-up angle and pore fluid pressure ratio. Coefficient of internal friction is assumed by conjugate set of thrusts at toe region.



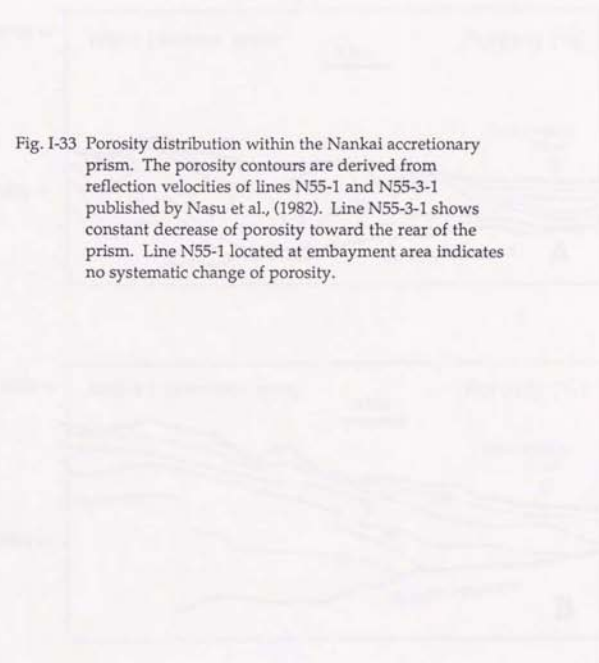


Fig. I-33 Porosity distribution within the Nankai accretionary prism. The porosity contours are derived from reflection velocities of lines N55-1 and N55-3-1 published by Nasu et al., (1982). Line N55-3-1 shows constant decrease of porosity toward the rear of the prism. Line N55-1 located at embayment area indicates no systematic change of porosity.

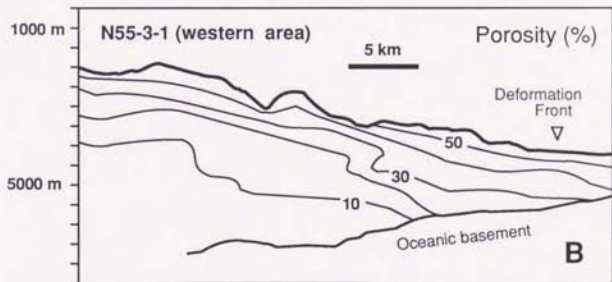
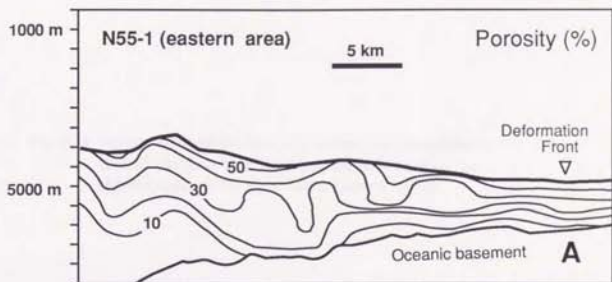
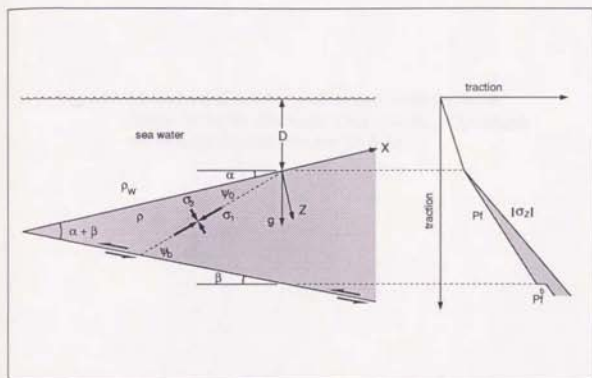


Fig. I-34 Schematic cross-section of a submarine noncohesive critical wedge with effective stress indicated by the shaded area on the right (after Dahlen, 1984).



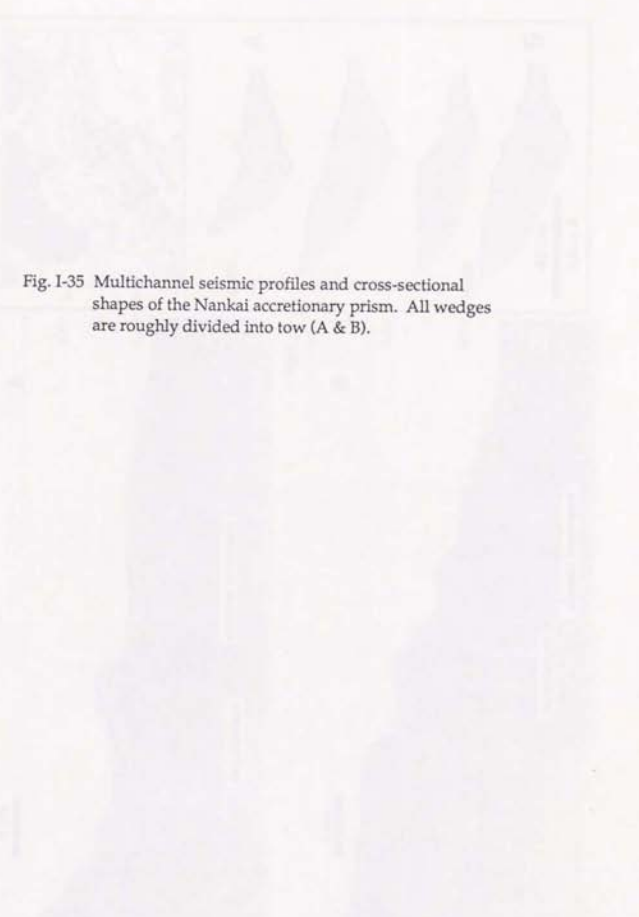


Fig. I-35 Multichannel seismic profiles and cross-sectional shapes of the Nankai accretionary prism. All wedges are roughly divided into tow (A & B).

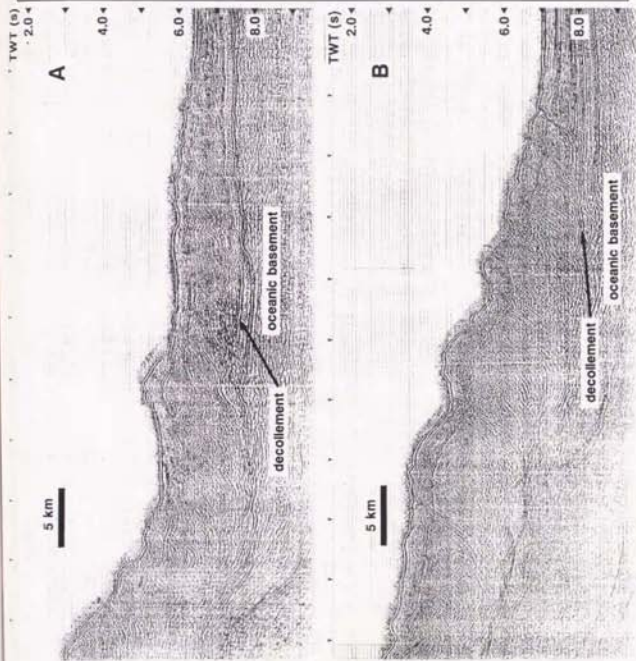
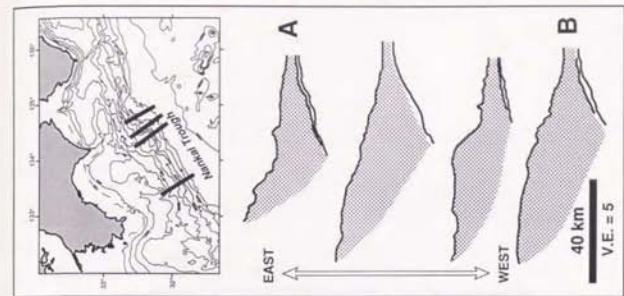
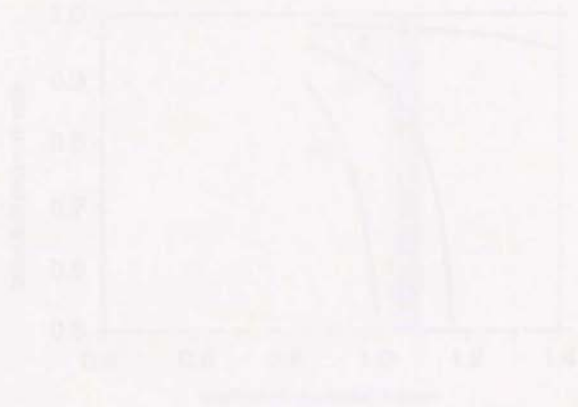


Fig. I-36 Relationship between fluid pressure ratio and coefficient of internal friction. Smaller tapered wedge indicates higher fluid pressure ratio.



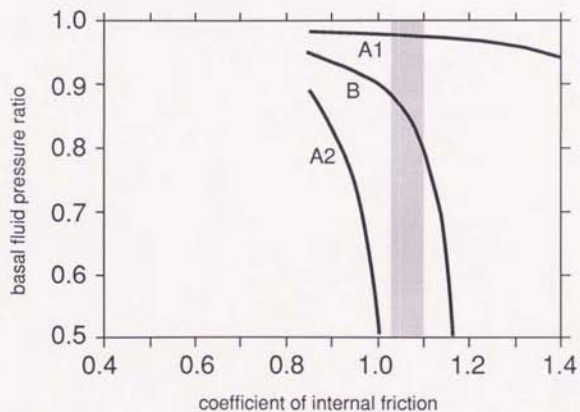
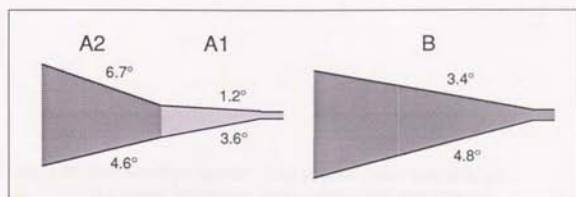
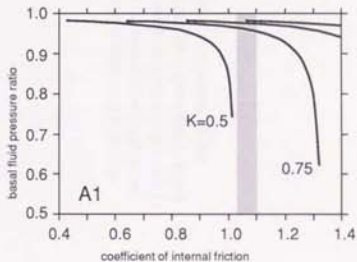
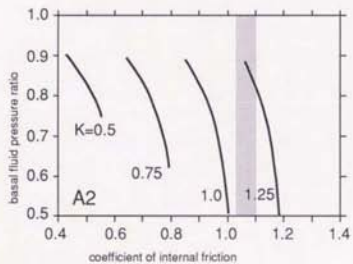
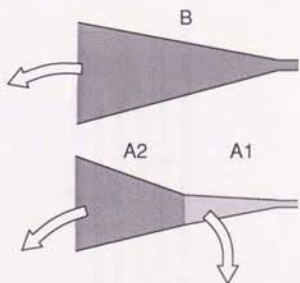
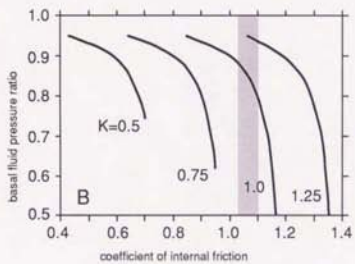


Fig. I-37 Relationships between fluid pressure ratio and efficient of internal friction for various ratios between internal and basal fluid pressure.



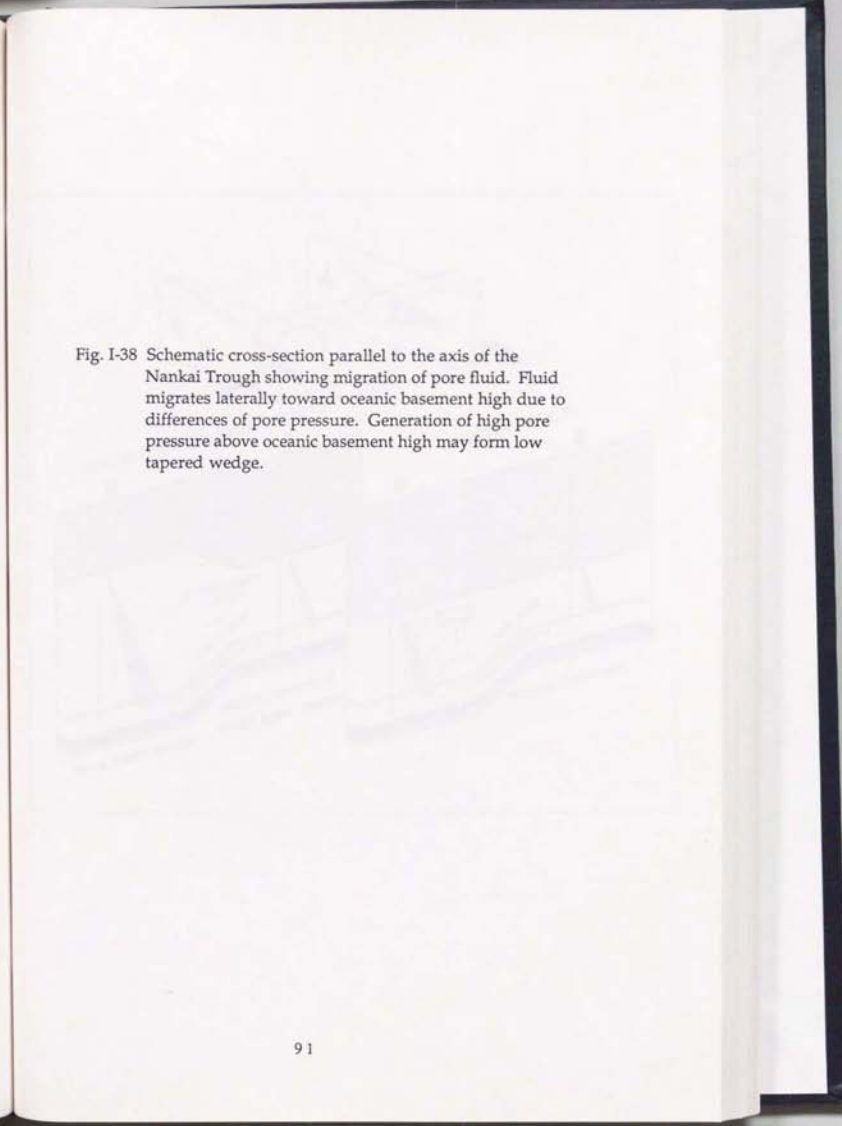
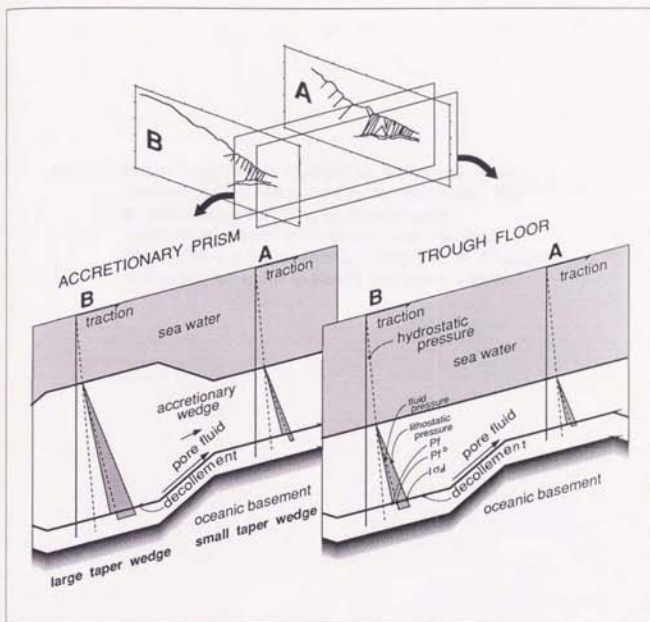


Fig. I-38 Schematic cross-section parallel to the axis of the Nankai Trough showing migration of pore fluid. Fluid migrates laterally toward oceanic basement high due to differences of pore pressure. Generation of high pore pressure above oceanic basement high may form low tapered wedge.



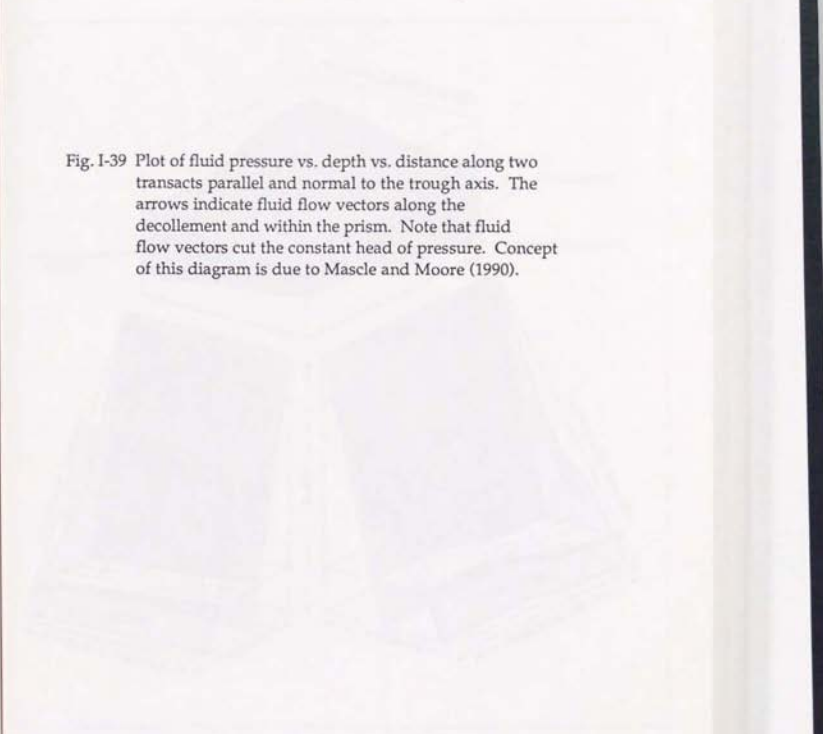
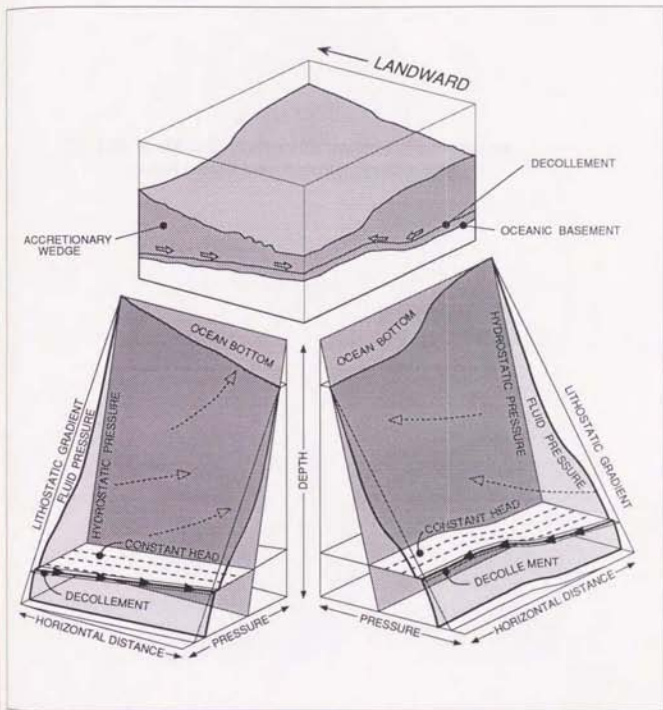


Fig. I-39 Plot of fluid pressure vs. depth vs. distance along two transects parallel and normal to the trough axis. The arrows indicate fluid flow vectors along the decollement and within the prism. Note that fluid flow vectors cut the constant head of pressure. Concept of this diagram is due to Mascle and Moore (1990).



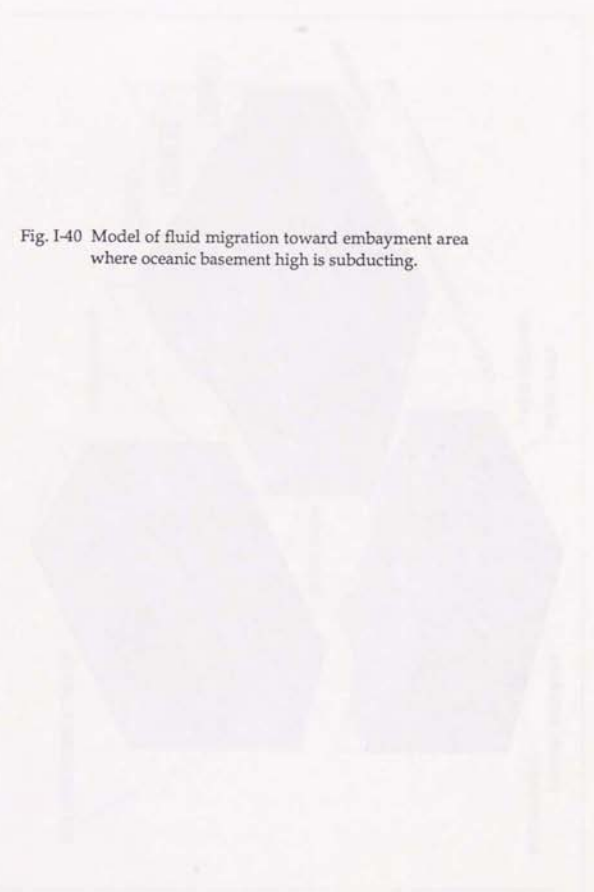
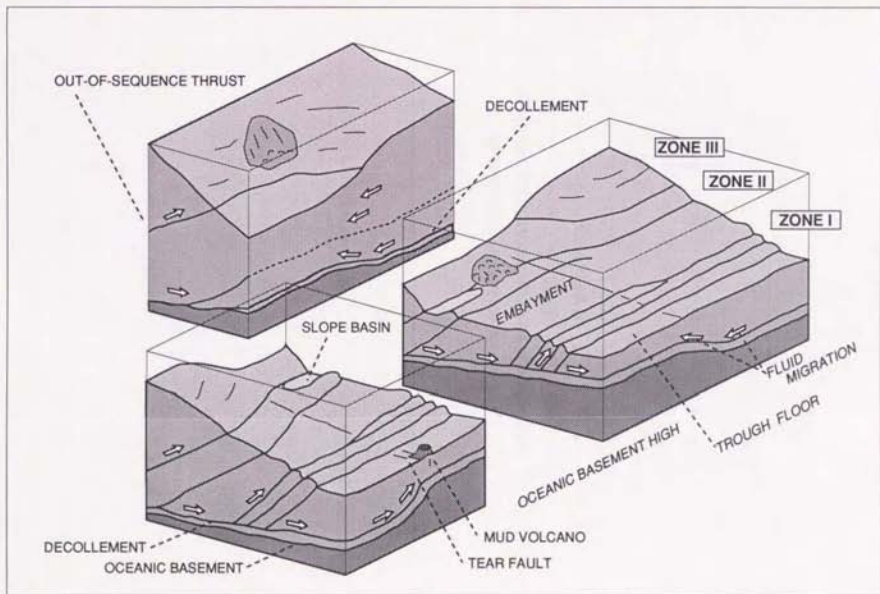


Fig. I-40 Model of fluid migration toward embayment area
where oceanic basement high is subducting.



CHAPTER II

THERMAL STRUCTURE AND HYDROGEOLOGY OF THE NANKAI ACCRETIONARY PRISM

ABSTRACT

Seismic reflection profiles obtained from the Nankai accretionary prism provide high resolution images of not only internal structures but also thermal structures, which can be estimated from the depth of bottom simulating reflector (BSR) originated in gas hydrate. More than forty seismic lines reveal that the landward decrease of heat flow observed in the Nankai accretionary prism is closely associated with the thickening of the sedimentary section above the oceanic basement. The temperature of the oceanic basement top, which is calculated by the thermal gradients and the estimated conductivities, is constant (100° - 150°) for a 30 km-wide zone beneath the seaward part of the prism. Elevated heat flow is detected at a 10 km-wide zone landward of the deformation front. This is explained by advective heat flow rather than the regional high temperature on the top of the oceanic basement. The IZANAGI side-looking sonar data indicate that the advective zone is apparently correlated with the region of rugged topography, where fault-bend anticlinal ridges are well developed without slope sediment cover. The advective heat flow thus appears to be caused by the localized fluid expulsion related to the specific structural conditions at the toe region. The frontal part of the prism is characterized by rapid tectonic overburden elevating the pore pressure and accelerating the dewatering. The existence of mud volcanoes on the trough floor suggests that a part of pore fluids expelled from the prism migrates laterally toward the trough sedimentary section. The landward-tilted and relatively undisturbed terrigenous sequences at the toe should provide effective conduits at the toe region. Fluid flow along landward dipping thrust faults is also detected by the absence of BSR at the fault plane, but have no effect on the thermal structure as a whole, because BSR do not bend up near the fault plane. Consequently, the advective heat flow may be

accomplished by the presence of coherent permeable layers rather than fault planes.

II-1. INTRODUCTION

Accretionary prisms are formed by accretion and underplating of sedimentary sequences on the subducting oceanic basement. Offscraped sediments, which initially show porosities of at least 50%, become dewatered losing the porosity and are gradually lithified through the evolution of prism. Dewatering at the frontal part of the prism are mainly caused by rapid tectonic thickening due to imbricate thrusting. In deeper parts of the prism, dewatering and volume reduction appear to proceed by dehydration and metamorphic reactions. On the other hand, underthrust sediments subduct beneath the prism separated by a decollement, maintaining considerable amount of pore fluids (Moore, 1989). Underplating of these sediments also provides pore fluids to the bottom of the prism. In addition, some fluid sources other than accreted sediments are presumed, for example, continental crust, oceanic basement, mantle wedge and meteoric water (e.g. Elderfield et al., 1990), although these quantities are likely to be very small except unknown amount in oceanic crust.

A large amount of pore fluids entering with the sediments should be expelled through the prisms as they grow. The major conduits are roughly divided into three paths. First, sedimentary layers composed of coarse grained materials have generally high permeability. In an accretionary prism, the presence of tilted permeable layers seems to play an important role in fluid flow. Based on the study of the amplitude of seismic reflectors, fluids appear to move up through the entire pelagic section from deeper levels of the prism (Moore, G.F. et al., 1990). Second, accretionary prisms are usually characterized by numerous landward dipping thrusts and some backthrusts. Fluid flow may selectively occur along such fault planes, because they probably form intensely fracture zone which may have high permeability. Submersible

observations have revealed that the distribution of active fluid vents tend to be controlled by the locations of faults (e.g. Moore, J. C. et al., 1990). Third, mud diapirs incorporated with pore fluids are remarkable as a tubular conduit, whereas the former two paths are plane in shape. Mud volcanoes which are considered to be surface manifestation of mud diapirs occasionally provide a great quantity of fluids to the seafloor (Le Pichon et al., 1990).

The mode, rate and pathway of fluid expulsion are closely related to the evolution of the accretionary prism, because physical property, chemistry and thermal structure in the prism are strongly influenced by the pore fluid (Langseth and Moore, 1990). Conversely speaking, it may be possible to reveal the role of fluids in subduction zones by the observations of relatively shallow part of the prism. This paper describes the relationship between the heat flow distribution and the geologic structure around the Nankai Trough off Shikoku. The former is mainly based on the gas hydrate distribution detected in seismic reflection profiles, and the latter is revealed by the IZANAGI side-looking sonar and seismic reflection surveys. The goal of this paper is to assess the pattern of fluid migration during the accretionary processes.

II-2. TECTONIC SETTING AND PREVIOUS WORKS

The Nankai Trough is the convergent plate boundary between the Philippine Sea and Eurasian plates (Fig. II-1). Estimates of the convergence rate vary from 1 - 2 cm/yr (Ranken et al., 1984) to 3 - 4 cm/yr (Seno, 1977). The age of the subducting oceanic crust corresponds to the age of the Shikoku Basin between 14 - 25 Ma B.P. being estimated by the magnetic anomalies (Kobayashi and Nakada, 1978; Shih, 1980). The Kinan Seamount Chain is situated in the axial zone of the Shikoku Basin. These NNW-SSE trending seamounts are interpreted to be the product of an aborted specific stage of seafloor spreading (Chamot-Rooke et al., 1987) with modification by widely distributed off-ridge volcanism (Klein and Kobayashi, 1980). An accretionary prism is well developed landward of the Nankai Trough, especially off Shikoku. The internal structure of the prism, which is mainly characterized by landward dipping imbricate thrusts, has been revealed by the seismic reflection studies (Nasu et al., 1982; Aoki et al., 1983; Moore et al., 1990).

Heat flow in the Nankai Trough is conspicuously high compared with other subduction zones (Yoshii and Kobayashi, 1981). Fair amount of data obtained by thermal probe provides the general pattern of heat flow around the Nankai Trough off Shikoku (Uyeda, 1972; Watanabe et al., 1977; Yoshii, 1979). In addition to the conventional method of heat flow measurement, Yamano et al. (1982) estimated heat flow from the gas hydrate distribution detected by seismic reflection survey. The heat flow contour map compiled by Yamano et al. (1984) shows that the highest heat flow occurs on the trough floor. On the outside of the trough, heat flow gradually decreases landward in the prism and is highly scattered on the Shikoku Basin. The heat flow value obtained in the toe is in good agreement with bottom-hole temperature at Site 583 (Kinoshita and Yamano, 1986). Some specific causes of the high heat flow on the trough

have been proposed by several authors as follows. First, the high heat flow on the trough floor is attributed to subduction of a young hot plate (Yamano et al., 1984). Second, heat flow disturbance is caused by migration of pore fluid extruded from the sediments during underthrusting (Yamano et al., 1984). Third, chemical reactions in the sediments affect surrounding thermal structures (Kinoshita and Yamano, 1986). Forth, heat rebound accompanied by buried hydrothermal circulation provides the recovery of the high heat flow on the trough (Nagihara et al., 1989). In contrary, the highly scattered values of heat flow on the Shikoku Basin are interpreted to be due to fluid circulations within the sediment. More detail heat flow survey, however, should be done to reveal the thermal structure of the Shikoku Basin. This study mainly discusses the heat flow pattern of the prism and speculates the high heat flow on the trough in the latter section.

II-3. HEAT FLOW ESTIMATION

Anomalous acoustic reflectors are found on most seismic profiles obtained from the Nankai accretionary prism (Fig. II-2). They are generally subparallel to the sea floor and often cut across the reflectors of sedimentary layers. Such bottom simulating reflectors (BSR) are regarded as the phase boundary between solid gas hydrates and gas soluble fluid in sediments (Yamano et al, 1982). Gas hydrate compounds have an ice-like crystalline structure in which a large amount of gas molecules are trapped by the water molecule lattice. Free gas can be trapped beneath the hydrate layer which forms a barrier to upward migrating fluids and gases. Based on the experimental study, artificially formed gas hydrate in the sediment causes marked increase in acoustic wave velocity (Stoll et al., 1971). Moreover, a concentration of gas below the hydrate, if present, causes the velocity and density to decrease considerably at the boundary (Bryan, 1974). Consequently, BSR is thought to represent an reversed polarity which indicates a decrease of acoustic impedance from gas hydrate to fluid phase in the sedimentary sequence.

The phase diagram of hydrate with various gas composition shows that the hydrate stability field is situated in lower temperature and higher pressure (e.g. Tucholke et al., 1977). Therefore, the depth distribution of gas hydrate layer provides the insitu temperature at the BSR. The thermal gradients were estimated in some areas on the basis of hydrate-forming conditions (Shiple et al., 1979; Yamano et al., 1982).

The method of heat flow estimation is proposed by Yamano et al. (1982) as shown in Fig. II-3. Seismic reflection profiles exhibit the depth of BSR in two-way travel time. Conversion of travel time into the depth in meter is based on average velocity law (Fig. A5) constructed by the published interval velocity data (Nasu et al., 1982) and the correlation

between seismic reflection profiles and drilling results (e.g. Moore et al., 1990; Taira, Hill, Firth, et al., in press). The pressure at the BSR is calculated by the overburden of both the sediment and the sea water columns. The average sediment density is assumed to be 1.9 g/cm^3 from drilling results (Bray and Karig, 1986; Taira, Hill, Firth, et al., in press). The temperature at the BSR can be found by the phase diagram and the pressure data, when the gas compositions are fixed. Gas extracted from continental margin sediments is composed of methane and small gas mixtures such as ethane and CO_2 . The drilling data of ODP Leg 131 shows the absence of ethane gas in the sediment above 700 m (Taira, Hill, Firth, et al., in press). In this study, the boundary condition for a pure water and pure methane system can be adopted, because small addition of NaCl reduces the effect of CO_2 gas mixture (Kvenvolden and Barnard, 1983). The mean geothermal gradient can be estimated by the discrepancy between the temperatures at the BSR and the sea floor, versus the depth of the BSR. The sea floor temperature considers to the bottom water temperature obtained by CTD (Ocean Research Institute, unpublished data).

The acquisition of heat flow value needs the estimation of the thermal conductivity as well as the geothermal gradient. According to Horai (1982), there are remarkable correlations between thermal conductivity and other physical properties such as compressional wave velocity (V_p). Therefore, the mean thermal conductivity above BSR can be estimated to be $1.3 \text{ mW/m}^\circ\text{C}$ by appropriate V_p values derived from seismic reflection studies (e.g. Nasu et al., 1982). This estimated value is in good agreement with physical property data obtained by deep-sea drillings (Karig et al., 1975; Kinoshita and Yamano, 1986; Taira, Hill, Firth, et al., in press).

Seismic profiles for the mapping of both the sea floor and the BSR depths are JAPEX, ORI and Fred Moore multichannel lines and Kaiko project single-channel lines (Fig. II-4). The contour map of heat flow

distribution is constructed by more than four thousand data points on forty seven seismic reflection lines (Fig. II-5). Yamano et al.(1982) argued that the error attains 25 % of the absolute values, and suggested that the main cause of error is derived from the estimation of thermal conductivity and velocity structure. However, the error about the Vp value assumes to be relatively small except for well-lithified sediments exposed at steep slope areas. Because the velocity estimation is restricted within the shallow part of the prism and there is no BSR in most slope basins and the frontal part of the prism where large velocity changes are predicted. Calculated heat flow values in this study are shown in Fig. A6.

II-4. HEAT FLOW DISTRIBUTION

The heat flow obtained in this study show almost the same general distribution as the previous heat flow data (Yamano et al., 1984; Yamano et al., 1986; Kinoshita and Kasumi, 1988). Fig. II-5 demonstrates that the heat flow increases toward the trough floor as pointed out by Yamano et al. (1982). In addition, a large quantity of heat flow data obtained in this study reveals the more detail distribution than that of previous ones. The heat flow contour indicates the conspicuously high heat flow in the topographically low region named "Tosa Bae embayment" by Leggett et al. (1984).

The cross sectional pattern of heat flow have been discussed on the basis of two dimensional models (Yamano et al., 1984; Kinoshita and Kasumi, 1988; Nagihara et al., 1989). Kinoshita and Kasumi (1988) explained the landward decreasing heat flow by the cooling effect of the subducting plate and the landward thickening effect of the accretionary prism. The same results were obtained by heat flow observations in other areas (Langseth et al., 1990; Davis et al., 1990). Based on these results, the heat flow value is expected to be related to the thickness of the prism. Seismic reflection profiles show that the prism in the Tosa Bae embayment is much smaller tapered than the surrounding area (Fig. II-6). This is in good agreement with the observation of high heat flow.

The sediment thickness (prism thickness) above the oceanic basement (Fig. II-7) is estimated by seismic reflection profiles and the average velocity law. Total sixty seven seismic profiles are available for the mapping of the sediment thickness. The contour map of sediment thickness is characterized by undulation with NW-SE trending axis, which is the same orientation as the presumed fossils ridges during the spreading of the Shikoku Basin (Chamot-Rooke et al., 1987). Le Pichon et al. (1987b) attributed the distribution of trench-fill thickness to the relief of

the oceanic basement. Moreover, the thickness variations in the prism is enlarged by the NW directed convergence, because thickening of the prism seems to be mainly due to the amount of incoming sediments. For instance, the small tapered accretionary prism is developed in the Tosa Bae embayment where the oceanic basement high has been subducted.

A combined contour map of both the heat flow and the sediment thickness is shown in Fig. II-8. There is a good correlation between heat flow and sediment thickness, especially 3000 m contour in thickness versus 70 mWm² contour in heat flow. This relation suggests that the heat flow observed near the surface of the prism is closely controlled by the depth and the thermal structure of the oceanic basement. Fig. II-9 illustrates the almost linear relationship between heat flow and sediment thickness along the cross section at the Tosa Bae embayment. This relationship seems to extend from the toe to the area where the sediment thickness exceeds 5000 m.

II-5. DISTRIBUTIONS OF BSR

The existence of gas hydrate is not always accompanied with BSR. In the Middle American trench off Guatemala, the drilling results provide the abundant evidence for the presence of gas hydrate in the recovered samples where BSRs are not readily discernible by the seismic reflection profile (Harrison and Curiale, 1982). This observation suggests that the accumulation of gases is indispensable for the formation of BSR. The gases are derived mainly from organic-rich materials such as terrigenous sediments.

Distribution of BSR around the Nankai Trough is restricted to the accretionary prism except for the frontal part (Fig. II-6). In addition, there is occasionally no BSR at the slope basin and along the fault plane (Fig. II-2). The lack of BSR in the slope basin seems to result from the inactive fluid migration owing to the subhorizontal strata. Moreover, the slope basin sediments contain less organic matter than the offscraped sediments. In the case of the Nankai trough, a large quantity of terrigenous sediments are supplied along the trough axis by turbidity currents. However, the trough fills are accreted before the sufficient generation of gases. On the other hand, the broad and thick terrigenous sediments provides the seismic bright spot due to accumulation of gases in the Makuran abyssal plain (Minshull and White, 1989). The cause of no BSR in the frontal part of the prism is thought to be the insufficient gas generation within the sediment as well as in the trough floor, although the tilted layers suitable for fluid migration are already developed.

The disappearance of BSR along thrust fault may be influenced by the upward migration of pore fluids. No depth change of BSR across the fault plane indicates that the thermal effect of assumed fluid flow appears to be restricted in the small region near the thrust fault. In the Makran accretionary prism, however, Minshull and White (1989)

reported about the shallowing BSR near the thrust fault and suggested warm pore fluids expelled from the depth. This feature indicates that the major conduits are fault planes having higher permeability than the host sedimentary layers.

II-6. EFFECTS OF FLUID MIGRATION

The comparison between the observed heat flow and the model of conductive thermal structure is one of the methods to determine whether the prism is conductive or not. As mentioned previously, Kinoshita and Kasumi (1988) proposed the two dimensional steady state model only based on conductive heat flow. They calculated the heat flow variation from the trough to the prism using of the basal heat flux treated as a parameter. Fig. II-10 shows the comparison between the model curves of surface heat flow and the observations of heat flow in this study. The 110 mW/m^2 curve and the 150 mW/m^2 curve represent the surface heat flow variations calculated by the basal heat fluxes on the basis of the estimated age of the Shikoku Basin and the mean heat flow observed on the trough floor, respectively. The observations in the landward slope of the prism is roughly consistent with the 110 mW/m^2 curve. Toward the trough floor, the observations gradually approaches to the 150 mW/m^2 curve. Based on the Kinoshita and Kasumi's (1988) model compared with the results of this study, the frontal part of the prism is not regarded as conductive but advective.

The possibility of fluid expulsion in the toe of the prism is indirectly supported by the presence of a single shell of *Calyptogenia* observed by the deep-towed camera during the KH86-5 cruise (Taira et al., 1988). Kinoshita and Kasumi (1988) obtained abnormal high heat flow just at the deformation front by means of the ordinary heat flow probe, and presumed fluid upwelling through a thrust fault. The cross sections of thermal structure, which are the same lines as the seismic reflection lines N55-1 and N55-3-1, provides the more obvious effects for fluid migration (Fig. II-11). These profiles are constructed by estimating of thermal gradients from the surface to the deeper part of the prism, which is calculated by the conductivities and the heat flow values from BSR. The

conductivity can be estimated by the previously provided V_p values (Nasu et al., 1982) adopting the Horai's (1982) V_p -conductivity relation. Fig. II-11 demonstrates that the surface temperature of the oceanic basement is relatively constant between 100 °C and 150 °C at the both sections. In the eastern area (Line N55-1), however, the thermal gradient increases at the frontal part of the prism, and the geothermal contour lines cut across the top of the oceanic basement. The large thermal gradient at the toe appears to be caused by the up-dip migration of pore fluids rather than the regionally hot oceanic basement near the toe. Therefore, the 150 °C contour line is probably parallel to the top of the basement, when the active fluid flow is restricted within the sedimentary sequences.

Based on the simple treatment of the thermal effect of pore fluid advection (Bredehoeft and Papadopoulos, 1965), upward fluid velocity (V_z) can be estimated from the discrepancy between the thermal gradient obtained by heat probe or BSR (G_a) and that assumed by the conductive model (G_c) in a thermal conductivity K . The one-dimensional steady state solution is

$$v_z = \beta K / \rho_w c_w$$

where

$$\frac{G_a}{G_c} = \frac{\beta L}{(1 - e^{-\beta L})}$$

and C_w , ρ_w and L are the specific heat capacity, density of pore fluid and the total thickness of sediment where advection occurs.

Within 10 km landward of the deformation front, the average thermal gradient of 100 °C/km is estimated from heat probe and BSR. Therefore, the ratio G_a / G_c is about 1.2 because the predicted value of thermal gradient is 83 °C/km using the conductive model. Inserting $C_w = 4.2 \times 10^3$ J/kg, $\rho_w = 10^3$ kg/m³, $K = 2.0$ W/mK, $L = 1000$ m gives a vertical Darcy water velocity of 1.79×10^{-10} m/s. This value is almost the same as that in the toe of the Northern Cascadia accretionary prism estimated by Davis et al. (1990).

II-7. HEAT FLOW VARIATIONS ALONG THE NANKAI TROUGH

The observed heat flow values on the Shikoku Basin, which are scattered and vary from less than 50 mW/m^2 to 222 mW/m^2 , is mostly lower than that estimated from the magnetic-anomaly age (Yamano et al., 1984). Such low and scattered heat flows were interpreted to be due to the fluid circulation or the rapid sedimentation on the trough. The heat flow seems to be stable in the accretionary prism rather than the Nankai Trough (Fig. II-5).

Fig. II-12 shows plots of the heat flow estimated from BSR versus the distance from the NW-SE trending line of the Kinan Seamount chain for various values of the sediment thickness in the prism. The highly scattered values of heat flow detected in the thinner sedimentary sequence (less than 3000 m) may be attributed to the updip fluid flow near the deformation front (Fig. II-12A). On the contrary, the heat flow values in the thick sedimentary sequence (more than 3000 m) reveals the southwestward decreasing tendency of heat flow (Fig. II-12B). At the eastern-most part, however, very low values of heat flow are distributed. These low values appear to be caused by cooling due to the rapid sedimentation before accretion, because the very thick turbidite sequence is developed seaward of the low heat flow region. The high heat flow in the area where the Kinan Seamount chain have subducted and the southwestward decrease of heat flow values may be associated with the off-ridge volcanism activity and/or the age of the oceanic plate, although there is no observation in the area eastward of the seamount chain (Fig. II-12).

II-8. DISCUSSION

The well-defined BSR in the prism except for the toe region suggests the widespread migration of pore fluids including gases. The rate of such migration is presumed to be extremely small, because the heat flow observations are consistent with the estimated values based on the conductive model. Fig. II-11 illustrates that the thermal structure of the prism is basically conductive and mainly controlled by the temperature of the subducting oceanic basement. The fluid flows along the thrust faults, even if present, have little effect on the thermal structure as a whole, because the BSR does not bend up but disappears at the fault plane.

The observations of higher heat flow than that estimated from the conductive model are detected at the prism of the eastern area and situated within 10 km of the deformation front. Such region is assumed to be advective due to active fluid migrations. The boundary area between conductive and advective may be associated with the surface structural features. The mosaic of side-looking sonar image obtained by "IZANAGI" demonstrates that the well-continuous rugged topographic features are distributed at the frontal part of the prism (Fig. II-13). Based on the seismic reflection profiles (Fig. II-6), these configurations obviously correspond to the anticlinal ridges caused by thrust faults at intervals of a few kilometers. Toward the rear of the prism, slope sediments mainly composed of fine grained materials have overlain and modified the undulations such as fault-bend folds (Fig. II-13).

The boundary between conductive and advective, which means the change of the thermal structure in the prism, seems to coincide with the transition zone of the IZANAGI image from well-defined lineament regions to low reflective regions covered by slope sediments. At the toe, pore fluids may be easily expelled out from the prism because of no

sedimentary cap on the slope. In addition, the toe region is regarded as the most active dewatering zone due to rapid tectonic overburden during frontal accretion (Bray and Karig, 1986). Moreover, the terrigenous sediment layers are tilted without conspicuous deformations. The intensely disrupted layers landward of the toe may have low permeability as a whole, because the permeable layer is isolated and the porosity decreases landward. The amplitude of seismic reflectors at the toe suggests the fluid expulsion through the entire pelagic section (Moore G.F. et al., 1990). Therefore, the condition of advective heat flow is attained by the rapid tectonic overburden, continuously tilted permeable layers and no sedimentary cap at the toe region. On the other hand, Fig. II-11 indicates no advective zone in the western area. This may be related to the narrow regions where the IZANAGI image shows well-defined lineaments in comparison with the eastern area (Fig. II-13). Unfortunately, there is no heat flow data due to the lack of BSR at the toe of the western area, although the presumed advective zone based on the IZANAGI image may be distributed within 7 km of the deformation front (Fig. II-11). In the northern Cascadia accretionary prism, fluid expulsion resulting from the dewatering of the prism sediments is detected at the 10-20-km wide zone landward of the deformation front (Davis et al., 1990).

The pore fluids expelled from the prism seems to be mostly discharged at the toe region, but may be partly supplied into the sedimentary sequence under the trough floor. It is likely that the high pore pressure generates due to the tectonic overburden beneath the toe and migrates laterally into the relatively low pressured sediments in the trough (Fig. II-14). The IZANAGI image revealed that the three cones regarded as mud volcanoes are developed in the trough floor (Fig. II-13). The biggest one is 2 km in diameter and less than 50 m in height, and is characterized by the depression at the top. The existence of mud volcano provides evidence of very high pore pressure caused by lateral fluid

migration from the prism probably through the decollement as inferred for the Barbados Ridge (Westbrook and Moore, 1983). The mud volcanoes appear to occur along the well-developed probable tear faults under the abnormal high pore pressure (Fig. II-14). Such fluid flow within the trough sediments might be the main cause of the high heat flow observed in the trough floor. The abnormal high heat flow near the prism toe at the embayment area may also result from the lateral fluid migration from the surrounding prisms where larger tectonic overburden arise pore pressure.

II-9. SUMMARY AND CONCLUSIONS

The detailed heat flow mapping by the BSR reveals that the heat flow distribution in the prism is closely associated with the thickness of the sediments above the oceanic basement. The heat flow value decreases with the increase of sediment thickness independently of the distance from the deformation front. This relationship extends from the toe to the area where the thickness of sediment starts to exceed 5000 m.

Based on the observed heat flow values and the conductive steady state model (Kinoshita and Kasumi, 1988), the surface heat flow is controlled by conductive heat transfer except in the toe of the prism. The cross section of thermal structure, which is constructed by presumed conductivity and thermal gradient near the surface, indicates that the surface temperature of the oceanic basement is between 100° and 150° beneath the lower slope of the prism. Moreover, the toe of the eastern area is characterized by higher heat flow probably caused by pore fluid expulsion. Such high heat flow is not attributed to the localized fluid flow along the thrust as pointed out by Davis et al (1990).

The high heat flow region is obviously correlated with the well-developed fault-bend fold zone revealed by the IZANAGI side-looking sonar. The active fluid expulsion seems to be due to specific structural features at the toe region. First, rapid tectonic overburden occurs owing to frontal accretion. High pore pressure generated within and under the prism should cause diffusion of pore fluid through the permeable zones. A part of such fluid flow may extend seaward. The existence of mud volcanoes in the trough floor suggests the lateral fluid migration from the prism. Such lateral flow within the trough sediment provides a good explanation for the highly scattered heat flow values previously observed by thermal probes. Second, the existence of tilted terrigenous sequences provides the effective conduits. These conduits in the toe region are

continuous in comparison with the landward portion of the prism where the offscraped sedimentary layers are highly disrupted. Third, the slope sediments which prevent the expulsion of fluids are very thin at the toe region. Consequently, a large amount of pore fluids appear to regionally migrate up at the shallow part of the toe region.

References

- Aoki, Y., Tamano, T., and Kato, S. 1983. Detailed structure of the Nankai Trough from migrated seismic sections. *Mem. Am. Asso. Pet. Geol.* 34, 309-322.
- Bray, C.J., and Karig, D.E. 1986. Physical properties of sediments from the Nankai Trough, Deep Sea Drilling Project Leg 87A sites 582 and 583. In Kagami, H., Karig, D.E. et al., *Init. Repts. DSDP*, Washington (U.S. Govt. Printing Office), 87, 827-842.
- Bredehoeft, J., and Papadopoulos, I.S. 1965. Rates of vertical groundwater movement estimated from the Earth's thermal profile. *Water Resour. Res.*, 1, 325-328.
- Bryan, G.M. 1974. In situ indications of gas hydrates, In Kaplan, I.R., ed., *Natural gases in marine sediments*, New York, Plenum, 298-308.
- Chamot-Rooke, N., Renard, V., and Le Pichon, X. 1987. Magnetic anomalies in the Shikoku Basin: a new interpretation. *Earth Planet Sci. Lett.*, 83, 214-228.
- Davis, E.E., Hyndman, R.D., and Villingier, H. 1990. Rates of fluid expulsion across the northern Cascadia accretionary prism: Constrains from new feat flow and multichannel seismic reflection data. *J. geophys. Res.* 95, 8869-8890.
- Elderfield, H., Kastner, M. and Martin, J.B. 1990. Composition and sources of fluids in sediments of the Peru subduction zone. *J. geophys. Res.* 95, 8819-8828.
- Harrison, W.E., and Curiale, J.A. 1982. Gas Hydrates in sediments of holes 497 and 498A, Deep Sea Drilling Project Leg 67, In Aubouin, J., von Huene, R., et al., *Init. Repts. DSDP*, Washington (U.S. Govt. Printing Office), 67, 591-594.

- Horai, K. 1982. Thermal conductivity of sediments and igneous rocks recovered during Deep Sea Drilling Project Leg 60, In Hussong, D., Uyeda, S. et al., *Init. Repts. DSDP*, Washington (U.S. Govt. Printing Office), 60, 807-834.
- Karig, D.E. 1975. Basin genesis in the Philippine Sea. In Karig, D.E., Angevine, C.L. et al., *Init. Repts. DSDP*, Washington (U.S. Govt. Printing Office), 31, 857-880.
- Kinoshita, H. and Yamano, M. 1985. The heat flow anomaly in the Nankai Trough area. In Kagami, H., Karig, D.E., et al., *Init. Repts. DSDP*, Washington (U.S. Govt. Printing Office), 87, 737-743.
- Kinoshita, M., and Kasumi, Y. 1988. Heat flow measurement in the Nankai Trough Area. *Preliminary Report of the Hakuho Maru cruise KH86-5: ODP Site Survey*. Ocean Research Institute, University of Tokyo, 190-206.
- Klein, G. deV., and Kobayashi, K. 1980. Geological summary of the North Philippine Sea based on Deep Sea Drilling Project Leg 58 Results. In Klein, G. deV., and Kobayashi, K., et al., *Init. Repts. DSDP*, Washington (U.S. Govt. Printing Office), 58, 951-961.
- Kevenvolden, K.A., and Barnard, L.A. 1983. Gsa hydrates of the Blake Outer Ridge, site 533, Deep Sea Drilling Project Leg 76. In Sheridan, R.E., Gradstein, F.M., *Init. Repts. DSDP*, Washington (U.S. Govt. Printing Office), 76, 353-365.
- Langseth, M.G., and Moore, J.C. 1990. Introduction to special section on the role of fluids in sediment accretion, deformation, diagenesis, and metamorphism in subduction zones. *J. geophys. Res.* 95, 8737-8742.
- Langseth, M.G., Westbrook, G.K. and Hobart, M. 1990. Contrasting geothermal regimes of the Barbados ridge accretionary complex. *J. geophys. Res.* 95, 8829-8844.
- Leggett, J. K., Aoki, Y. and Toba, T. 1985. Transition from frontal accretion to underplating in a part of the Nankai Trough accretionary complex off Shikoku (SW Japan) and extensional features on the lower trench slope. *Mari. Petrol. Geol.* 2, 131-141.

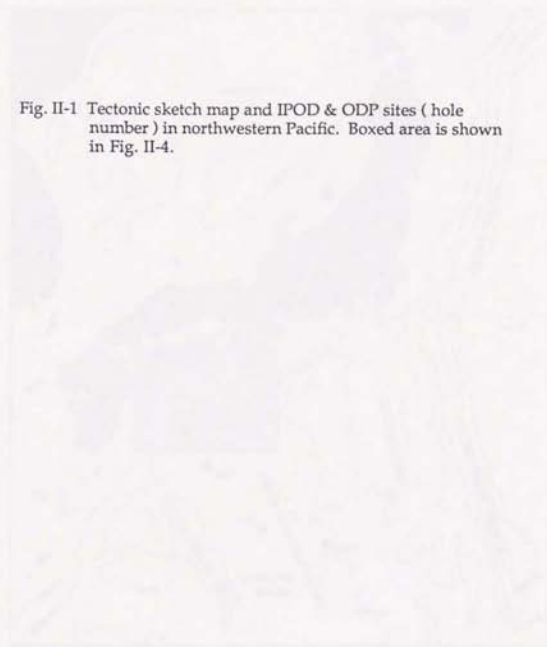
- Le Pichon, X., Iiyama, T., Chamley, H., Charvet, J., Faure, M., Fujimoto, H., Furuta, T., Ida, Y., Kagami, H., Lallemand, S., Leggett, J., Murata, A., Okada, H., Rangin, C., Renard, V., Taira, A. and Tokuyama, H. 1987. Nankai Trough and the fossil Shikoku Ridge, results of Box 6 Kaiko survey. *Earth Planet Sci. Lett.* 83, 186-198.
- Le Pichon, X., Foucher, J., Boulegue, J., Henry, P., Lallemand, S., Benedetti, M., Avedik, F., and Marippt, A. 1990. Mud volcano field seaward of the Barbados accretionary complex: A submersible survey. *J. Geophys. Res.* 95, 8931-8944.
- Minshull, T., and White, R. 1989. Sediment compaction and fluid migration in Makran Accretionary Prism. *J. Geophys. Res.* 94, 7387-7402.
- Moore, G.F., Shipley, T.H., Stoffa, P.L., Karig, D.E., Taira, A., Kuramoto, S., Tokuyama, H., and Suyehiro, K. 1990. Structural of the Nankai Trough accretionary zone from multichannel seismic reflection data. *J. Geophys. Res.* 95, 8753-8765.
- Moore, J. C. 1989. Tectonics and hydrogeology of accretionary prisms: role of the decollement zone. *Jour. Structural Geol.* 11, 95-106.
- Moore, J.C., Orange, D., and Kulm, L.D. 1990. Interrelationship of fluid venting and structural evolution: Alvin observations from the frontal accretionary prism, Oregon. *J. Geophys. Res.* 95, 8795-8808.
- Nagihara, S., Kinoshita, H., and Yamano, M. 1989. On the high heat flow in the Nankai Trough area - a simulation study on a heat rebound process. *Tectonophysics*, 161, 33-41.
- Nasu, N., Tomoda, Y., et al. 1982. Multichannel seismic reflection data across Nankai Trough, *Ocean Research Institute, University of Tokyo, IPOD-Japan Basic Ser.* 4.
- Ranken, B., Cardwell, R.K. and Karig, D. E. 1984. Kinematics of the Philippine sea plate. *Tectonics*, 3, 555-575.
- Seno, T. 1977. The instantaneous rotation vector of the Philippine Sea plate relative to the Eurasian plate. *Tectonophysics*, 42, 209-226.

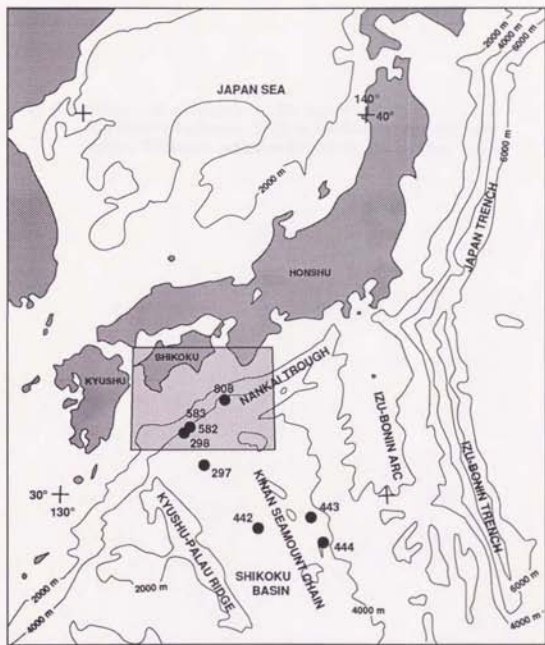
- Shih, T.C. 1980. Magnetic lineations in the Shikoku Basin. In Klein, G. deV., Kobayashi, K., et al., *Init. Repts. DSDP*, Washington (U.S. Govt. Printing Office), 58, 783-788.
- Shibley, T.H., Houston, M.H., Buffler, R.T., Shaub, F.J., McMillen, K.J., Ladd, J.W., and Worzel. 1979. Seismic evidence for widespread possible gas hydrate horizons on continental slopes and rises. *Am. Ass. Petro. Geol. Bull.* 63, 2204-2213.
- Stoll, R.D., Ewing, J., and Bryan, G.M. 1971. Anomalous wave velocities in sediments containing gas hydrate. *J. Geophys. Res.* 76, 2090-2095.
- Taira, A., Nishiyama, E., Tokuyama, H., Kinoshita, M., Soh, W., and Ashi, J. 1988. Hydrogeologic framework of the Nankai Trough accretionary prism. *Preliminary Report of the Hakuho Maru cruise KH86-5: ODP Site Survey*. Ocean Research Institute, University of Tokyo, 207-221.
- Taira, A., Hill, I., Firth, J. et al. in press. *Proc. ODP, Init. Rept., 131: Collage Station, TX* (Ocean Drilling Program).
- Tucholke, B.E., Bryan, G.M., and Ewing, J.I. 1977. Gas-hydrate horizons detected in seismic-profiler data from the western North Atlantic. *Am. Ass. Petro. Geol. Bull.* 61, 698-707.
- Uyeda, S. 1972. Heat flow. In Miyamura, S., and Uyeda, S. (Eds.), *The Crust and Upper Mantle of the Japanese Area* (Part 1, Geophysics): Tokyo (Earthquake Research Institute, University of Tokyo), pp. 97-105.
- Watanabe, T., Langseth, M., and Anderson, R.N. 1977. Heat flow in back-arc basins of the western Pacific. In Talwani, M., and Pitman, W.C., III (Eds.), *Island Arcs, Deep Sea Trenches, and Backarc Basins: Washington* (Am. Geophys. Union), Maurice Ewing Series, 1, 137-167.
- Westbrook, G. K., and Smith, M. J. 1983. Long decollements and mud volcanoes: Evidence from the Barbados Ridge Complex for the role of high pore-fluid pressure in the development of an accretionary complex. *Geology*, 11, 279-283.
- Yamano, M., Uyeda, S., Aoki, Y., and Shibley, T.H. 1982. Estimates of heat flow derived from gas hydrates. *Geology*, 10, 339-343.

- Yamano, M., Honda, S., and Uyeda, S. 1984. Nankai Trough: A hot trench ?. *Marine Geophysical Researches*, 6, 187-203.
- Yamano, M., Ku, K., Uyeda, S., Kinoshita, M. and Taira, A. 1986. Heat flow distribution in the Nankai Trough Area estimated from BSRs due to gas hydrate. *Abstracts of international Kaikio conference on subduction zones*, 33.
- Yoshii, T. 1979. Compilation of geophysical data around the Japanese Islands (1). *Bull. Earthquake Res. Inst. Univ. Tokyo*, 54, 75-117.
- Yoshii, T. and Kobayashi, K. 1981. Geophysics of Subduction Zones, *Kagaku* 51, 472-478 (in Japanese).

FIGURES

Fig. II-1 Tectonic sketch map and IPOD & ODP sites (hole number) in northwestern Pacific. Boxed area is shown in Fig. II-4.





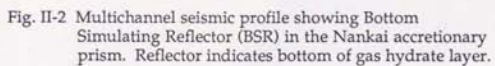


Fig. II-2 Multichannel seismic profile showing Bottom Simulating Reflector (BSR) in the Nankai accretionary prism. Reflector indicates bottom of gas hydrate layer.

TWT (s)

2.0

5 km

4.0

6.0

8.0

SLOPE BASIN

BSR

THRUST

NW

SE

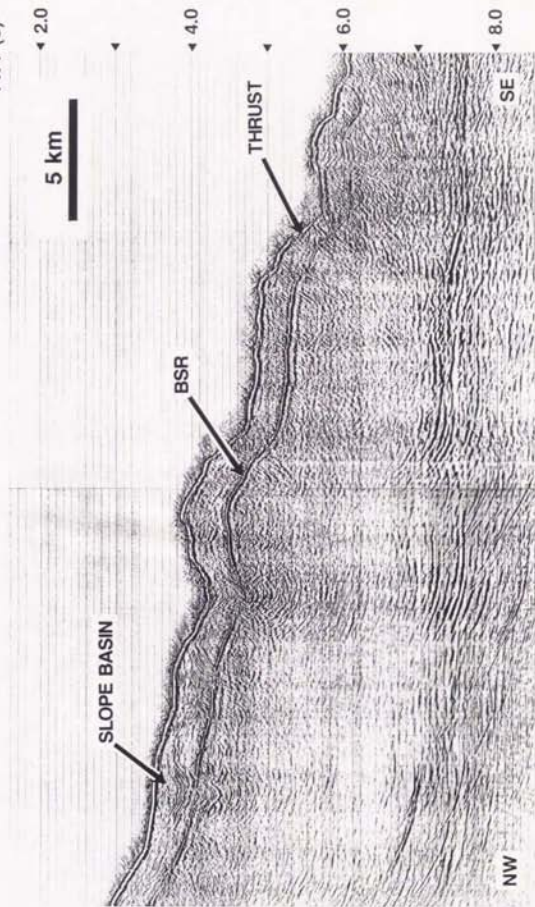


Fig. II-3 Flow chart of heat flow estimation from seismic reflection profile.



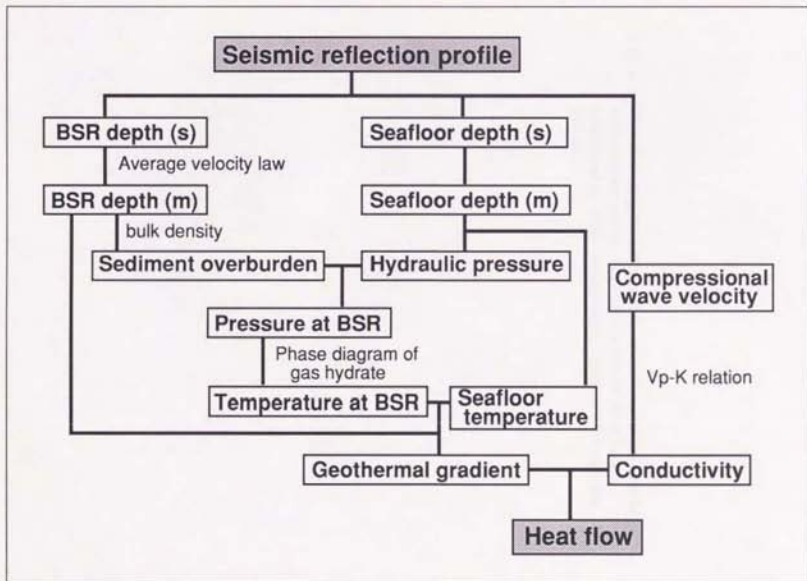
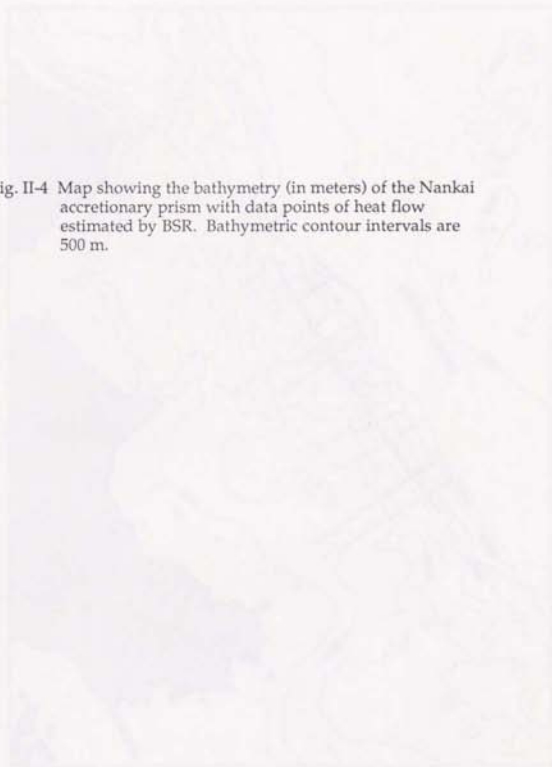


Fig. II-4 Map showing the bathymetry (in meters) of the Nankai accretionary prism with data points of heat flow estimated by BSR. Bathymetric contour intervals are 500 m.



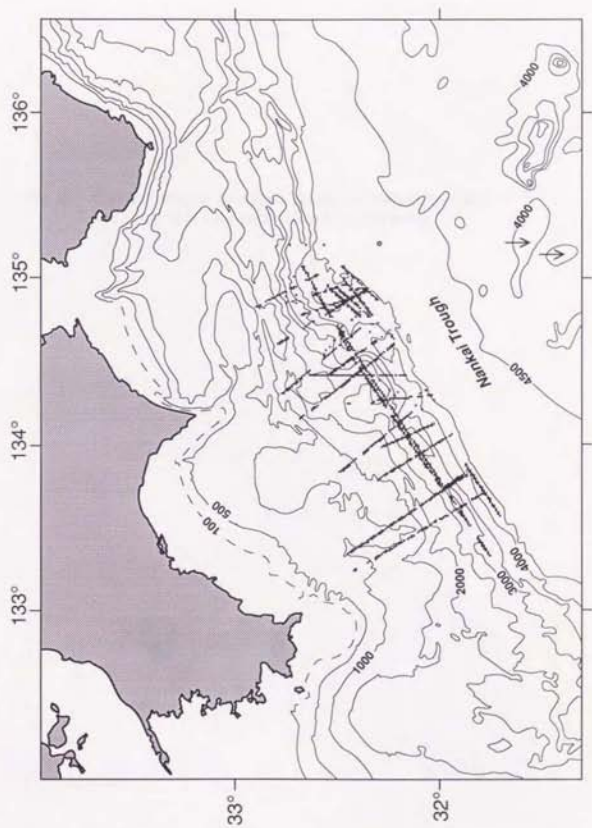
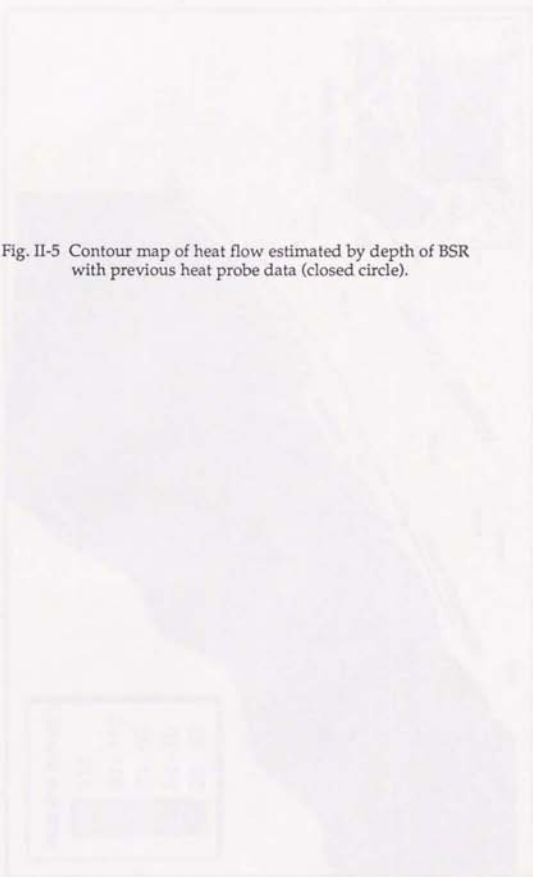


Fig. II-5 Contour map of heat flow estimated by depth of BSR with previous heat probe data (closed circle).



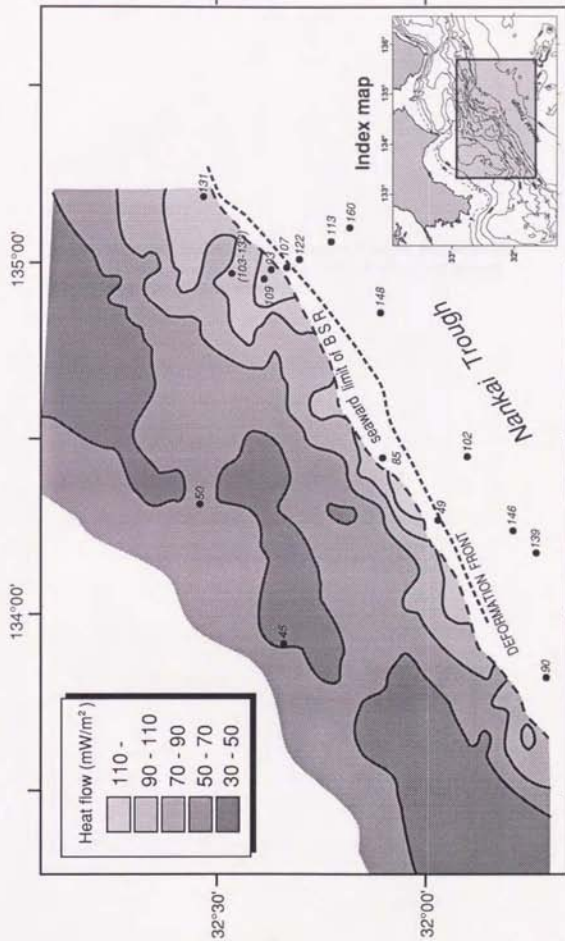


Fig. II-6 Migrated multichannel seismic reflection profile of line NT62-8, located on Fig. A3. No observations of BSR near the deformation front.

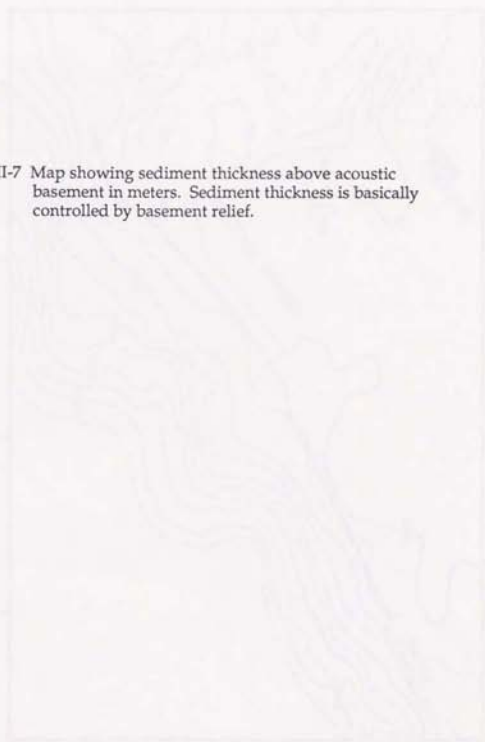
TWT(s)

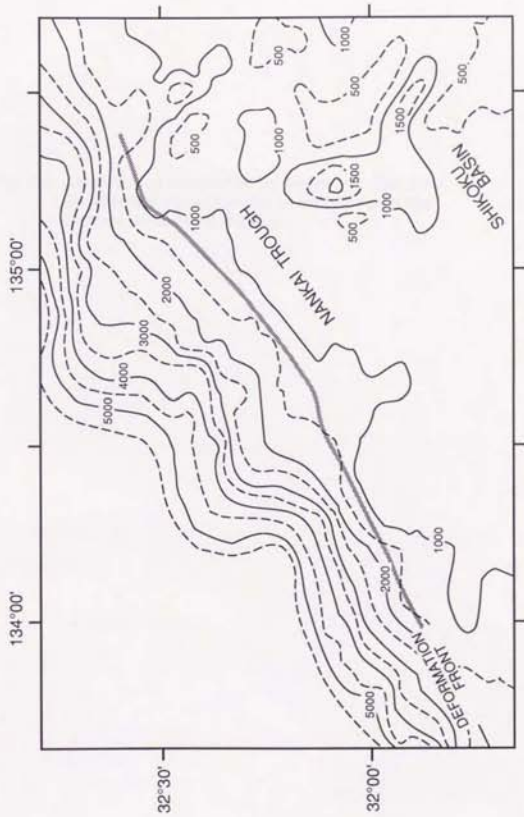
◀5.0

2 km



Fig. II-7 Map showing sediment thickness above acoustic basement in meters. Sediment thickness is basically controlled by basement relief.





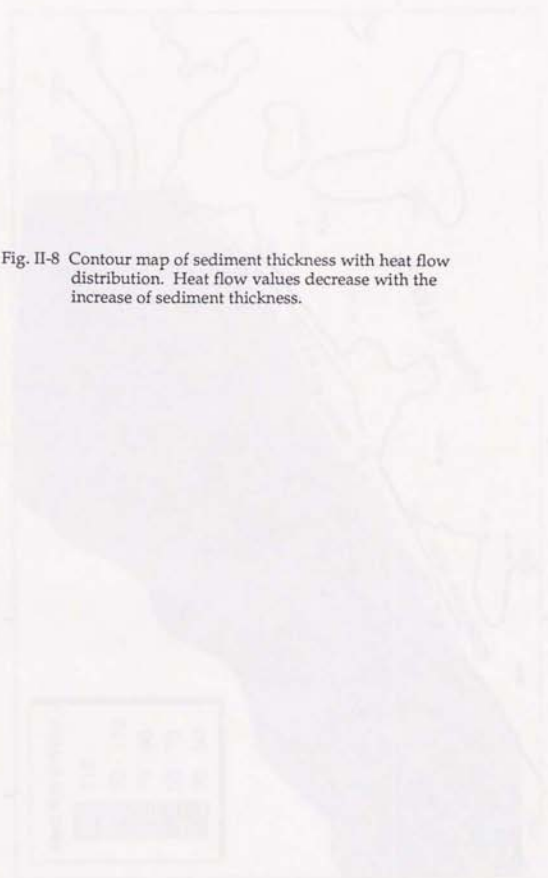
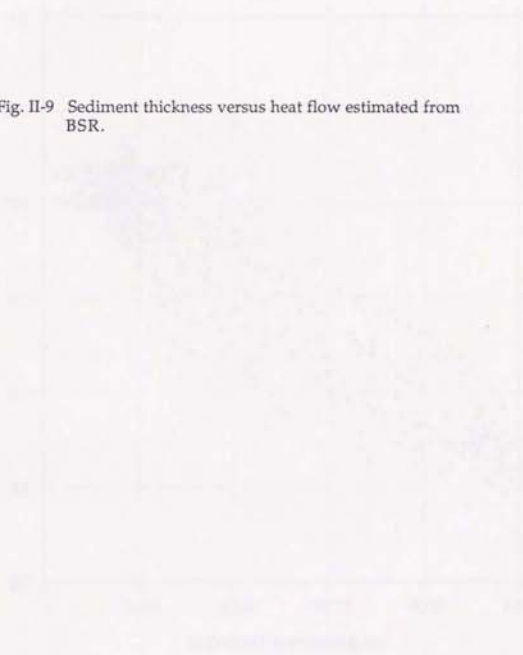


Fig. II-8 Contour map of sediment thickness with heat flow distribution. Heat flow values decrease with the increase of sediment thickness.

Fig. II-9 Sediment thickness versus heat flow estimated from BSR.



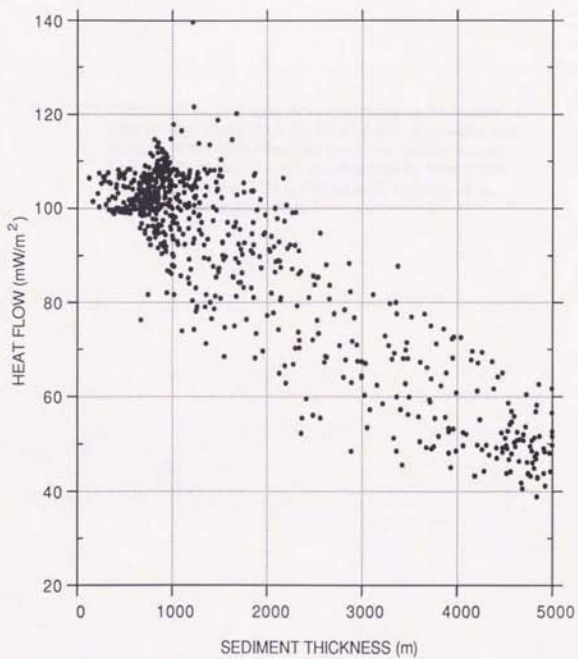
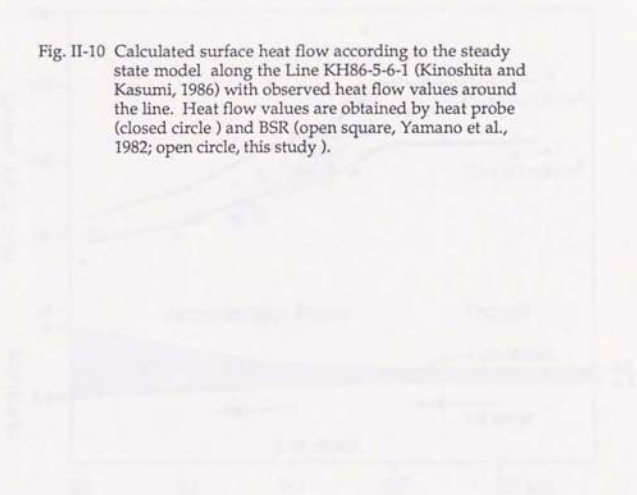


Fig. II-10 Calculated surface heat flow according to the steady state model along the Line KH86-5-6-1 (Kinoshita and Kasumi, 1986) with observed heat flow values around the line. Heat flow values are obtained by heat probe (closed circle) and BSR (open square, Yamano et al., 1982; open circle, this study).



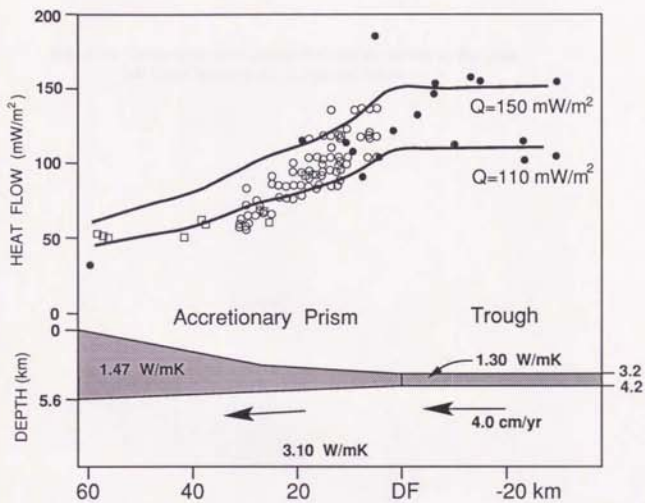
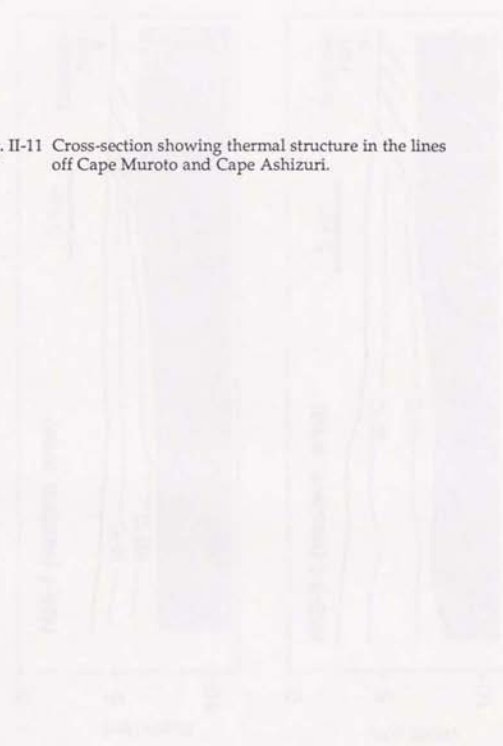


Fig. II-11 Cross-section showing thermal structure in the lines off Cape Muroto and Cape Ashizuri.



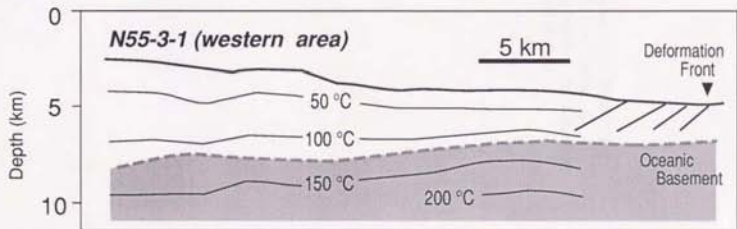
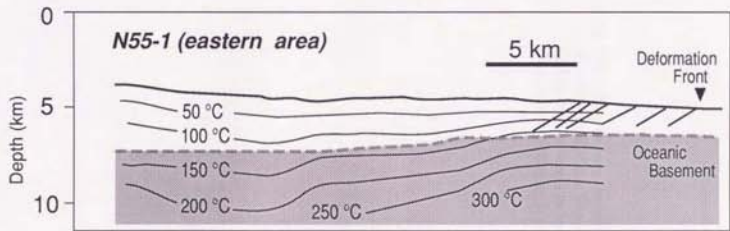
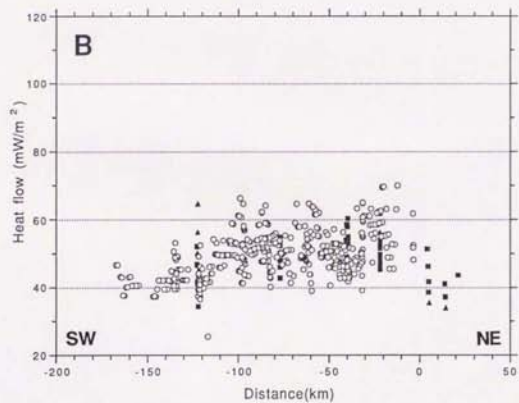
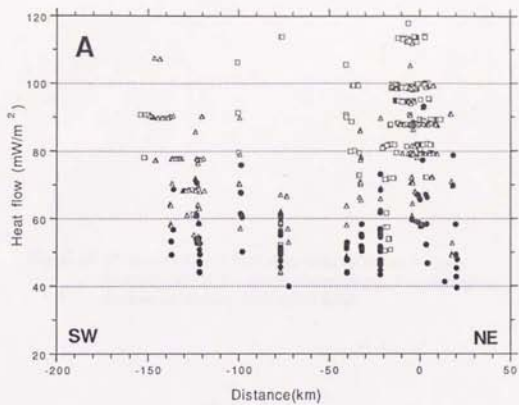


Fig. II-12 Heat flow values versus distance from the NW-SE trending line of the Kinan Seamount chain. A: Sediment thickness is less than 3000 m. B: Sediment thickness is between 3000 m and 6000 m.



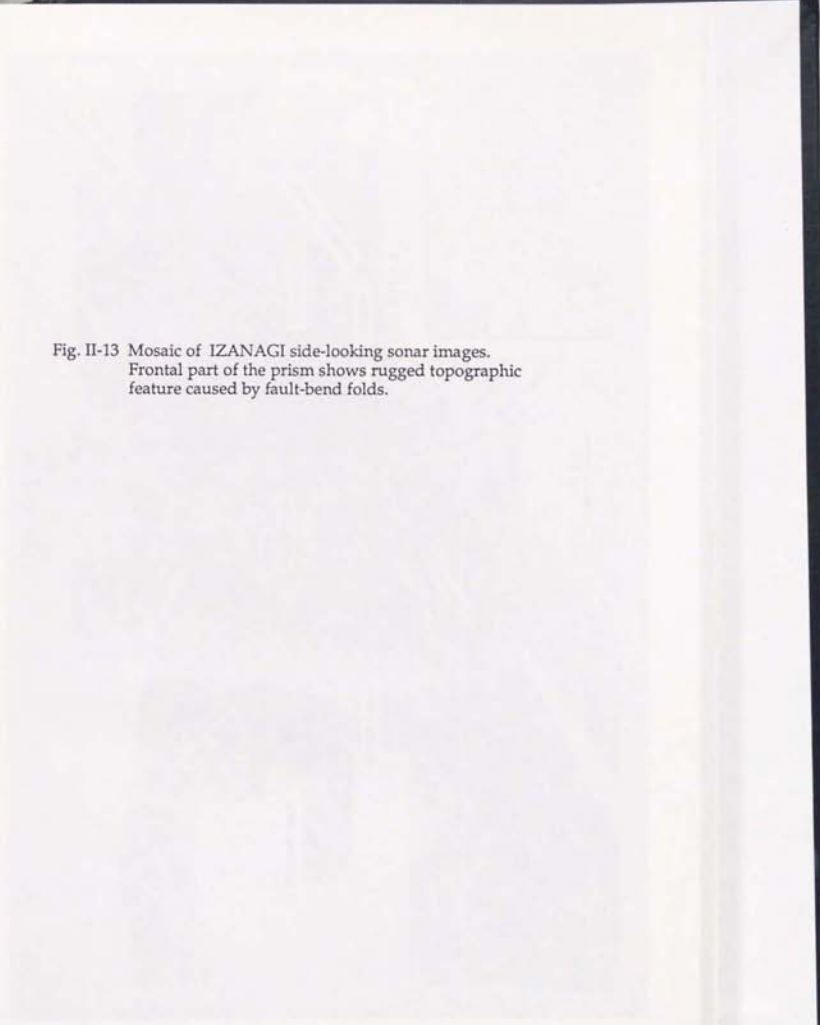


Fig. II-13 Mosaic of IZANAGI side-looking sonar images.
Frontal part of the prism shows rugged topographic
feature caused by fault-bend folds.

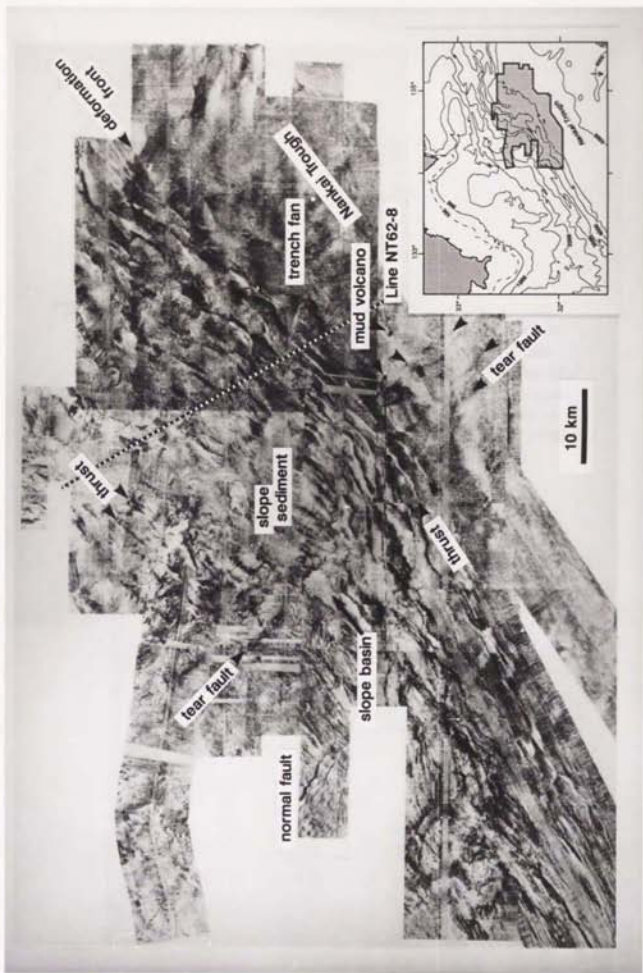
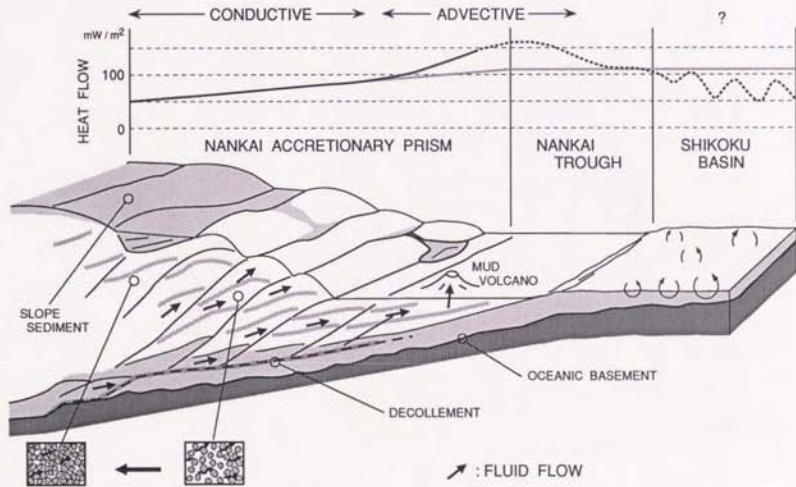


Fig. II-14 Schematic diagram showing fluid expulsion (below) and heat flow variation (above) from the Shikoku Basin to the Nankai accretionary prism. Solid line is heat flow value estimated by BSR in this study and dotted line indicates heat flow pattern from previous heat flow data (e.g. Yamano et al., 1984). Gray line is predicted heat flow value based on the age of the Shikoku Basin (Kinoshita and Kasumi, 1988). Discrepancy between solid (dotted) line and gray line indicates advective fluid flow.



APPENDIX

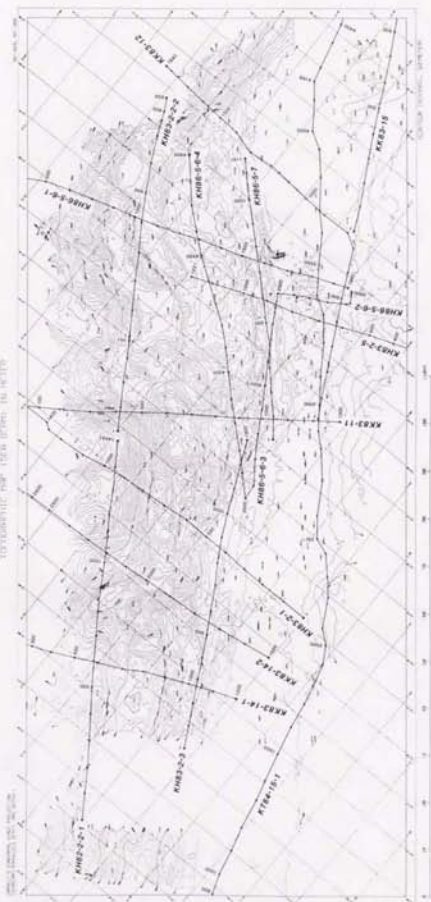
APPENDIX

Fig. A1 Track chart of JAPEX lines.

APPENDIX

Fig. A2 Track chart of ORI lines.

ISOTHERMIC MAP FOR DESIGN IN WATER



APPENDIX

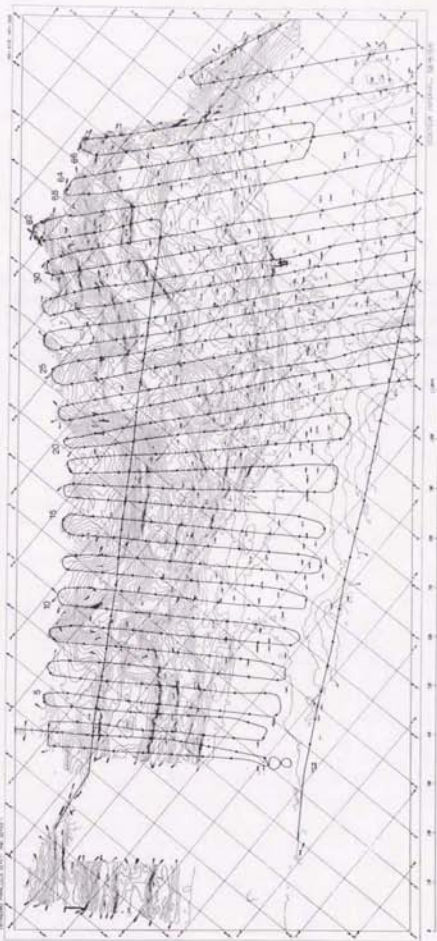
Fig. A3. Track chart of Fred-Moore lines.

APPENDIX

Fig. A4. Track chart of KAIKO Project single channel lines.

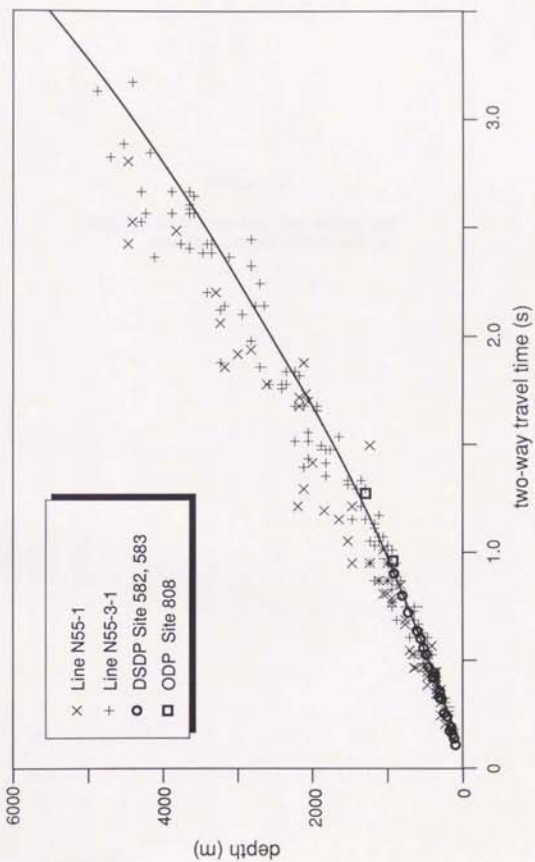
МЕДИУМНО-ТОПОГРАФИЧЕСКАЯ КАРТА ВЕТЕРИНАРНОГО ЗАВОДА

МАСШТАБ 1:5000



APPENDIX

Fig. A5 Average velocity law used in the estimation of the sediment thickness. The data of relation between depth and two-way travel time are interval velocities estimated by Nasu et al.(1982) and drilling results compared with seismic reflection lines (Kagami, Karig, et al., 1986; Taira, Hill, Firth, et al., in press).



APPENDIX

Fig. A6 Calculated heat flow values and seabottom depth with locations.

134.83 30.87 3880.00 89.00
134.82 30.86 3879.00 89.00
134.79 30.85 3878.00 89.00
134.81 30.84 3877.00 89.00
134.78 30.83 3876.00 89.00
134.80 30.82 3875.00 89.00
134.77 30.81 3874.00 89.00
134.79 30.80 3873.00 89.00
134.76 30.79 3872.00 89.00
134.78 30.78 3871.00 89.00
134.75 30.77 3870.00 89.00
134.77 30.76 3869.00 89.00
134.74 30.75 3868.00 89.00
134.76 30.74 3867.00 89.00
134.73 30.73 3866.00 89.00
134.75 30.72 3865.00 89.00
134.72 30.71 3864.00 89.00
134.74 30.70 3863.00 89.00
134.71 30.69 3862.00 89.00
134.73 30.68 3861.00 89.00
134.70 30.67 3860.00 89.00
134.72 30.66 3859.00 89.00
134.69 30.65 3858.00 89.00
134.71 30.64 3857.00 89.00
134.68 30.63 3856.00 89.00
134.70 30.62 3855.00 89.00
134.67 30.61 3854.00 89.00
134.69 30.60 3853.00 89.00
134.66 30.59 3852.00 89.00
134.68 30.58 3851.00 89.00
134.65 30.57 3850.00 89.00
134.67 30.56 3849.00 89.00
134.64 30.55 3848.00 89.00
134.66 30.54 3847.00 89.00
134.63 30.53 3846.00 89.00
134.65 30.52 3845.00 89.00
134.62 30.51 3844.00 89.00
134.64 30.50 3843.00 89.00
134.61 30.49 3842.00 89.00
134.63 30.48 3841.00 89.00
134.60 30.47 3840.00 89.00
134.62 30.46 3839.00 89.00
134.59 30.45 3838.00 89.00
134.61 30.44 3837.00 89.00
134.58 30.43 3836.00 89.00
134.60 30.42 3835.00 89.00
134.57 30.41 3834.00 89.00
134.59 30.40 3833.00 89.00
134.56 30.39 3832.00 89.00
134.58 30.38 3831.00 89.00
134.55 30.37 3830.00 89.00
134.57 30.36 3829.00 89.00
134.54 30.35 3828.00 89.00
134.56 30.34 3827.00 89.00
134.53 30.33 3826.00 89.00
134.55 30.32 3825.00 89.00
134.52 30.31 3824.00 89.00
134.54 30.30 3823.00 89.00
134.51 30.29 3822.00 89.00
134.53 30.28 3821.00 89.00
134.50 30.27 3820.00 89.00
134.52 30.26 3819.00 89.00
134.49 30.25 3818.00 89.00
134.51 30.24 3817.00 89.00
134.48 30.23 3816.00 89.00
134.50 30.22 3815.00 89.00
134.47 30.21 3814.00 89.00
134.49 30.20 3813.00 89.00
134.46 30.19 3812.00 89.00
134.48 30.18 3811.00 89.00
134.45 30.17 3810.00 89.00
134.47 30.16 3809.00 89.00
134.44 30.15 3808.00 89.00
134.46 30.14 3807.00 89.00
134.43 30.13 3806.00 89.00
134.45 30.12 3805.00 89.00
134.42 30.11 3804.00 89.00
134.44 30.10 3803.00 89.00
134.41 30.09 3802.00 89.00
134.43 30.08 3801.00 89.00
134.40 30.07 3800.00 89.00
134.42 30.06 3799.00 89.00
134.39 30.05 3798.00 89.00
134.41 30.04 3797.00 89.00
134.38 30.03 3796.00 89.00
134.40 30.02 3795.00 89.00
134.37 30.01 3794.00 89.00
134.39 30.00 3793.00 89.00
134.36 29.99 3792.00 89.00
134.38 29.98 3791.00 89.00
134.35 29.97 3790.00 89.00
134.37 29.96 3789.00 89.00
134.34 29.95 3788.00 89.00
134.36 29.94 3787.00 89.00
134.33 29.93 3786.00 89.00
134.35 29.92 3785.00 89.00
134.32 29.91 3784.00 89.00
134.34 29.90 3783.00 89.00
134.31 29.89 3782.00 89.00
134.33 29.88 3781.00 89.00
134.30 29.87 3780.00 89.00
134.32 29.86 3779.00 89.00
134.29 29.85 3778.00 89.00
134.31 29.84 3777.00 89.00
134.28 29.83 3776.00 89.00
134.30 29.82 3775.00 89.00
134.27 29.81 3774.00 89.00
134.29 29.80 3773.00 89.00
134.26 29.79 3772.00 89.00
134.28 29.78 3771.00 89.00
134.25 29.77 3770.00 89.00
134.27 29.76 3769.00 89.00
134.24 29.75 3768.00 89.00
134.26 29.74 3767.00 89.00
134.23 29.73 3766.00 89.00
134.25 29.72 3765.00 89.00
134.22 29.71 3764.00 89.00
134.24 29.70 3763.00 89.00
134.21 29.69 3762.00 89.00
134.23 29.68 3761.00 89.00
134.20 29.67 3760.00 89.00
134.22 29.66 3759.00 89.00
134.19 29.65 3758.00 89.00
134.21 29.64 3757.00 89.00
134.18 29.63 3756.00 89.00
134.20 29.62 3755.00 89.00
134.17 29.61 3754.00 89.00
134.19 29.60 3753.00 89.00
134.16 29.59 3752.00 89.00
134.18 29.58 3751.00 89.00
134.15 29.57 3750.00 89.00
134.17 29.56 3749.00 89.00
134.14 29.55 3748.00 89.00
134.16 29.54 3747.00 89.00
134.13 29.53 3746.00 89.00
134.15 29.52 3745.00 89.00
134.12 29.51 3744.00 89.00
134.14 29.50 3743.00 89.00
134.11 29.49 3742.00 89.00
134.13 29.48 3741.00 89.00
134.10 29.47 3740.00 89.00
134.12 29.46 3739.00 89.00
134.09 29.45 3738.00 89.00
134.11 29.44 3737.00 89.00
134.08 29.43 3736.00 89.00
134.10 29.42 3735.00 89.00
134.07 29.41 3734.00 89.00
134.09 29.40 3733.00 89.00
134.06 29.39 3732.00 89.00
134.08 29.38 3731.00 89.00
134.05 29.37 3730.00 89.00
134.07 29.36 3729.00 89.00
134.04 29.35 3728.00 89.00
134.06 29.34 3727.00 89.00
134.03 29.33 3726.00 89.00
134.05 29.32 3725.00 89.00
134.02 29.31 3724.00 89.00
134.04 29.30 3723.00 89.00
134.01 29.29 3722.00 89.00
134.03 29.28 3721.00 89.00
134.00 29.27 3720.00 89.00
134.02 29.26 3719.00 89.00
133.99 29.25 3718.00 89.00
134.01 29.24 3717.00 89.00
133.98 29.23 3716.00 89.00
134.00 29.22 3715.00 89.00
133.97 29.21 3714.00 89.00
134.00 29.20 3713.00 89.00
133.95 29.19 3712.00 89.00
133.97 29.18 3711.00 89.00
133.94 29.17 3710.00 89.00
133.96 29.16 3709.00 89.00
133.93 29.15 3708.00 89.00
133.95 29.14 3707.00 89.00
133.92 29.13 3706.00 89.00
133.94 29.12 3705.00 89.00
133.91 29.11 3704.00 89.00
133.93 29.10 3703.00 89.00
133.90 29.09 3702.00 89.00
133.92 29.08 3701.00 89.00
133.89 29.07 3700.00 89.00
133.91 29.06 3699.00 89.00
133.88 29.05 3698.00 89.00
133.90 29.04 3697.00 89.00
133.87 29.03 3696.00 89.00
133.89 29.02 3695.00 89.00
133.86 29.01 3694.00 89.00
133.88 29.00 3693.00 89.00
133.85 28.99 3692.00 89.00
133.87 28.98 3691.00 89.00
133.84 28.97 3690.00 89.00
133.86 28.96 3689.00 89.00
133.83 28.95 3688.00 89.00
133.85 28.94 3687.00 89.00
133.82 28.93 3686.00 89.00
133.84 28.92 3685.00 89.00
133.81 28.91 3684.00 89.00
133.83 28.90 3683.00 89.00
133.80 28.89 3682.00 89.00
133.82 28.88 3681.00 89.00
133.79 28.87 3680.00 89.00
133.81 28.86 3679.00 89.00
133.78 28.85 3678.00 89.00
133.80 28.84 3677.00 89.00
133.77 28.83 3676.00 89.00
133.79 28.82 3675.00 89.00
133.76 28.81 3674.00 89.00
133.78 28.80 3673.00 89.00
133.75 28.79 3672.00 89.00
133.77 28.78 3671.00 89.00
133.74 28.77 3670.00 89.00
133.76 28.76 3669.00 89.00
133.73 28.75 3668.00 89.00
133.75 28.74 3667.00 89.00
133.72 28.73 3666.00 89.00
133.74 28.72 3665.00 89.00
133.71 28.71 3664.00 89.00
133.73 28.70 3663.00 89.00
133.70 28.69 3662.00 89.00
133.72 28.68 3661.00 89.00
133.69 28.67 3660.00 89.00
133.71 28.66 3659.00 89.00
133.68 28.65 3658.00 89.00
133.70 28.64 3657.00 89.00
133.67 28.63 3656.00 89.00
133.69 28.62 3655.00 89.00
133.66 28.61 3654.00 89.00
133.68 28.60 3653.00 89.00
133.65 28.59 3652.00 89.00
133.67 28.58 3651.00 89.00
133.64 28.57 3650.00 89.00
133.66 28.56 3649.00 89.00
133.63 28.55 3648.00 89.00
133.65 28.54 3647.00 89.00
133.62 28.53 3646.00 89.00
133.64 28.52 3645.00 89.00
133.61 28.51 3644.00 89.00
133.63 28.50 3643.00 89.00
133.60 28.49 3642.00 89.00
133.62 28.48 3641.00 89.00
133.59 28.47 3640.00 89.00
133.61 28.46 3639.00 89.00
133.58 28.45 3638.00 89.00
133.60 28.44 3637.00 89.00
133.57 28.43 3636.00 89.00
133.59 28.42 3635.00 89.00
133.56 28.41 3634.00 89.00
133.58 28.40 3633.00 89.00
133.55 28.39 3632.00 89.00
133.57 28.38 3631.00 89.00
133.54 28.37 3630.00 89.00
133.56 28.36 3629.00 89.00
133.53 28.35 3628.00 89.00
133.55 28.34 3627.00 89.00
133.52 28.33 3626.00 89.00
133.54 28.32 3625.00 89.00
133.51 28.31 3624.00 89.00
133.53 28.30 3623.00 89.00
133.50 28.29 3622.00 89.00
133.52 28.28 3621.00 89.00
133.49 28.27 3620.00 89.00
133.51 28.26 3619.00 89.00
133.48 28.25 3618.00 89.00
133.50 28.24 3617.00 89.00
133.47 28.23 3616.00 89.00
133.49 28.22 3615.00 89.00
133.46 28.21 3614.00 89.00
133.48 28.20 3613.00 89.00
133.45 28.19 3612.00 89.00
133.47 28.18 3611.00 89.00
133.44 28.17 3610.00 89.00
133.46 28.16 3609.00 89.00
133.43 28.15 3608.00 89.00
133.45 28.14 3607.00 89.00
133.42 28.13 3606.00 89.00
133.44 28.12 3605.00 89.00
133.41 28.11 3604.00 89.00
133.43 28.10 3603.00 89.00
133.40 28.09 3602.00 89.00
133.42 28.08 3601.00 89.00
133.39 28.07 3600.00 89.00
133.41 28.06 3599.00 89.00
133.38 28.05 3598.00 89.00
133.40 28.04 3597.00 89.00
133.37 28.03 3596.00 89.00
133.39 28.02 3595.00 89.00
133.36 28.01 3594.00 89.00
133.38 28.00 3593.00 89.00
133.35 27.99 3592.00 89.00
133.37 27.98 3591.00 89.00
133.34 27.97 3590.00 89.00
133.36 27.96 3589.00 89.00
133.33 27.95 3588.00 89.00
133.35 27.94 3587.00 89.00
133.32 27.93 3586.00 89.00
133.34 27.92 3585.00 89.00
133.31 27.91 3584.00 89.00
133.33 27.90 3583.00 89.00
133.30 27.89 3582.00 89.00
133.32 27.88 3581.00 89.00
133.29 27.87 3580.00 89.00
133.31 27.86 3579.00 89.00
133.28 27.85 3578.00 89.00
133.30 27.84 3577.00 89.00
133.27 27.83 3576.00 89.00
133.29 27.82 3575.00 89.00
133.26 27.81 3574.00 89.00
133.28 27.80 3573.00 89.00
133.25 27.79 3572.00 89.00
133.27 27.78 3571.00 89.00
133.24 27.77 3570.00 89.00
133.26 27.76 3569.00 89.00
133.23 27.75 3568.00 89.00
133.25 27.74 3567.00 89.00
133.22 27.73 3566.00 89.00
133.24 27.72 3565.00 89.00
133.21 27.71 3564.00 89.00
133.23 27.70 3563.00 89.00
133.20 27.69 3562.00 89.00
133.22 27.68 3561.00 89.00
133.19 27.67 3560.00 89.00
133.21 27.66 3559.00 89.00
133.18 27.65 3558.00 89.00
133.20 27.64 3557.00 89.00
133.17 27.63 3556.00 89.00
133.19 27.62 3555.00 89.00
133.16 27.61 3554.00 89.00
133.18 27.60 3553.00 89.00
133.15 27.59 3552.00 89.00
133.17 27.58 3551.00 89.00
133.14 27.57 3550.00 89.00
133.16 27.56 3549.00 89.00
133.13 27.55 3548.00 89.00
133.15 27.54 3547.00 89.00
133.12 27.53 3546.00 89.00
133.14 27.52 3545.00 89.00
133.11 27.51 3544.00 89.00
133.13 27.50 3543.00 89.00
133.10 27.49 3542.00 89.00
133.12 27.48 3541.00 89.00
133.09 27.47 3540.00 89.00
133.11 27.46 3539.00 89.00
133.08 27.45 3538.00 89.00
133.10 27.44 3537.00 89.00
133.07 27.43 3536.00 89.00
133.09 27.42 3535.00 89.00
133.06 27.41 3534.00 89.00
133.08 27.40 3533.00 89.00
133.05 27.39 3532.00 89.00
133.07 27.38 3531.00 89.00
133.04 27.37 3530.00 89.00
133.06 27.36 3529.00 89.00
133.03 27.35 3528.00 89.00
133.05 27.34 3527.00 89.00
133.02 27.33 3526.00 89.00
133.04 27.32 3525.00 89.00
133.01 27.31 3524.00 89.00
133.03 27.30 3523.00 89.00
133.00 27.29 3522.00 89.00
133.02 27.28 3521.00 89.00
132.99 27.27 3520.00 89.00
133.01 27.26 3519.00 89.00
132.98 27.25 3518.00 89.00
133.00 27.24 3517.00 89.00
132.97 27.23 3516.00 89.00
132.99 27.22 3515.00 89.00
132.96 27.21 3514.00 89.00
132.98 27.20 3513.00 89.00
132.95 27.19 3512.00 89.00
132.97 27.18 3511.00 89.00
132.94 27.17 3510.00 89.00
132.96 27.16 3509.00 89.00
132.93 27.15 3508.00 89.00
132.95 27.14 3507.00 89.00
132.92 27.13 3506.00 89.00
132.94 27.12 3505.00 89.00
132.91 27.11 3504.00 89.00
132.93 27.10 3503.00 89.00
132.90 27.09 3502.00 89.00
132.92 27.08 3501.00 89.00
132.89 27.07 3500.00 89.00
132.91 27.06 3499.00 89.00
132.88 27.05 3498.00 89.00
132.90 27.04 3497.00 89.00
132.87 27.03 3496.00 89.00
132.89 27.02 3495.00 89.00
132.86 27.01 3494.00 89.00
132.88 27.00 3493.00 89.00
132.85 26.99 3492.00 89.00
132.87 26.98 3491.00 89.00
132.84 26.97 3490.00 89.00
132.86 26.96 3489.00 89.00
132.83 26.95 3488.00 89.00
132.85 26.94 3487.00 89.00
132.82 26.93 3486.00 89.00
132.84 26.92 3485.00 89.00
132.81 26.91 3484.00 89.00
132.83 26.90 3483.00 89.00
132.80 26.89 3482.00 89.00
132.82 26.88 3481.00 89.00
132.79 26.87 3480.00 89.00
132.81 26.86 3479.00 89.00
132.78 26.85 3478.00 89.00
132.80 26.84 3477.00 89.00
132.77 26.83 3476.00 89.00
132.79 26.82 3475.00 89.00
132.76 26.81 3474.00 89.00
132.78 26.80 3473.00 89.00
132.75 26.79 3472.00 89.00
132.77 26.78 3471.00 89.00
132.74 26.77 3470.00 89.00
132.76 26.76 3469.00 89.00
132.73 26.75 3468.00 89.00
132.75 26.74 3467.00 89.00
132.72 26.73 3466.00 89.00
132.74 26.72 3465.00 89.00
132.71 26.71 3464.00 89.00
132.73 26.70 3463.00 89.00
132.70 26.69 3462.00 89.00
132.72 26.68 3461.00 89.00
132.69 26.67 3460.00 89.00
132.71 26.66 3459.00 89.00
132.68 26.65 3458.00 89.00
132.70 26.64 3457.00 89.00
132.67 26.63 3456.00 89.00
132.69 26.62 3455.00 89.00
132.66 26.61 3454.00 89.00
132.68 26.60 3453.00 89.00
132.65 26.59 3452.00 89.00
132.67 26.58 3451.00 89.00
132.64 26.57 3450.00 89.00
132.66 26.56 3449.00 89.00
132.63 26.55 3448.00 89.00
132.65 26.54 3447.00 89.00
132.62 26.53 3446.00 89.00
132.64 26.52 3445.00 89.00
132.61 26.51 3444.00 89.00
132.63 26.50 3443.00 89.00
132.60 26.49 3442.00 89.00
132.62 26.48 3441.00 89.00
132.59 26.47 3440.00 89.00
132.6

